LBL-19021 c.2

Lawrence Berkeley Laboratory

UNIVERSITY OF CALIFORNIA

RECEIVED
LAWRENCE
BERKELEY LABORATORY

MAY 22 1985

LIBRARY AND
DOCUMENTS SECTION

Materials & Molecular Research Division

REARRANGEMENT DURING SINTERING OF TWO DIMENSIONAL ARRAYS OF SPHERES

M.W. Weiser
(M.S. Thesis)

April 1985

TWO-WEEK LOAN COPY

This is a Library Circulating Copy which may be borrowed for two weeks.

LBL-19021 c.2

Prepared for the U.S. Department of Energy under Contract DE-AC03-76SF00098

DISCLAIMER

This document was prepared as an account of work sponsored by the United States Government. While this document is believed to contain correct information, neither the United States Government nor any agency thereof, nor the Regents of the University of California, nor any of their employees, makes any warranty, express or implied, or assumes any legal responsibility for the accuracy, completeness, or usefulness of any information, apparatus, product, or process disclosed, or represents that its use would not infringe privately owned rights. Reference herein to any specific commercial product, process, or service by its trade name, trademark, manufacturer, or otherwise, does not necessarily constitute or imply its endorsement, recommendation, or favoring by the United States Government or any agency thereof, or the Regents of the University of California. The views and opinions of authors expressed herein do not necessarily state or reflect those of the United States Government or any agency thereof or the Regents of the University of California.

LBL-19021

Rearrangement During Sintering of Two Dimensional Arrays of Spheres

Martin William Weiser

Materials and Molecular Research Division
Materials Science and Mineral Engineering
Lawrence Berkeley Laboratory
University of California
Berkeley, California 94720

This work was supported by the Division of Materials Sciences, Office of Basic Sciences of the Department of Energy, under Contract No. DE-AC03-76SF00098.

Rearrangement During Sintering of Two Dimensional Arrays of Spheres

Martin William Weiser

Materials and Molecular Research Division
Materials Science and Mineral Engineering
Lawrence Berkeley Laboratory
University of California
Berkeley, California 94720

ABSTRACT

The rearrangement of large random arrays of spheres is studied in two dimensions using hot stage optical microscopy to enable all of the changes in the array to be observed from the very beginning of the sintering process. The local density at each sphere is defined using the Voronoi area and is used to describe the densification behavior of the arrays. Both the interparticle angles and distances are measured and used to describe the rearrangement of the spheres during sintering. The rearrangement behavior is found to involve long range interactions between many spheres. The extrapolation of the two-sphere model or the bending moment from asymmetric sintering necks in the three-sphere model gives a very poor description of the actual rearrangement as seen in this study. It is concluded that rearrangement is a long range, multiparticle process that arises out of local differential densification caused by the density fluctuations that are found in inhomogenously packed arrays.

Table of Contents

Acknowledgements iii

1 Introduction 1

2 Background 4

2.1 Two Particle Model 5

2.2 Three Particle Model 11

2.3 Multiparticle Arrays 16

2.4 Computer Simulations of Sintering 18

2.4.1 Sintering Maps 19

2.4.2 Discrete Particle Simulators 20

3 Experimental Procedure 25

3.1 Powder Preparation 25

3.2 Sample Preparation 27

3.3 Hot Stage Optical Microscopy 27

3.4 Image Analysis 28

3.4.1 Digitizing the Sphere Center Coordinates 28

3.4.2 Normalization of the Center Coordinates 30

3.5 Derived Quantities 31

4 Results 38

4.1 Overall Data 45

4.1.1 Density and Densification Rate 45

4.1.2 Average Sphere Coordination Number and Distribution 49

4.2 Local Density and Densification Rate 57

4.2.1 Local Densities 58

4.2.2 Local Densification Rate 74

4.3 Interparticle Distances 82

4.4 Interparticle Angles 87

4.4.1 Distribution of Interparticle Angles 90

4.4.2 Trends of Individual Angles 93

5 Color Mappings 104

5.1 Local Density 104

5.2 Local Shrinkage Rates 105

5.3 Maximum Angular Change 106

6 Conclusions 111

References 115

ACKNOWLEDGEMENTS

The author would like to thank the many people who assisted with this work and the completion of this thesis: my advisor, Lutgard C. De Jonghe who gave many helpful suggestions and encouragement; the staff of MMRD for their assistance in building the equipment to preform the experiments; the members of the LBL computer science division for assistance in creation of the software for the data analysis; the other graduate students for their assistance and encouragement; Patty Burt for much encouragement, particularly when the work was not going well.

This work was supported by the Division of Materials Sciences, Office of Basic Sciences of the U.S. Department of Energy, under contract No. DE-AC03-76SF00098.

1 Introduction

This study attempts to bridge the gap between one-dimensional sintering studies and the three-dimensional sintering that is actually preformed to produce products. Two-dimensional sintering experiments allow the observation of individual particles and sintering necks as in the one-dimensional case but these necks are subjected to the variety of forces and moments present in the three-dimensional case. This work is the most complete characterization of rearrangement during sintering in two dimensions to this time, and serves as the best description of the probable rearrangement processes in three dimensions.

One-dimensional sintering experiments, such as the two sphere model, yield a large amount of data about the mechanisms and rates of material transport during sintering. This type of experiment has improved our knowledge of sintering considerably but it is observed that when the data are extrapolated to three dimensions there is poor agreement with bulk sintering studies. A three-dimensional sintering study gives good, accurate data about the macroscopic densification which is of great use in producing a final product. Unfortunately, it is very difficult to determine what caused the formation of specific flaws in the sintered compact in this type of experiment. The two-dimensional sintering experiment allows the interactions of the individual particles to be studied but it involves the multiparticle influences found in the three-dimensional case.

A variety of two-dimensional experiments have been preformed, but they have either been only slightly more complex than the two sphere model or only minimal statistics have been taken about the array. In this study the relative motions of large arrays of spheres were studied as a function of sintering time. As seen in figure 1.1 these relative motions are observed to be rather complex

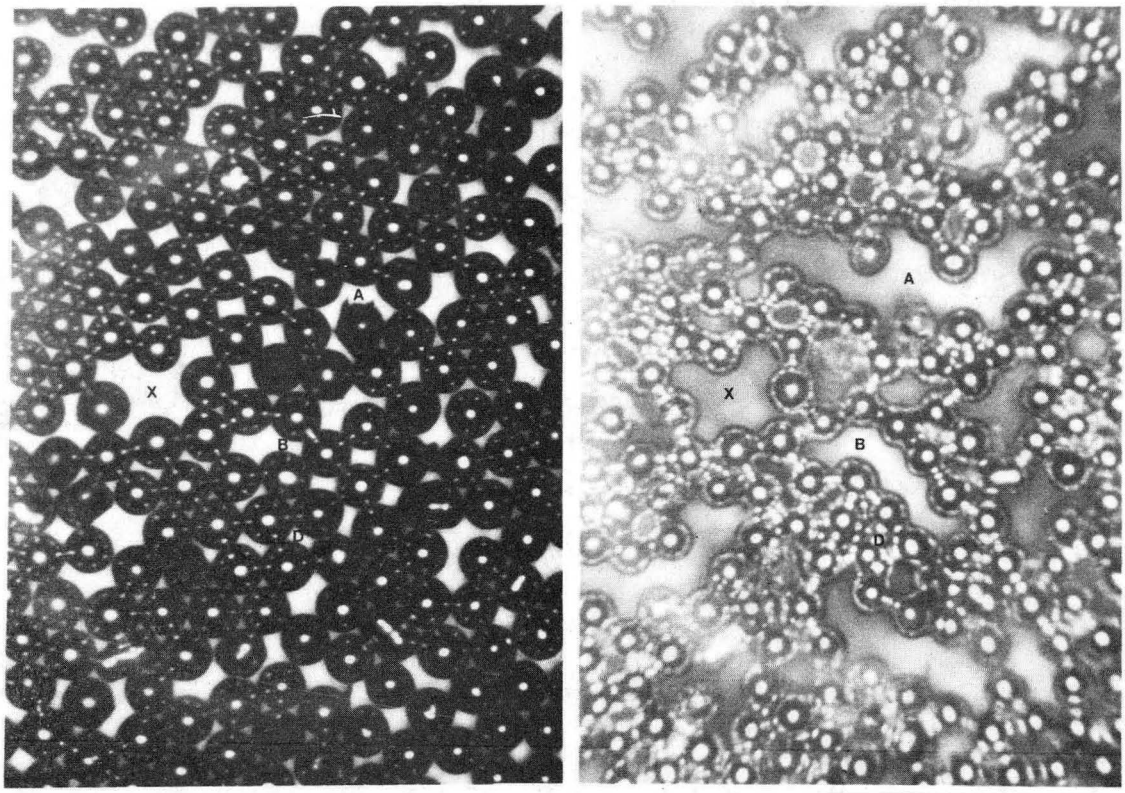

XBB 830-10602A

Figure 1.1 Micrograph of a representative two-dimensional sintering array showing the different types of behavior during sintering. The areas labeled A and B show the formation of enlongated pores. The pore labeled X exhibits rounding without growth. The area labeled D is a highly coordinated area that densifies homogeneously.

and can not be explained in the simple terms that had been previously proposed by other authors. From the location of the center of each of the spheres the local density, the interparticle angle, and the center to center distance were calculated. This large collection of data was then analyzed to determine the driving force of rearrangement during sintering and what effect this has upon the densification of a two-dimensional array of spheres.

2 Background

The earliest sintering experiments were concerned only with the production of a usable final product, and not with the details of how it was produced. As the desired quality of sintered products was increased it was necessary to study the details of the sintering process in order to determine where and how the improvements could be made. The earliest of this type of study involved the examination of either a fracture surface or a polished section after the powder sample had been sintered to determine what had happened during the heat treatment. The next stage of study was the simple model experiments involving a sphere and a plate, two spheres, or a series of cylinders. These experiments did a great deal to improve our understanding of the mechanisms of sintering, but were not directly applicable to real bulk sintering because of the many simplifications that had been made.

Next, many experiments were done that involved careful porosimetry, dilatometry, and serial sectioning techniques on three dimensional samples to determine the details of the sintering process. But unfortunately the complex geometry of these samples severely limits the amount of useful detailed information that can be obtained. A middle ground of geometric complexity was next reached in which multiparticle, two dimensional arrays of spheres were sintered to allow the examination of the particles during the sintering process. Yet another type of study involves the computer simulation of the sintering process. Computer simulation is a powerful tool that has not reached its potential because of the lack of detailed information on how the simple model experiments extrapolate to three dimensions. The next sections of this paper give some of the details of these studies in the order of their complexity and describe

how they they are related to the present work.

2.1 Two Particle Model

The two particle models include all of the geometrically simple systems such as the sphere and plate, the two sphere and the row of cylinders. All of these model experiments were designed to study the details of how the sintering neck forms and the degree of center to center approach of the particles. Most of these experiments dealt with determining what mechanism of material transport was causing the sintering.

The earliest work of this type was by Kuczynski [24] and employed the sphere and plate model. This was followed by Kingery and Berg [23], Wilson and Shewmon [32], Nichols [26], Johnson [21], Coble [6], and Wong and Pask [34]. All of these classic papers were primarily interested in the determination of the material transport mechanism. From the standpoint of the sintering of bulk powder compacts this work gave some good general guidelines on what heat treatment would give the desired results, but it was still necessary to run trial and error tests to determine the proper treatment for a particular powder and desired result.

The main problem with this type of study is that in order to get data about the neck growth and center approach it simplifies the overall system too far to give much detailed information about how a real compact might behave. For the complete prediction of the sintering behavior in three dimensions it is a very difficult if not impossible extrapolation from the one-dimensional situation of the two sphere model. This is a result of the of the many different external forces on the sintering neck that can arise in the three dimensional case that are

not present in the two sphere model. These stresses can be either tensile or compressive and can also include a torque on any axis relative to the sintering neck. The two sphere model, however, can be very useful in determining the effect of the various sintering mechanisms upon the neck growth and the center to center approach.

The above mentioned authors have preformed both experimental and theoretical work on the two sphere model of sintering. From analysis of the experimental work it is apparent that the grain boundary diffusion mechanism is of great importance in the sintering of copper in the range of 1200 to 1300 K. The material transport rate and shrinkage rate have been calculated on numerous occasions by these authors with a variety of results. These differences arise primarily because of the differences in the assumed boundary conditions and/or the approximations used. The present study will next draw upon the previous work, in particular that of Swinkles and Ashby [31], to derive the relationship between the sintering rate and the applied stress upon the neck.

Two different types of force can be applied to a sintering neck, an axial stress along the center to center line connecting the particles, and a bending moment at any angle about this axis as illustrated in figure 2.1. For the two sphere model considered here it is not currently possible to solve analytically for the effect of the bending moment. However, Hsueh and De Jonghe [19] have found an analytic solution for the closely related problem of two cylinders which finds that the effect of the moment and the axial force are independent. As such these two forces should be independent in the two sphere model. Therefore in this work the only the effect of an applied axial load will be derived.

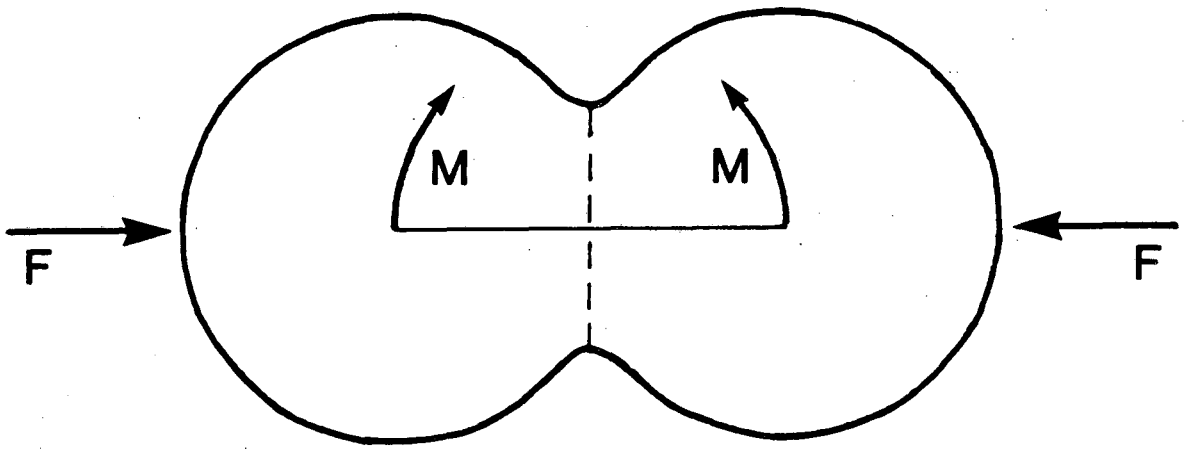

XBL 8412-5339

Figure 2.1 The two types of force that can be applied to a sintering neck shown here for the two-sphere model. F is an axial force and M is a bending moment about the axis connecting the sphere centers.

The two particle model used here is shown in cross section with the relevant geometric parameters in figure 2.2. For this geometry we can utilize the symmetry to write the stress normal to the grain boundary in the following form

$$\sigma(r) = C_1 r^2 + C_2 r + C_3 \tag{2.1}$$

where tension is assumed to be negative. The most useful and agreed upon set of boundary conditions are;

$$\sigma(x) = K \tag{2.2}$$

from continuality of the stress at the surface;

$$\frac{d\sigma}{dr}(0) = 0 \tag{2.3}$$

from the axial symmetry of the model;

$$\int_{r=0}^{r=x} 2\pi r\,\sigma(r)dr = -2\pi\gamma x + F \tag{2.4}$$

from the force balance normal to the grain boundary, with;

γ = surface tension

K = total surface curvature $= \frac{1}{x} - \frac{1}{\rho}$

F = applied force

Utilization of the second boundary condition simplifies the equation for the stress as a function of the radius to;

$$\sigma(r) = C_1 + C_3 \tag{2.5}$$

Using the stress of equation 2.5 in the both the first and third boundary conditions yields.

$$C_1 x^2 + C_3 = K\gamma \tag{2.6}$$

$$C_1 x^2 + 2C_3 = \frac{2F}{\pi x^2} - \frac{4\gamma}{x} \tag{2.7}$$

2 Sphere Model

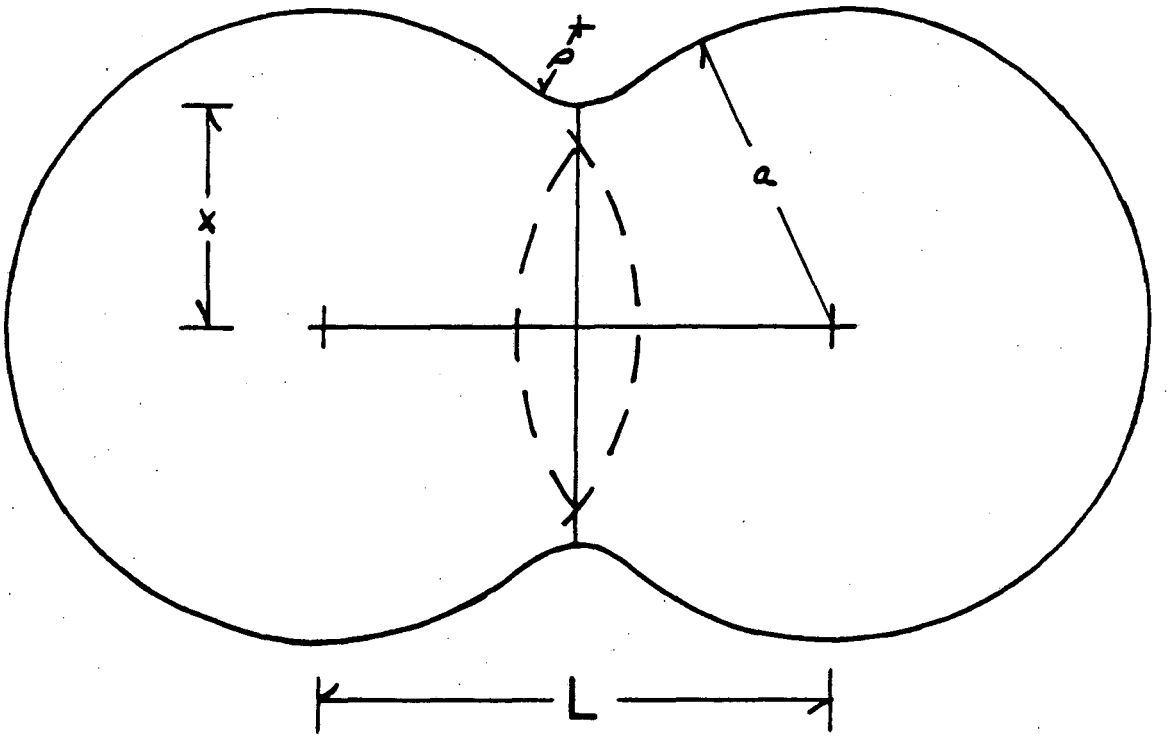

XBL 8412-5338

Figure 2.2 The two sphere model with the definition of the geometric parameters. The sphere radius is a, the half diameter of the neck is x, the minor radius of the neck is ρ, the interparticle distance is L.

Solving for the constants gives.

$$C_1 = \frac{4\gamma}{x^3} + \frac{2K\gamma}{x^2} - \frac{2F}{\pi x^4} \tag{2.8}$$

$$C_3 = \frac{2F}{\pi x^2} - \frac{4\gamma}{x} - K\gamma \tag{2.9}$$

The atomic flux due to a stress gradient is given by.

$$J = -\frac{D_b\,\delta_b}{kT}\,\nabla\sigma \tag{2.10}$$

Evaluation of equation 2.10 at the maximum radius and multiplication by the grain boundary perimeter gives the total atomic flux out of the grain boundary.

$$J_{total} = \frac{4\pi D_b\,\delta_b}{kT}\left[\frac{2F}{\pi x^2} - K\gamma - \frac{2\gamma}{x}\right] \tag{2.11}$$

The volume flux is simply the atomic volume times the atomic flux and the shrinkage rate is the negative of this volume flux divided by the area of the sintering neck, πx^2.

$$\frac{dL}{dt} = \frac{8D_b\,\delta_b\,\Omega}{kT}\left[\frac{K\gamma}{x^2} + \frac{2\gamma}{x^3} - \frac{F}{\pi x^4}\right] \tag{2.12}$$

This expression for the shrinkage rate due to the application of an axial stress in the two sphere model properly utilizes all of the parameters involved in the boundary conditions. In many of the past derivations one or the other of the parameters were neglected at various points in order to simplify the equations because it was felt that they were insignificant. As can readily be seen each of the three terms will make a contribution to the sintering rate. Some investigators have found it necessary to include an artificial factor to make the sintering due to grain boundary diffusion go to zero as the model goes to a columnar arrangement. This is a result of neglecting the second driving term in the situation of no applied force as shown in the following equations.

Equation 2.13 is the result when there is no applied force.

$$\frac{dL}{dt} = \frac{8D_b\,\delta_b\,\Omega}{kT}\left[\frac{K\gamma}{x^2} + \frac{2\gamma}{x^3}\right] \tag{2.13}$$

Exner [13] gives an approximation for the neck radius in the plane of the cross section shown in figure 2.2. Utilizing a numerical solution for combined surface and grain boundary diffusion, he found that this approximation holds for all but the smallest neck radii. Use of this approximation yields an expression for the total curvature at the intersection of the grain boundary and the neck surface.

$$K = \frac{5x - 4a}{x^2} \tag{2.14}$$

Inserting this expression into equation 2.13 and combining terms gives.

$$\frac{dL}{dt} = \frac{8D_b\,\delta_b\,\Omega}{kT}\left[\frac{7\gamma}{x^3} - \frac{4a\,\gamma}{x^4}\right] \tag{2.15}$$

From this expression it is obvious that the driving force and shrinkage rate both go to zero as the neck radius approaches 57 % of the particle diameter when all of the terms are retained.

2.2 Three Particle Model

The three particle model is one step up in complexity from the two particle model in that it attempts to look at how a pair of neighboring necks influence each other. Exner and Petzow [12,13] have worked extensively in this field and have come to the conclusion that asymmetric necks form and cause a torque that lies in the plane of the sintering neck as shown in figure 2.3. Their experimental results are depicted in figure 2.4 and show that the interparticle angle decreases during the early portion of sintering and then shows an increase in the

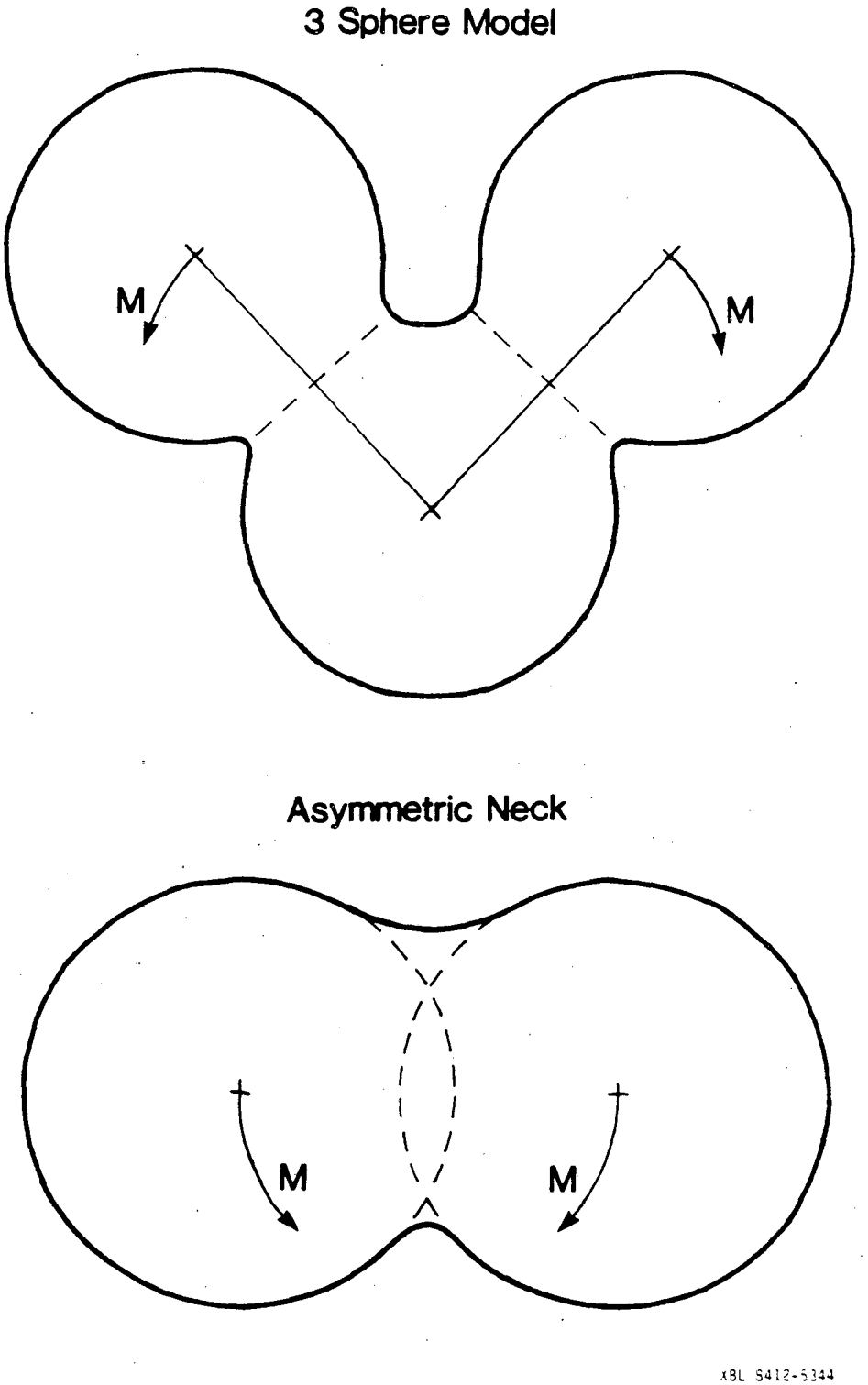

Figure 2.3 The three sphere model illustrating the bending moment due to an asymmetric neck.

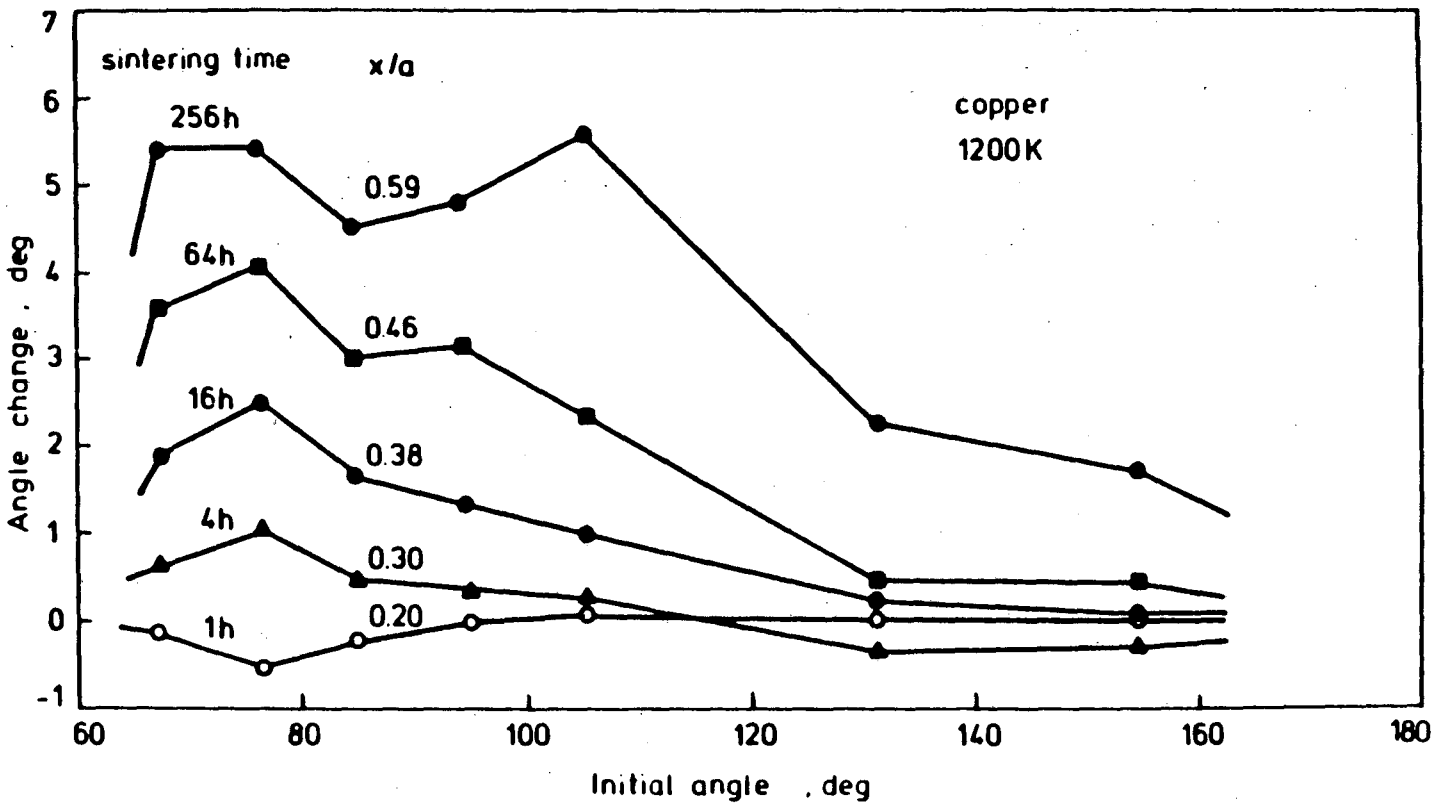

XBL 8410-4082

Angle changes of three particle models made of copper spheres as a function of initial angle during sintering at 1200 K.

Figure 2.4 The experimental results of Exner [13].

later stages of sintering. This change in the interparticle angle is relatively large, 4 to 8 degrees, for small initial angles, 60 to 90 degrees, and is rather small, less than 2 degrees, for initial angles greater than 140 degrees. This trend is seen in both crystalline and amorphous materials, so it can not be an effect exclusively due to grain boundary tilting. Our work will show that the angular changes in two dimensional arrays of spheres are both much greater in extent and not as systematic as shown by Exner and Bross.

Bross and Exner [5] have used a computer simulation of the neck between two cylinders to determine how far the zone of influence extends from the neck and how this influences the formation of asymmetric necks. They concluded that the zone of influence was much larger than the commonly used tangent circle model predicted and that this would allow the necks to impinge upon each other and form asymmetric necks at relatively small neck widths. They also simulated an asymmetric neck between cylinders and found that it should cause a rotation of up to 1.9 degrees [14]. All of this work is summerized in Exner's reveiw paper [13].

Hsueh and De Jonghe [19] have found an analytic expression for the effect of both a bending moment and an applied stress on a sintering neck between cylinders. Analysis of this result leads to the conclusion that an additional sintering neck located off the axis of symmetry of the necks of interest can exert moments that are comparable and even larger than that from asymmetric necks. A simplified geometry that might give rise to this effect is depicted in figure 2.5. It appears that the formation of asymmetric necks does lead to particle rotation and whence rearrangement. It will be shown in this work that this is a minor effect compared to the bending moment generated by the

Bending Moment due to Off Center Sintering Neck

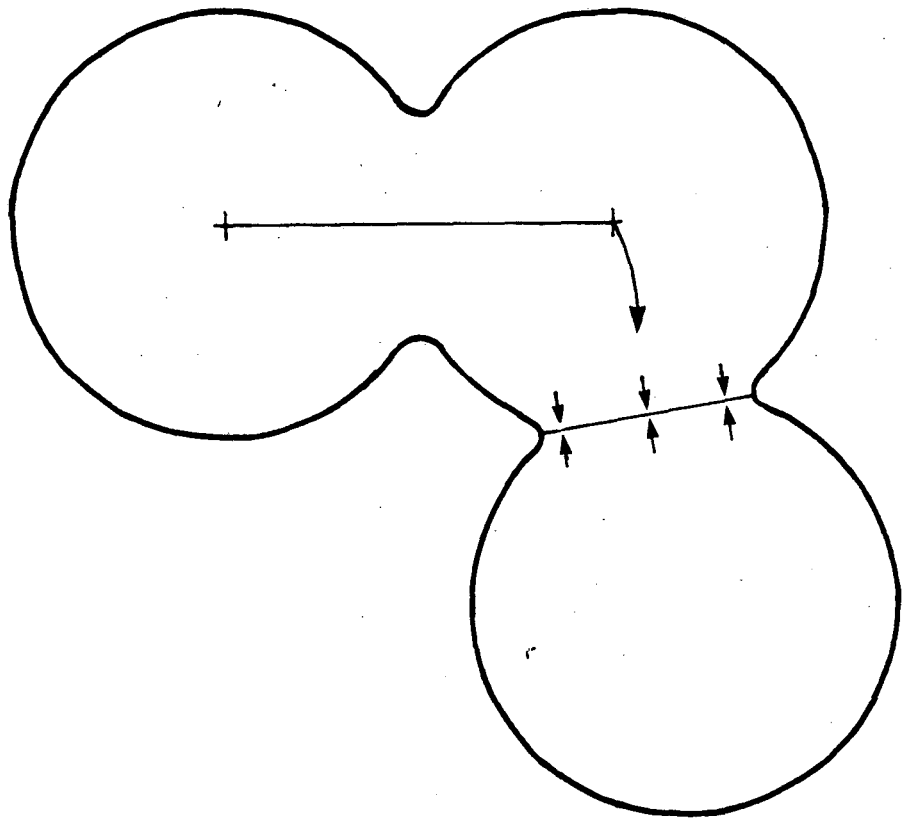

XBL 8412-5343

Figure 2.5 Schematic diagram showing how the shrinkage of an off center sintering can cause a bending moment in a nearby neck.

nonsymmetric arrangement of neighbors in multiparticle compacts. The studies of the three particle model have helped to define some of the perturbations on the two particle model that appear to apply in real sintering compacts.

2.3 Multiparticle Arrays

The term multiparticle array is used here to mean two dimensional irregular arrays of particles. All of the known multiparticle array studies that have been preformed have used spherical particles spread upon a plate, although it might be possible to use a random bundle of rods so that the forces in the neck could be handled more easily in a simulation. These arrays are used to study the interactions of the sintering necks across more than just the intervening surface of the central particle. The advantage of these arrays is that they are much closer to a three dimensional powder compact than the two particle model but they are simple enough so that the individual particles may be monitored during sintering.

After the three particle sample discussed previously the next step in complexity of sintering experiments are the closed loops of 4 to 15 spheres employed by Exner [13]. In these experiments he found that the loops tended to become more circular as a function of the degree of sintering. This was attributed to the formation of asymmetric necks which tended to maximize all of the interparticle angles in the loop. The large scale random array of spheres was first used by Barret and Yust [3] who concluded that centers of densification formed in the areas of relatively high initial density. As these centers of densification shrank they could cause the formation of porosity in the areas of relatively low density by shrinking away from them. They felt these areas of densification would then

eventually sinter together because they were connected by bridges.

Eloff and Lenal [10] propose that there are mechanical constraints in the two and three dimensional arrays that inhibit neck growth and shrinkage. They found that both shrinkage and neck growth were decreased as the experiment progressed from one to two to three dimensional sintering arrays. Their two dimensional arrays were found to form fissures and and as a result selected areas had higher local densification than the overall array. After the initial breakage and formation of new sintering necks they found that new necks formed slowly and would have little effect upon the shrinkage in the later stages of sintering. Pask and Hoge [27] felt that from a thermodynamic standpoint it was possible for the matrix to constrain areas of low density from further sintering. Exner, Petzow, and Wellner [11] state that the only way that mechanical constraints can arise is if a force such as substrate friction is applied from outside of the array. They further state that chains can only be broken if the ends are held fixed by these outside forces. However, Exner and Petzow [12] exhibit micrographs of two dimensional arrays of spheres that clearly show stretched necks in arrays that were asserted not to adhere to the substrate.

The most comprehensive studies to date of two dimensional arrays of spheres have been those of Exner et al. [11,12,13]. In all of these studies they find that substantial rearrangement occurs by complex mechanisms. It is found that small pores exhibit normal shrinkage and that large pores grow and tend to become more rounded. During the intermediate stages of sintering ($0.2 < \frac{x}{a} < 0.3$) interparticle contacts were observed to rupture and at later stages new contact formation predominated. They state that it is the formation of asym-

metric necks and the resulting torques that cause this behavior. This assertion is justified by citing that the rupture of contacts begins at the same time that the asymmetric necks begin their increase in angle in the three particle models.

There are a few common problems to all of these studies of multiparticle arrays of spheres. All of the experiments were carried out as a series of heat treatments followed by microscopic analysis. This thermal cycling can give rise to stresses and deformations of the network that would not occur in an isothermal situation. Transfering the sample to a microscope slide to allow observation can induce localized stresses in some necks which can change the behavior of the neck. Using a polished saphire flat as a substrate eliminates the transfer problem but we found that copper, the most frequent model material, adhered slightly to it. Since the sample must have enough structural integrity to stay in one piece it was necessary for all researchers to presinter their sample before the first micrograph was taken. This results in the loss of data on the earliest stage of sintering even though all researchers conclude that the amount of rearrangement occurring at the later stages of sintering is limited. It appears that the multiparticle study has given us a great deal more information about rearrangement but it has not been as fully exploited as it should be in allowing extrapolations to the three dimensional case.

2.4 Computer Simulations of Sintering

The computer simulation of the sintering process can take on three forms, neck geometry and material transport, average particle simulations and sintering maps, and discrete particle simulations. The neck geometry simulators were mentioned in section 2.2 and have improved our knowledge of how different

material transport mechanisms interact. They have also shown that the simple tangent circle approximation is actually rather crude, however these simulations are of little importance to the current work. The average particle simulators and sintering maps attempt to extrapolate the two sphere model into the three dimensions for the average particle. The intent of this type of work is to allow the prediction of the sintering behavior of a compact in real use. The discrete particle simulators extrapolate the two particle model into three dimensions by considering how all of the necks interact throughout the compact. This type of simulator can potentially yield the most information about sintering because it allows the more easily seen and understood one and two dimensional experiments to be compared with the three dimensional case.

2.4.1 Sintering Maps

Sintering maps were developed by Ashby [2] to help predict the behavior of a particle compact under a given heat treatment. These diagrams map sintering rate and mechanism on to plots of neck size versus temperature. Swinkles and Ashby [31] later refined the method of calculating these maps to include particle rearrangement and improved models of the material transport. Ashby's maps show only the most dominant of the six mechanisms that are known to cause neck growth. Mohan, Soni, and Moorthy [25] have created similar diagrams which show the relative contribution of all mechanisms. It should then be possible using either of these techniques to select a heat treatment schedule to bring about the desired microstructure in the sintered body. Unfortunately, doing the calculation for an average particle assumes that the particle packing is roughly homogeneous; homogeneous packings are rarely encountered in real compacts.

Swinkles and Ashby account for the shrinkage due to rearrangement by allowing the number of contacts to increase as the density increases according to the relationship.

$$NC = 16 \left[\frac{\rho_{actual}}{\rho_{theor.}} \right] - 2 \tag{2.16}$$

The influence of the impingement of neighboring necks on each other is accounted for by comparison with the regular packings of spheres of the same density. The average angle between contacts is set equal to the smallest angle found in the close packed planes of the regular arrangements with interpolation at intermediate densities. Neither of these assumptions do a very good job of modeling a real three dimensional compact. Bernal [4], Scott [30], and Frost and Raj [15] have shown that in dense random arrays of spheres the number of neighbors and angle between contacts is widely distributed. Jodrey and Tory [20] have calculated that in a green random dense compact both the number of nearest neighbors and the angle between contacts are distributed even more widely than in the arrays of steel spheres studied by the authors of the above papers. These sintering maps may prove useful as a rough guideline for the selection of a heat treatment schedule for a compact but the amount of information that they provide about the nature of sintering is quite limited.

2.4.2 Discrete Particle Simulators

The discrete particle simulator calculates the behavior of all of the sintering necks and their influence upon the neighboring particles. By making these detailed calculations for all of the necks and particles it is possible to observe the effect of the packing inhomogeneity. This packing inhomogeneity can make the environment, and whence the sintering behavior of two nearby particles,

radically different. However, this increase in the detail of the analysis is paid for very heavily in computation time. As a result it is necessary to make some approximations in this type of simulation so that a reasonably large sample size can be used so that a particular particle packing does not dominate the results.

The first simulator of this type was created by Hare [17] and makes some simplifications that are somewhat hard to justify. This work proposes to seperate the sintering process into two distinct processes; rearrangement and densification. It then does the calculations at the level of each sphere instead of each neck. Densification is simulated by enlarging the sphere diameter by an amount proportional to the average expected interpenetration of each of its necks and then normalizing the entire compact. This method fails to take into account the fact that smaller necks will both grow and interpenetrate at a faster rate than larger necks. Rearrangement was simulated by finding the vector sum of the force due to sphere interpenetration at each neck and displacing the center a distance proportional to this vector sum. The problem with this is that a large neck will contribute very little to the vector sum but it will strongly inhibit particle motion.

These two processes are combined by determining which one leads to the largest decrease in the surface area and applying that process to the entire compact in a very small step. This either/or selection totally fails to account for packing inhomogeneities and the fact that sintering is a process composed of both densification and rearrangement occurring at the same time. The inhomogeneity of the packing would probably make it advantageous for one mechanism or the other to predominate on the local level while the mechanism was observed to alternate for the entire compact. The final problem is that part of

the compacts are of too low a density (0.4 theoretical) and coordination (2.3 contacts) to be mechanically stable when working with compacts of spheres.

The simulation of Ross, Miller and Weatherly [29] involves both two and three dimensional arrays of spheres in both dense and loose arrangements. This work recognizes that a new contact will sinter rapidly and cause rapid center to center approach and set up compressive stresses in the neighboring necks. It finds the expected shrinkage in each neck and then employs an averaging procedure involving the neighboring necks in triangular arrays. This method is similar to the stress relaxation that must occur between nearby necks shrinking at different rates but the averaging method is hard to justify. This simulation uses the Voronoi cell of the particle to measure the local density for that particle. The Voronoi cell is defined for a two-dimensional array of points in figure 2.6 and this is then related to a two-dimensional array of spheres in figure 2.7. This method uniquely associates a portion of the porosity with each particle, since during the early portion of the sintering process it is the particles and not the pores that are discrete. Ross et al. come to the conclusion that the the lower shrinkage observed in looser compacts is a result of chain straightening. However, it is hard to perceive of a real three-dimensional compact having the extent of non- interconnected chains that they seem to find.

The work that has been done in the area of discrete particle simulators makes the leap from the one dimensional model to the complex case of a compact without detailed analysis of how the sintering particles interact. This oversight then leads to approximations that don't seem to make much physical sense. As a result the amount of information gained from them has been severely limited.

VORONOI CELLS

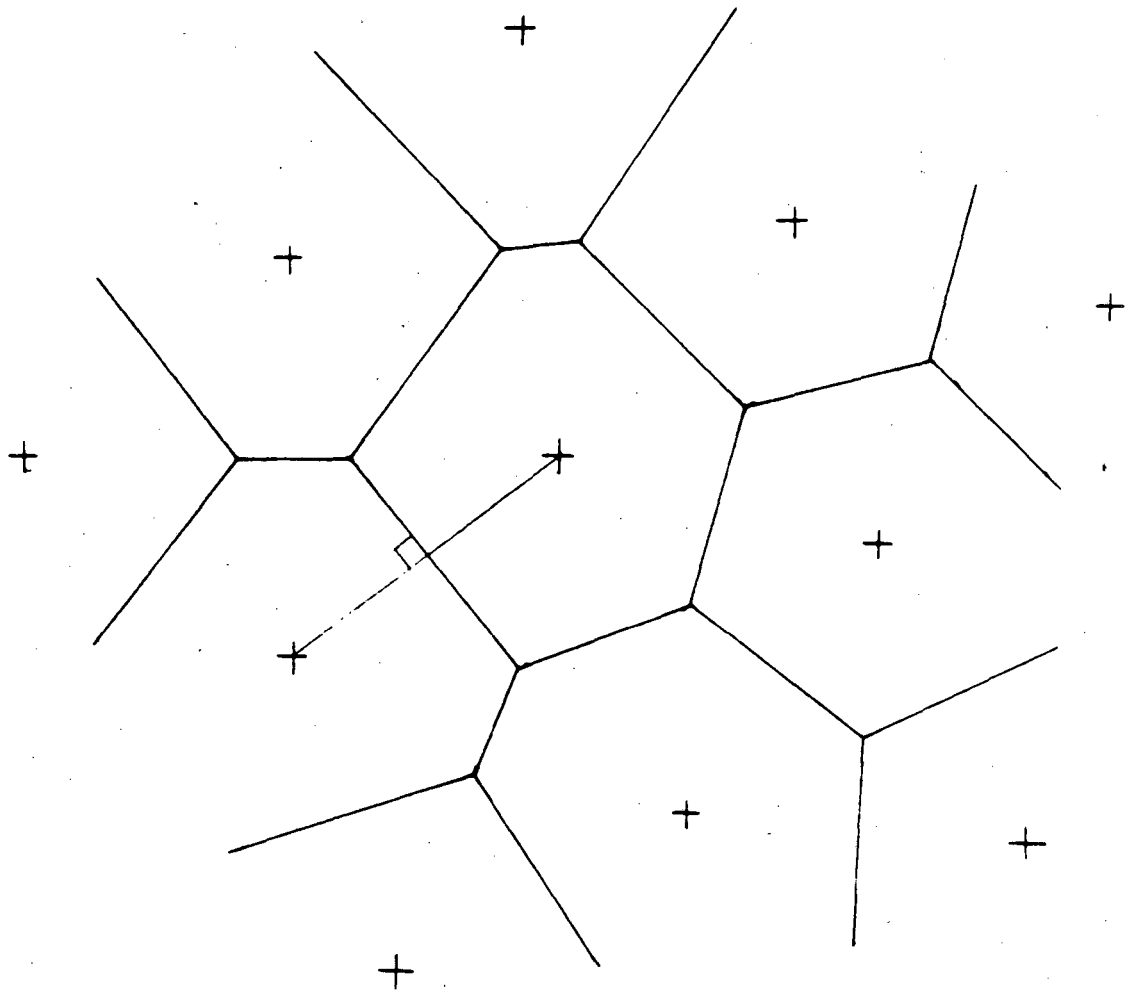

XBL 8410-4498

Figure 2.6 The Voronoi cells of a two-dimensional array of points. The cell is formed by first drawing the perpindicular bisectors of the lines connecting the points. The Voronoi cell is then the smallest area enclosed by the bisectors around each point.

VORONOI CELLS

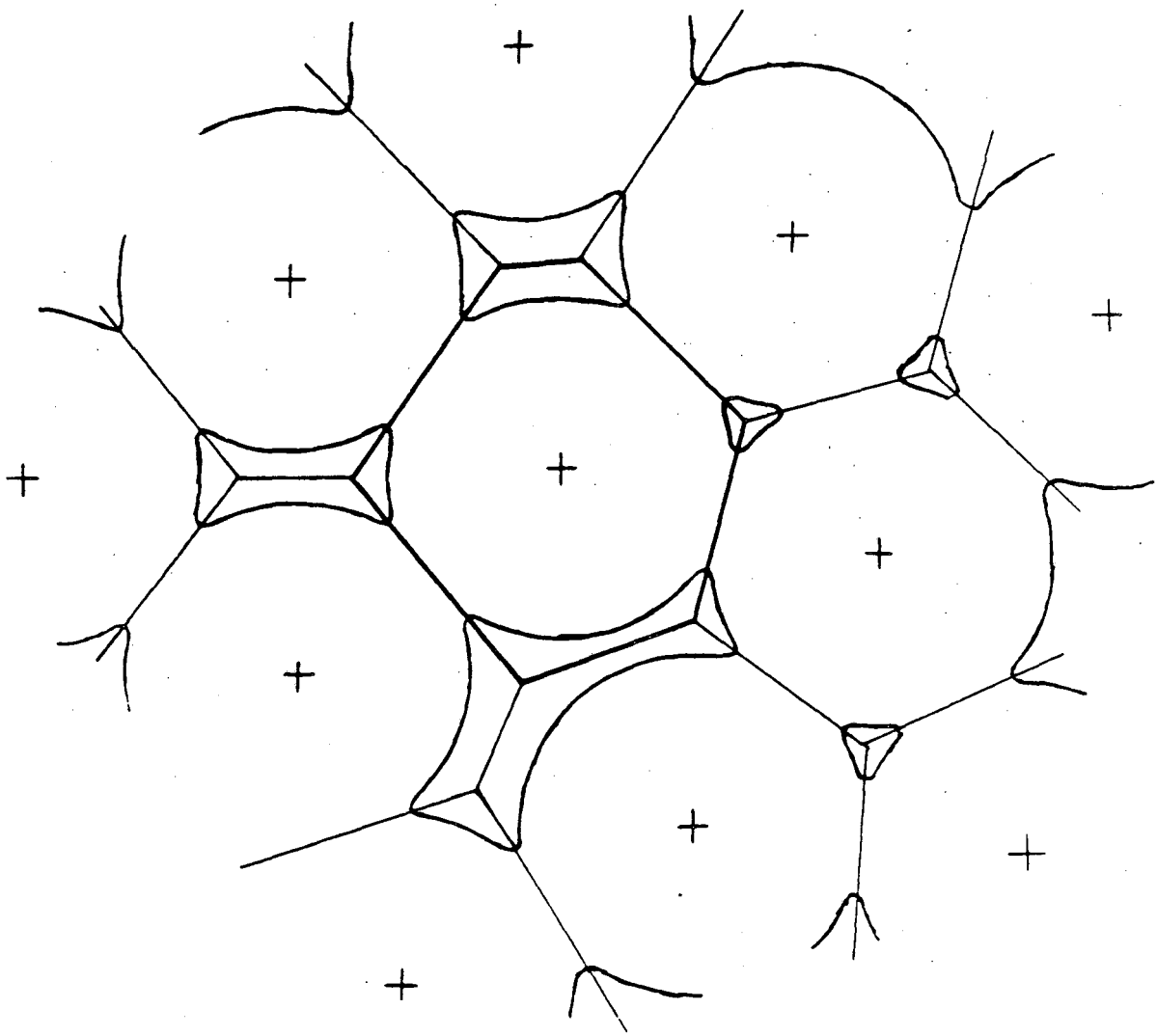

XBL 8412-5386

Figure 2.7 The Voronoi cells for an array of spheres. The center of each sphere is used for the points in figure 2.6.

3 Experimental Procedure

In this study a spherical copper powder was spread in a monolayer on a vitreous carbon substrate and sintered. A hot stage optical microscope was used to take a series of micrographs as a function of time of the same area of the array for analysis. These micrographs were then numbered so that each sphere could be followed as a function of time regardless of the amount of rearrangement that had taken place. The location of the sphere centers was then digitized so that the quantities of local density from the Voronoi cell area, nearest neighbor distance, and interparticle angle could be calculated.

3.1 Powder Preparation

The spherical copper powder used in this study was prepared from a high purity copper powder purchased from Alfa Chemical. Upon receipt the powder was sieved multiple times to eliminate all particles outside of the 37 to 45 micrometer range. The powder was then formed into spheres as suggested by Herrmann et al. [18] by thinly dispersing it upon a vitreous carbon plate and heat treating in an atmosphere of 95 % nitrogen and 5 % hydrogen. This heat treatment consisted of the melting of the copper at 1400 K and the subsequent natural cooling of the tube furnace. Since the molten copper does not wet the vitreous carbon surface it beads up into very good spheres. Upon examination in the SEM no flats of diameter greater than 1 micrometer were ever observed. The resulting spherical powder was then re-sieved in order to eliminate all particles outside of the 37 to 45 micrometer range. The particle size distribution is shown in figure 3.1.

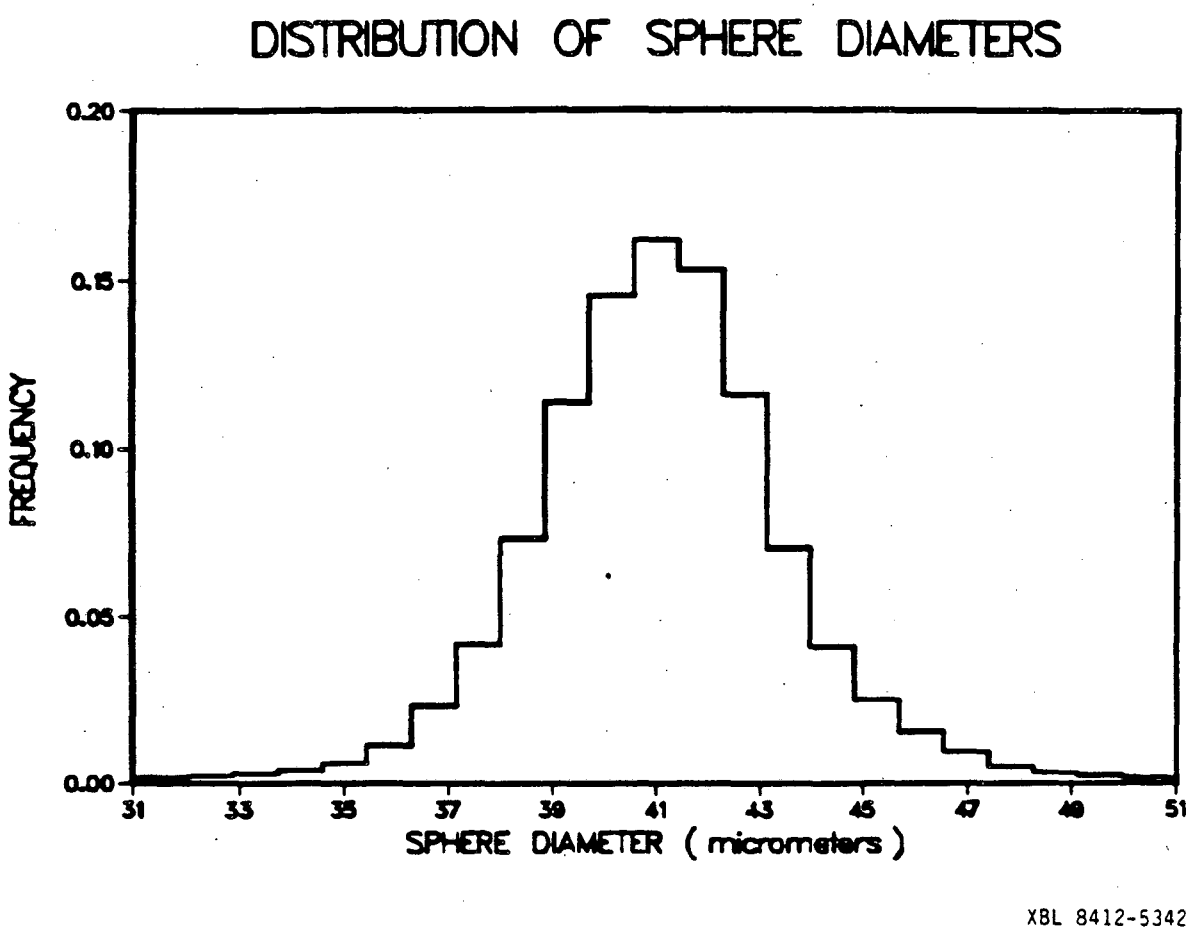

Figure 3.1 The distribution of the diameters of the spherical copper powder.

3.2 Sample Preparation

The vitreous carbon substrates were 10 mm diameter disks, 2.5 mm thick that had been polished using 0.25 micrometer diamond paste. The sample was prepared by placing a small quantity of the spherical powder upon a disk. A second disk was then placed over the powder and gentle pressure and vibration were applied in order to flatten the pile of spheres into a monolayer. During this dispersion great care was taken in order to prevent the formation of flats upon the spheres, if any such flats were observed a new powder sample was used. The vitreous carbon substrate was chosen in order to prevent the adhesion of the particles to the substrate. A test was preformed to find the best substrate material, during an extreme sintering case (1325 K and 120 hours) the copper spheres did not adhere to the vitreous carbon while they did adhere to the single crystal sapphire as had been used in some previous work.

3.3 Hot Stage Optical Microscopy

During the early experiments the partially sintered sample was observed to slide off the substrate whenever any movement of the sample was attempted. Extreme difficulty was also encountered in trying to find the same area of the sample after the inevitable sample sliding. By using a hot stage optical microscope it was possible to eliminate the above problems as well as the errors that can be induced by heat up and cool down effects. An optical microscope was used because the vapor pressure of copper in the 1200 to 1300 K range is approximately 10^{-1} Pa while the SEM requires a vacuum of at least 10^{-4} Pa. The loss of resolution due to the use of an optical microscope was not considered to be a major problem as this study was not intended to examine the

neck curvatures and would have a large number of particles to examine the data in a statistical manner to remove any errors.

The hot stage microscope was constructed around a Zeiss metallograph for the optics. I built the hot stage assembly which was composed of a small furnace and heat sink, a cover jar with an optical quality quartz viewport, gas inlet and outlet, and a shutter to prevent fogging of the viewport with copper vapor during the experimental run. A schematic drawing of a cross section of the hot stage assembly is shown in figure 3.2. The experiment was run in an atmosphere of 90 % argon, 9.5 % nitrogen, and 0.5 % hydrogen at approximately 250 Pa above atmospheric. This atmosphere was selected to prevent the oxidation of the copper sample and to minimize the deterioration of the vitreous carbon surface due to attack by the nitrogen and hydrogen. The micrographs were taken on Kodak Panatomic-X and developed using Kodak Microdol-X to achieve fine grain and high contrast in the negatives.

3.4 Image Analysis

Enlargements of the 35 mm negatives were made in order to make the size of the spheres large enough for easy and accurate analysis. For digitizing the sphere center locations 25 cm by 50 cm enlargements were made, this resulted in a sphere image diameter of 16 mm and a total magnification of 380 X.

3.4.1 Digitizing the Sphere Center Coordinates

The first step in digitizing the coordinates of the sphere centers was to number each of the spheres in each photograph. This numbering was done to make it possible to keep track of the location of each sphere at every time during the sintering run. The numbers were chosen so that the first N spheres were

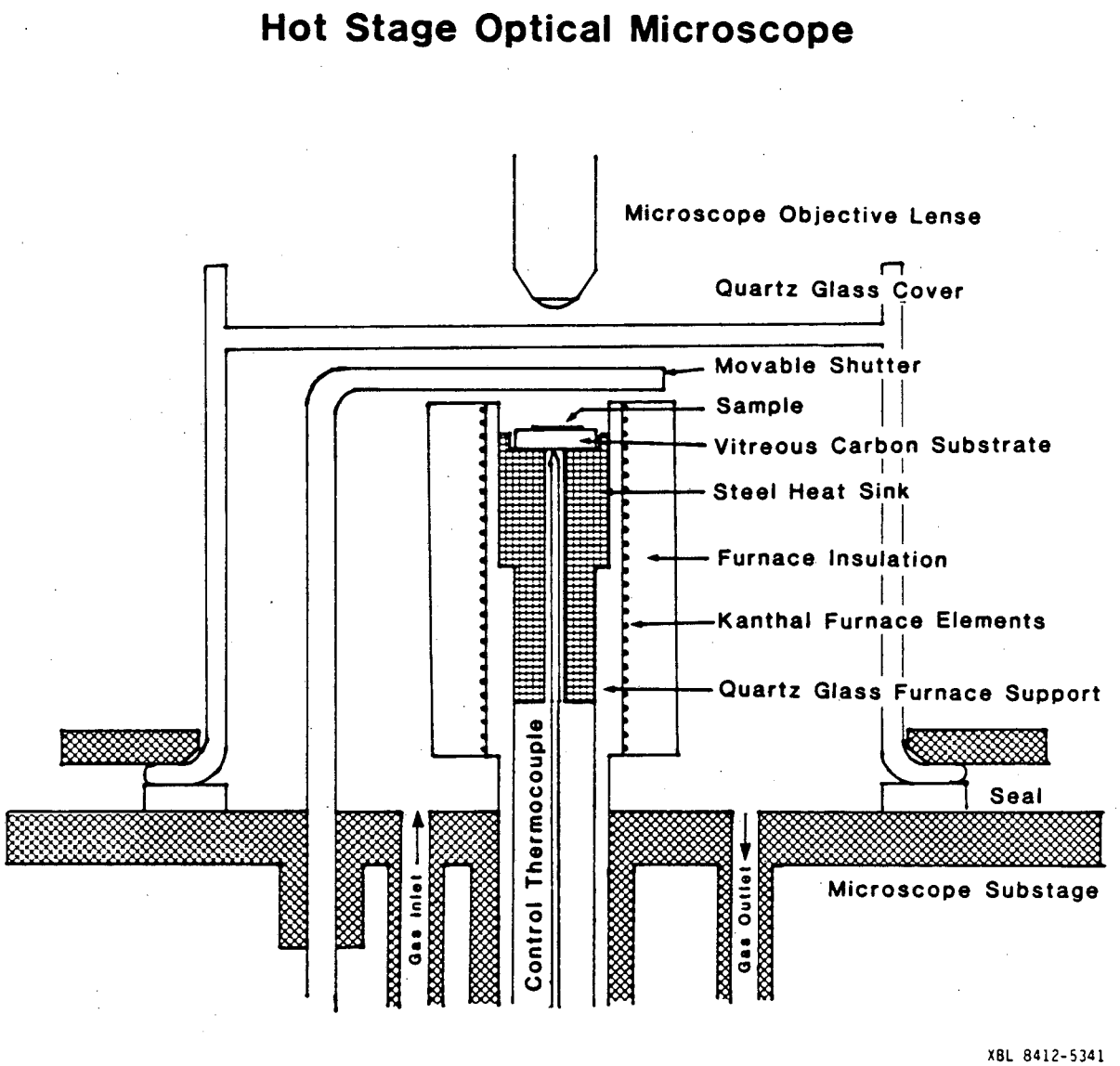

Figure 3.2 Schematic Diagram of the hot stage optical microscope.

inside a ring formed of the remaining spheres. These centrally located N spheres could then have the full set of data derived about them. Due to the slight movement of the field of view during refocussing it was necessary to make sure that all of the initially selected spheres appeared on each of the subsequent micrographs.

The location of the sphere centers were digitized by picking three points as far apart as possible on the circumference of the circle that was the projection of the sphere on to the micrograph. These points were used to calculate the center coordinates and radius of the projection of the sphere. If it was not possible to find three satisfactory points then the center location was approximated by eye. It was necessary to resort to this second method less than 3 % of the time. Since the enlargements were larger than the digitizer surface it was necessary to combine the coordinates from the different files created as the different areas of the enlargement were placed on the digitizer. This was done by finding the spheres that were common to both files and then making the appropriate rotation, translation, and dilation in the file to be added in order to bring them into the best possible coincidence.

3.4.2 Normalization of the Center Coordinates

Since it was not possible to keep the focus constant during the entire experimental run due to changes in thermal expansion and field of view, it was decided that the sphere center coordinates would have to be normalized after digitizing. This was accomplished by setting the average value of the radius at each time equal to 1.0 and making the appropriate dilation of the sphere center locations.

3.5 Derived Quantities

The derived quantities used in this study are the local density, the interparticle angle, and the nearest neighbor distance. However, before these quantities could be derived it was necessary to make an accurate list of the nearest neighbors at each time for every sphere. This was accomplished by having the computer find a set of approximate neighbors, (all spheres within 1.15 diameters), and editing the list by hand to remove any that did not actually make contact.

The local density associated with a sphere is defined as the average projected sphere area divided by the Voronoi cell area associated with that sphere as shown in figure 3.3. This definition of the local density not only takes the packing density into consideration but also the variation in the sphere diameter. A smoothing procedure was used on the local density versus time for a particular sphere in order to prevent the small amount of uncertainty (approximately 1%) in the location of the sphere centers from causing larger errors in the rate of change of the local density. This smoothing was accomplished by fitting a smooth curve with 4 adjustable parameters to the local density data versus time for each sphere. The effect of this smoothing is shown in figure 3.4 where both the smoothed and unsmoothed data are plotted for three representive spheres.

The interparticle angle was defined as the angle between a pair of nearest neighbors of a center sphere. These angles were found by starting with the first neighbor above the horizonal axis on the right side of the central sphere and moving sequentially around the center sphere in the counter-clockwise direction. Figure 3.5 shows a typical central sphere and its nearest neighbors along with definition of the interparticle angles. These data were also smoothed using a

LOCAL DENSITY

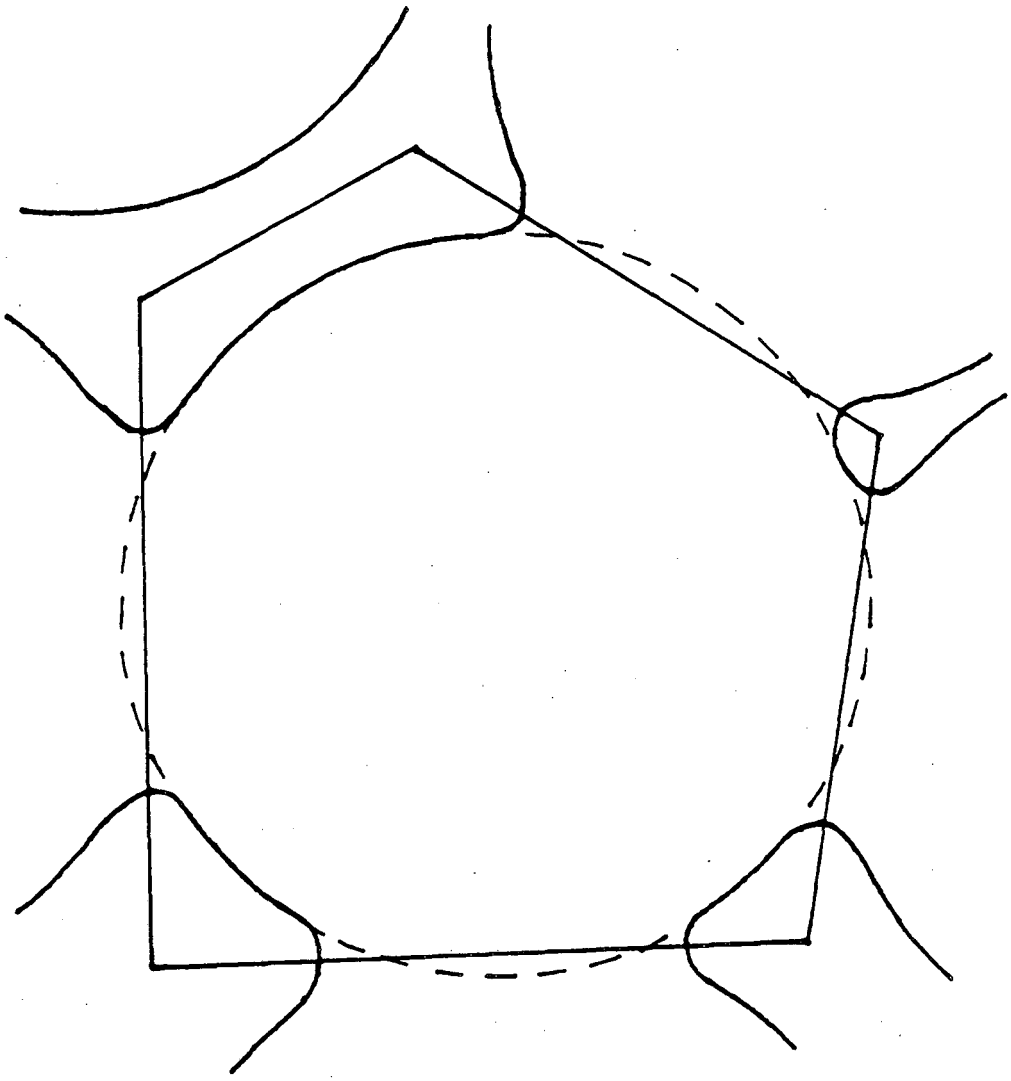

$$\text{Local Density} = \frac{\text{Projected Sphere Area}}{\text{Voronoi Cell Area}}$$

XBL 8412-5385

Figure 3.3 Definition of the local density as the projected sphere area divided by the Voronoi cell area.

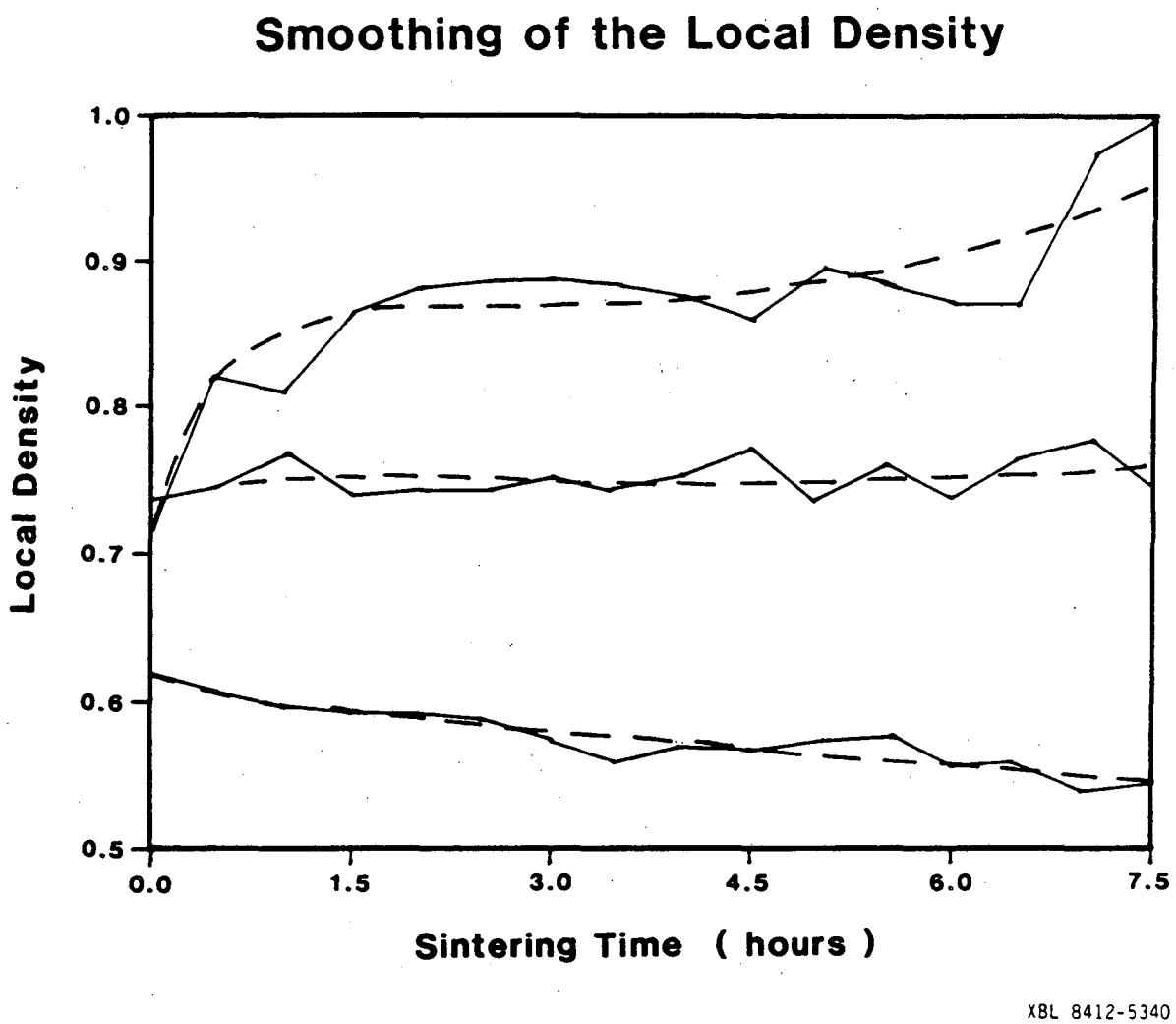

Figure 3.4 Example of the smoothing of the local density for three selected spheres. The dashed lines are the unsmoothed curves and the solid lines are the smoothed data that was used in this study.

Interparticle Angles and Distances

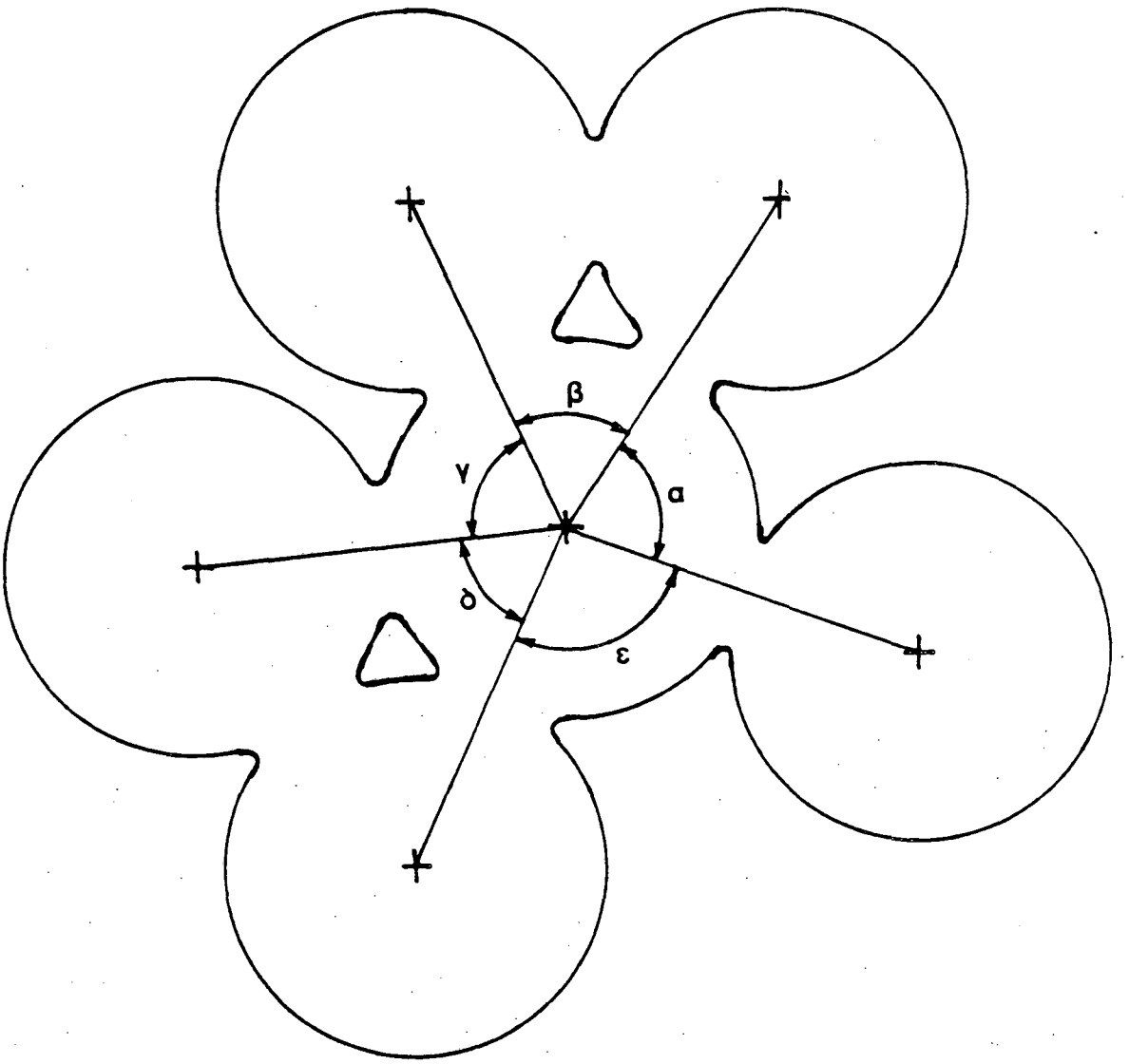

XBL 8412-5354

Figure 3.5 The definition of the interparticle angle and distance.

procedure similar to that for the local density in order to remove the fluctuations due to the small errors in measurement. The nearest neighbor distance is simply the distance between the centers of the spheres that are in contact with each other and is also shown in figure 3.5.

Much of the data presented in this study is in the form of distribution or frequency plots. In order to make these easier to interpret it was necessary to smooth the distribution curve before plotting. Since there was some degree of uncertainty in the actual value of a data point it was decided to assign the pseudo-gaussian distribution shown in figure 3.6 to each data point and then sum the contributions to form the distribution curve. This smoothing process has the beneficial effect of removing much of the noise from the curve and making interpretation easier with the minor disadvantage of spreading the distribution slightly. In figure 3.7 both a smoothed and unsmoothed distribution curve are plotted to demonstrate these effects.

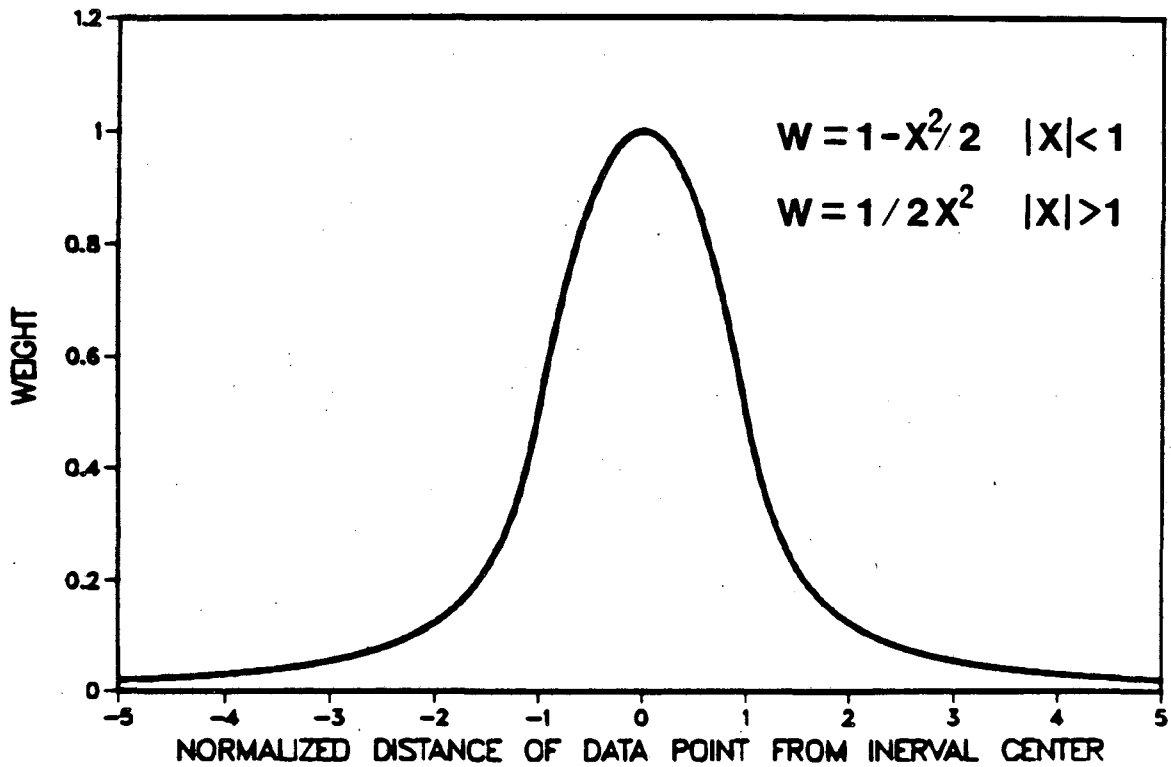

XBL 8412-5353

Figure 3.6 The pseudo-gaussian curve used to smooth the distribution data. This was used due to the sparseness of the data in some of the inervals.

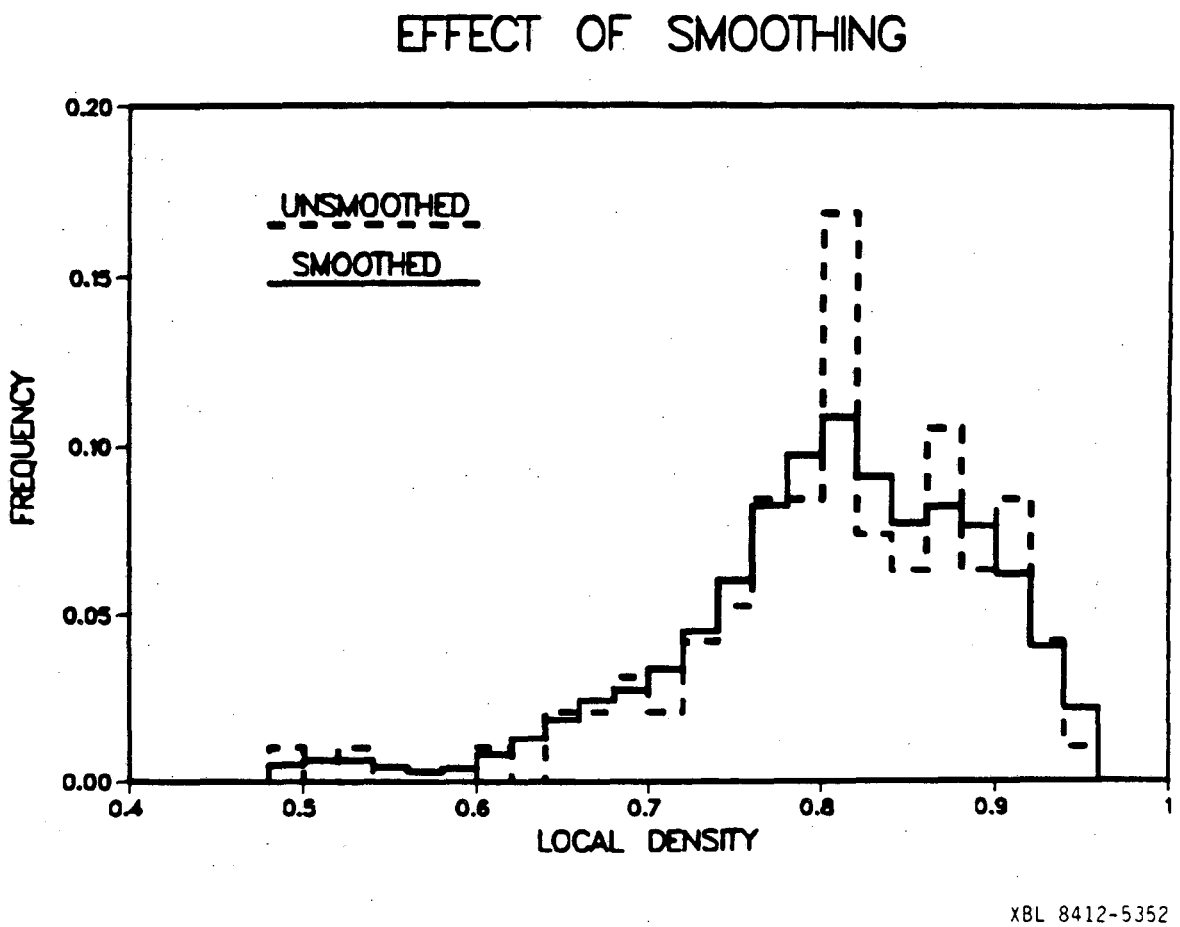

Figure 3.7 Example of the effect of smoothing, the dashed curve is the raw distribution and the solid curve is the smoothed version.

4 Results

The results used in this study were from the last two experimental runs out of a total of ten. The other eight runs were used to work out the details of the experimental procedure. These eight were discarded for one or more of the following reasons: small number of particles that appeared in every micrograph due to shifts in the image during sintering; blurred images at later stages of sintering due to the evaporation and condensation of copper on the veiwport; too many nonspherical particles; and the combination of time and temperature not being correct to give a good series showing rearrangement. Upon visual inspection of the micrographs these discarded experimental runs exhibited similar behavior to those that were analyzed in detail. For this reason it is felt that the results of the two completed experimental runs can be presented as representative examples and that valid conclusions can be drawn from them.

The two experimental runs that were used were labeled runs G and C. The samples for both runs were created by pouring approximately 8 milligrams of the spherical copper powder onto the substrate. This pile of powder was then flattened into a monolayer by applying gentle pressure to another smooth substrate as it was slid around on the pile of spheres. Both samples were heat treated for 12 hours at 200 C in the hot stage microscope in a 95% nitrogen - 5% hydrogen atmosphere to burn off any organics and remove oxygen from the system. For both experimental runs the overall samples were composed of approximately 8000 spheres. The area to be studied was selected to minimize the number of nonspherical particles and extremely large voids. The primary difference between the two runs was the temperature at which the isothermal heat treatment was carried out after the initial heat up which took

approximately 5 minutes.

For run G the sample was heat treated at 1260 K for a total of 7.5 hours after the initial heat-up. Prior to the initial heat-up, two micrographs were taken to establish the sphere locations at zero sintering. During the heat treatment at 1260 K a micrograph was taken every 30 minutes. In this experimental run the coordinates of 162 spheres were located on each of the 16 micrographs. Of the 162 total particles 118 of them were completely surrounded by the others so that the full range of derived data could be calculated for them.

Run C was heat treated at 1200 K for a total of 13.5 hours after the initial heat-up. A series of 10 overlapping micrographs were taken at each of 10 time increments of 1.5 hours including the initial set at zero sintering time. The number located in the lower right corner of some of the micrographs was imprinted on the negative when it was taken to identify each of the large number of very similar micrographs. Micrographs from the first 7 times were used with the sintering time running from 0 to 9 hours in 1.5 hour increments.

Only two of the 10 overlapping micrographs from run C were selected for study due to the very time consuming nature of the sphere location and digitization processes. Overlapping enlargements were made of half of each micrograph to provide the proper size image for the digitization process. An attempt was made to merge the four resulting coordinate files using the locations of the 30 to 60 spheres in the overlap to permit the calculation of the data for an array of approximately 400 particles. This did not work particularly well due to the slight distortions at the edges of the negatives and prints. Therefore separate sets of data were calculated for each of the 4 micrographs. This gave four arrays that had received identical heat treatment but had variations in

initial conditions.

The four arrays were composed of 140, 116, 110, and 100 total particles and were titled C1, C2, C3, and C4 respectively. Micrograph C1 shown in figure 4.1, had 95 internal particles and was fairly dense except for a long riplike void near the upper edge of the area that was used. Micrograph C2 shown in figure 4.2, had 75 internal particles, was located towards the center of the sample and had the highest density of any array studied here. The borders for this area were selected to avoid the large void in the upper right corner. Micrograph C3 shown in figure 4.3, had 72 internal particles, was located on the sample edge, and was exhibited quite a few relatively large voids. Micrograph C4 shown in figure 4.4, had 66 internal particles, was relatively near to the sample edge and was similar to C3 except that the voids were not as large. For some of the data types the four different areas show few differences in behavior, in this case they are treated together as run C. When the four areas do show significant differences in behavior they are treated separately.

Each of the different types of data was first calculated for each of the time steps. After inspection to make sure the program did not get stuck on an unusual geometry they were then combined by data type. The following sections examine the behavior of each of these types of data. The first section examines the overall characteristics of the arrays such as the density, densification rate, and the distribution of sphere coordination number versus time. This is followed by separate analyses of the local density, the interparticle distances, and the interparticle angles. These three sections give a detailed veiw of how the rearrangement process occurs at both the short range, local level and at longer range.

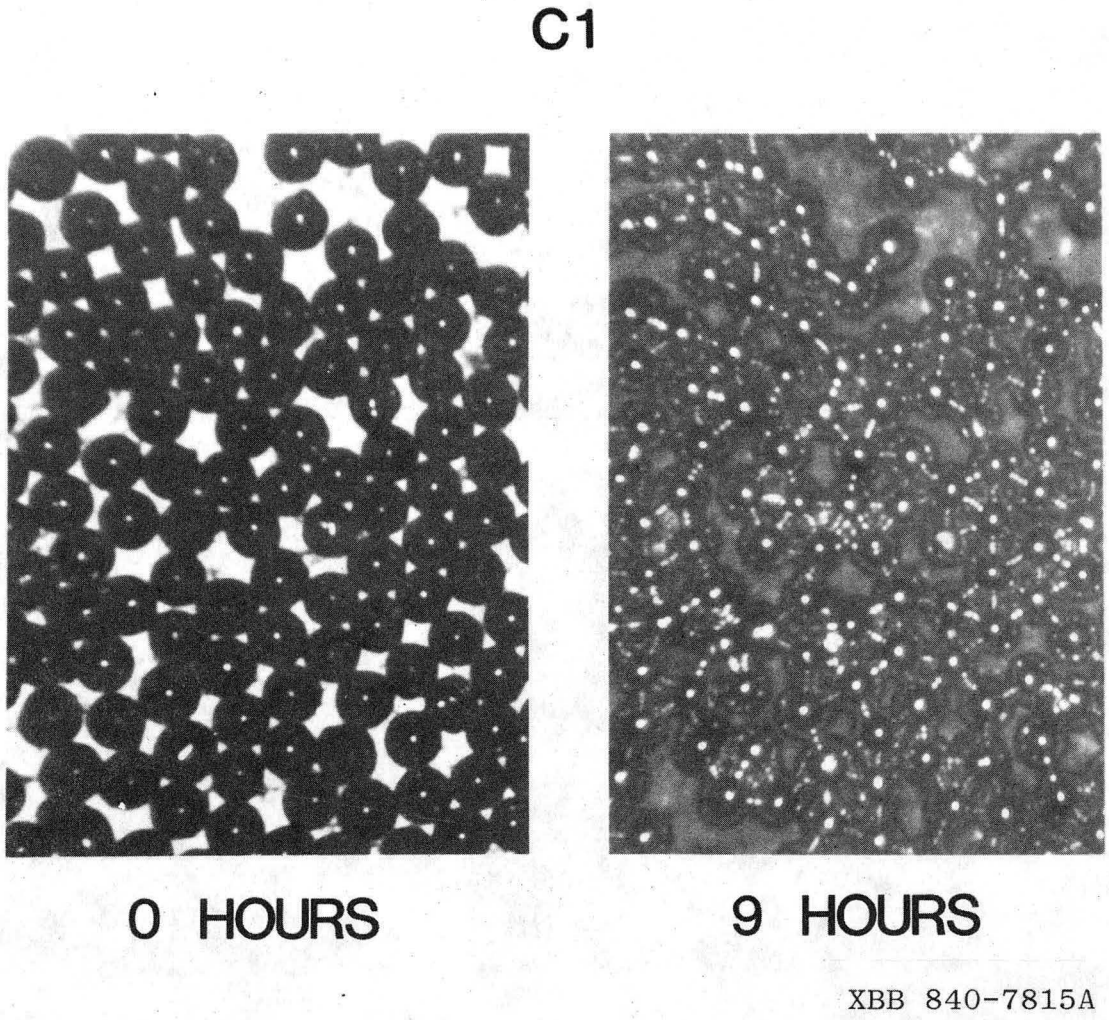

Figure 4.1 Micrograph C1, note the riplike void along the upper edge of the micrograph.

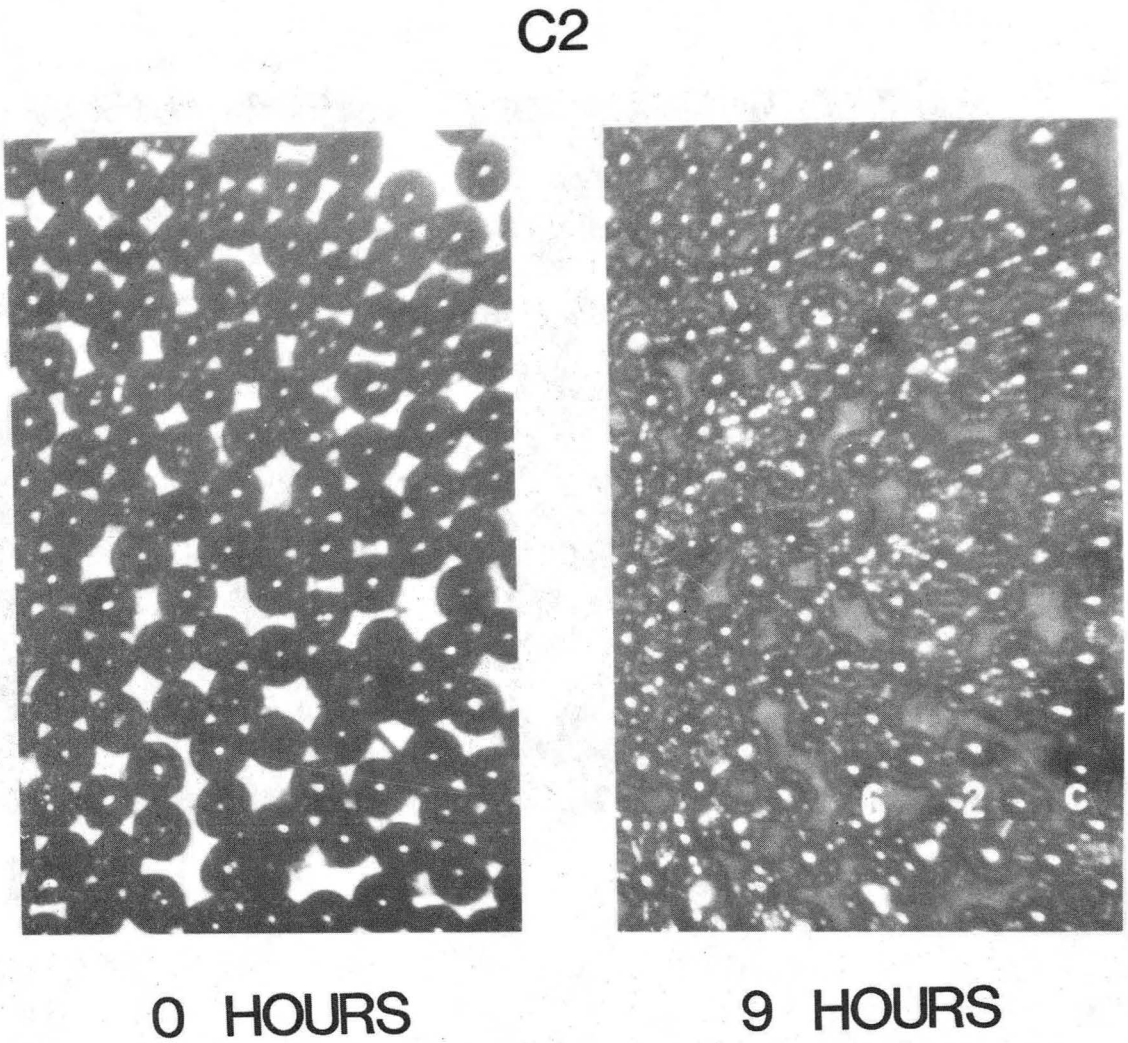

XBB 840-7816A

Figure 4.2 Micrograph C2, note the high density and relatively uniform densification.

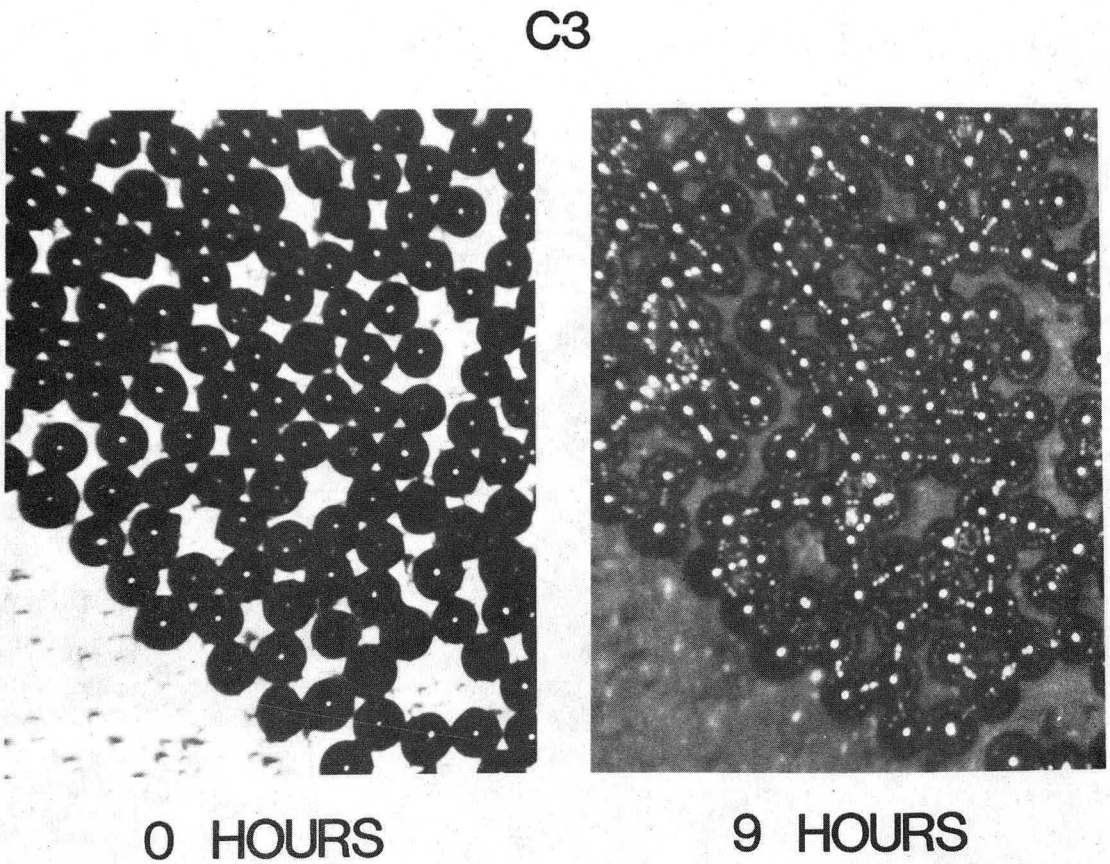

XBB 840-7817A

Figure 4.3 Micrograph C3, note the relatively large voids that have enlarged after sintering.

C4

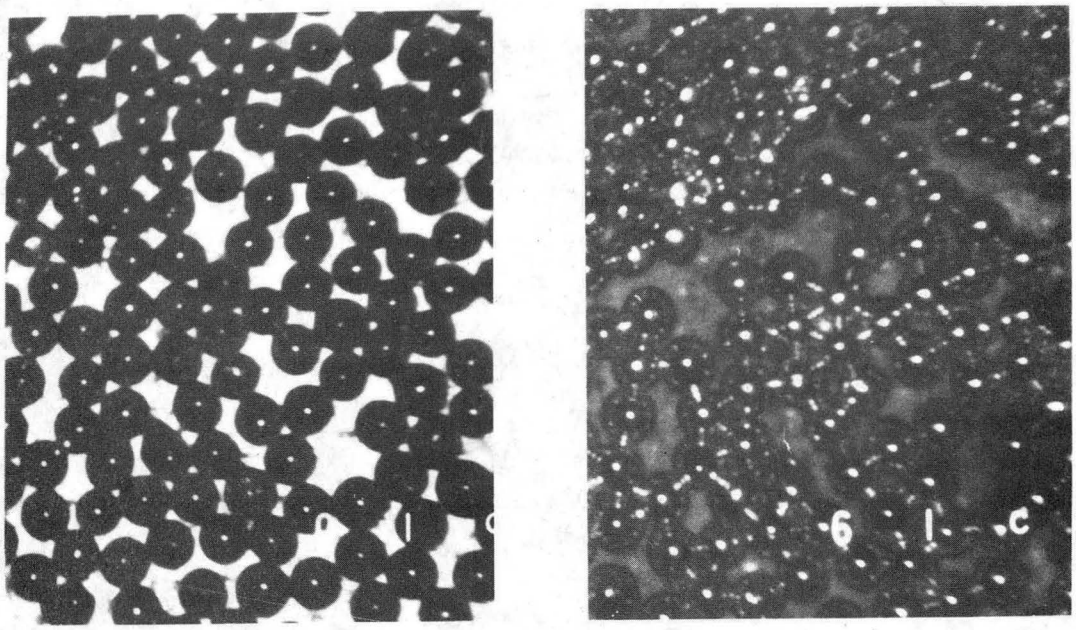

0 HOURS 9 HOURS

XBB 840-7818A

Figure 4.4 Micrograph 4.4, note the smaller voids than C3 and the formation of two prominent riplike voids that have formed after sintering.

4.1 Overall data

4.1.1 Density and Densification Rate

The density that is used in this work is the projected two-dimensional density as defined in figure 2.7. The Voronoi area is the reciprocal of the local density since the average sphere area has been. normalized to 1.0. The overall densities of the arrays were found by taking the average of the local densities for all of the interior spheres on each micrograph. All of the areas examined here in both experimental runs behave in the same overall manner; an initial rapid increase in density is followed by a period of slower densification as depicted in figure 4.5. Experimental run C at 1200 K continued to densify at a faster rate than run G at 1260 K after the initial rapid densification. This results in a higher relative densification of 10 % for the low temperature run versus 7 % for the run at the higher temperature. The lower relative shrinkage for the higher temperature run agrees well with the work of Swinkles and Ashby [31] and others that suggests that nondensifying mechanisms should tend to dominate at higher temperatures in the sintering of copper. The initial density for all of the areas range from 0.738 to 0.809, this is similar to the projected density of the regular square packing of 0.785. The final density ranges from 0.808 to 0.871 which is still less than the projected density of the regular hexagonal packing of 0.907.

The densification rate as used in this study is defined as the derivative of the area of the Voronoi cell for each sphere with respect to time. The densification rate and shrinkage rate used in this study are equivalent. Negative values of this rate mean that the Voronoi cell is shrinking. In this study shrink-

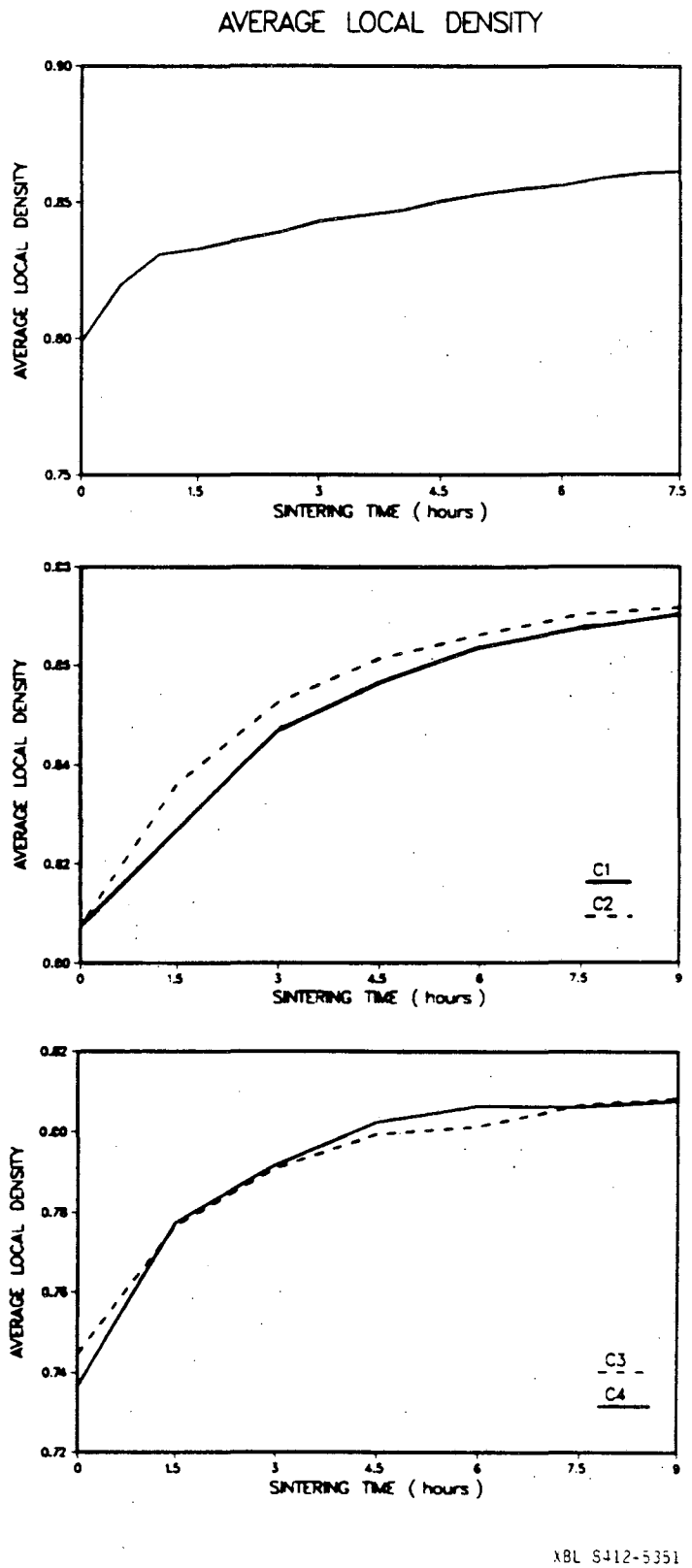

Figure 4.5 The average local density versus time for all five areas examined in this study. Run G is shown in the upper graph, runs C1 and C2 are shown in the middle, and runs C3 and C4 are shown in the bottom graph.

age is expressed as a negative densification rate. The overall densification rate was calculated both as the average of the local densification rates for each of the Voronoi cells and as the derivative of the overall density as function of time. This was done to check the method of calculating the local densification rate from a curve fit of the local density versus time, the two methods showed only slight differences in the values which showed that the smoothing did not distort the data.

The overall densification rates initially show a large shrinkage rate followed by a period of slower shrinkages shown in figure 4.6. This is just as expected from visual inspection of the graph of average local density versus time. Experimental run G has the fastest initial shrinkage, -0.082 , but the densification rate reaches a fairly low, stable value, -0.006, after only 2.5 hours. The four areas from run C have lower initial shrinkage rates, -0.037 to -0.064, than run G but they take much longer to approach the lower values than run G. The more rapid initial shrinkage in run G is a result of the faster kinetics of the higher sintering temperature but this quickly results in larger necks and slower sintering rates. The areas in run C all behave in roughly the same manner as run G. The initial average shrinkage rate for C1 is less than the others because of the opening of the preexistent large riplike void at the upper edge of the area. The overall densification behavior of the two-dimensional arrays of spheres studied here exhibits behavior that is consistent with the densification of three-dimensional compacts as seen in numerous previous studies.

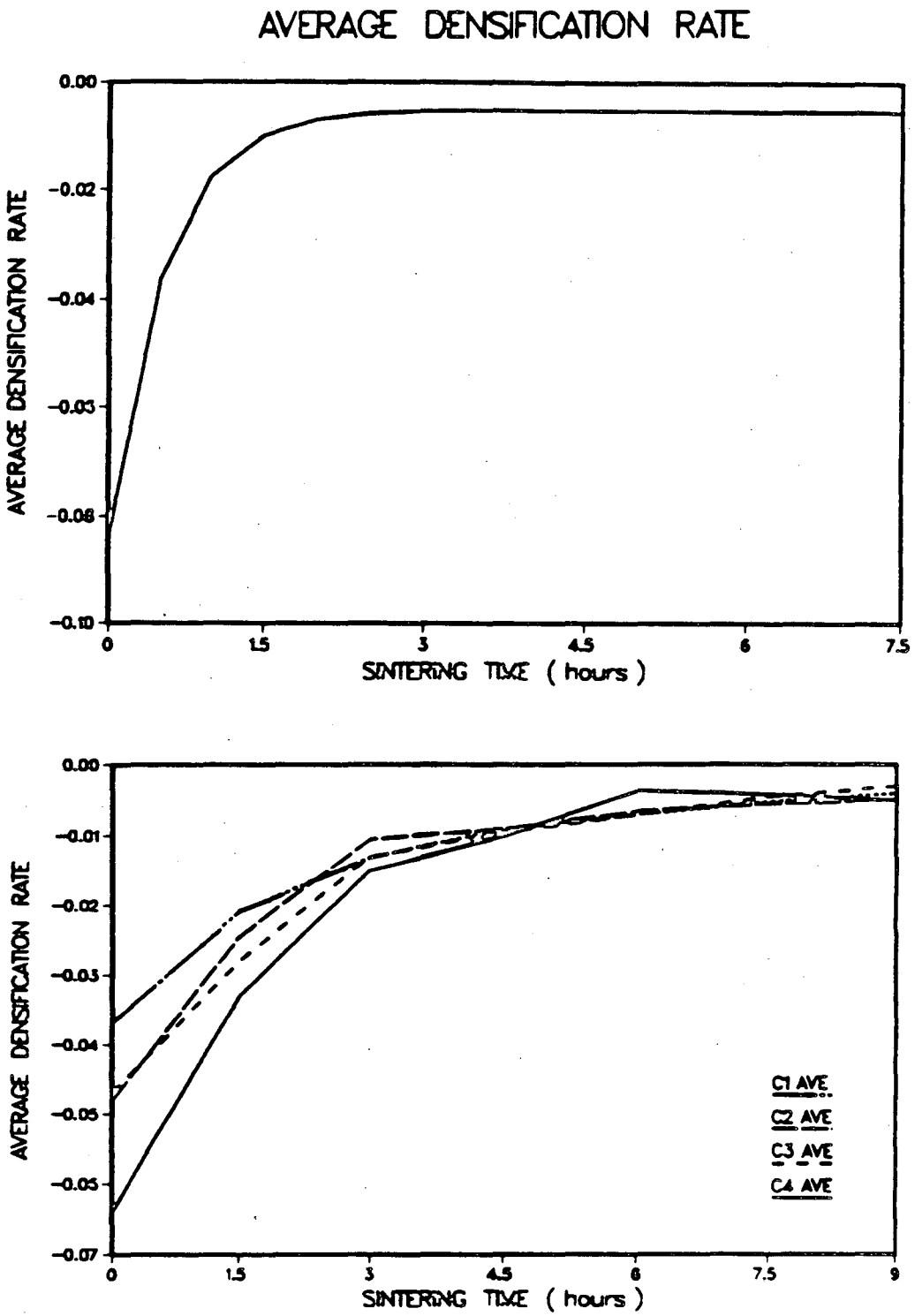

XBL 8412-5350

Figure 4.6 The average densification rates for all five areas. Run G is shown in the upper plot and the four areas from run C are shown in the lower plot.

4.1.2 Average Sphere Coordination Number and Distribution

The coordination number of a particle is the number of neighboring particles with which it forms sintering necks. This number will change during the sintering process as new necks are formed and old ones are broken. The coordination number is always less than or equal to the number of sides in the Voronoi cell since a nearby particle can be close enough to form a Voronoi cell edge without making contact with central particle. This can be seen in figure 2.7 for the central particle where the coordination number is 4 but there are 6 edges on the Voronoi cell.

It is possible to make regular, space filling arrangements of spheres in two dimensions that have coordination numbers ranging from three to six, these are illustrated in figure 4.7. The arrangement with a coordination number of three is not a close packing as an additional sphere may be inserted in the center of each of the hexagonal rings to convert it to the hexagonal close packing. The square close packing has the lowest coordination that results in a regular arrangement of spheres in two dimensions that is locally stable against collapse into an array of hogher coordination. In a random array the coordination number can also take on values of zero for an isolated sphere, and one and two, these low coordination arrangements can be thought of as analogous to the broken atomic bonds in an amorphous solid and are one of the primary differences between a regular and a random array.

In the five arrays studied here the initial coordination ranged from 3.44 to 4.08 and the final coordination ranged from 3.54 to 3.99 as graphed in figure 4.8. During sintering contacts between particles may form, be broken, or remain unchanged. A new contact is observed to form when two particles make contact

Regular Arrays of Spheres in 2 - Dimensions

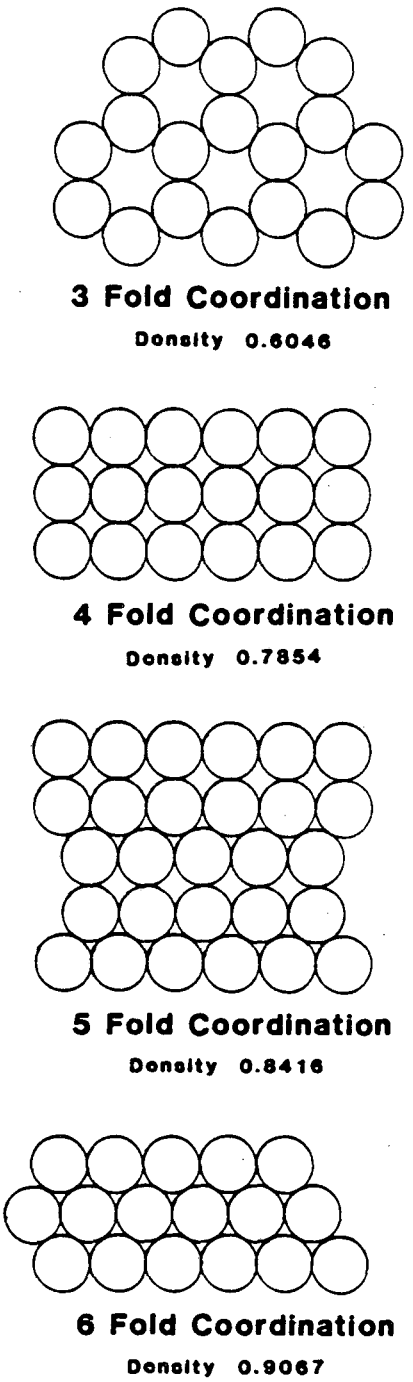

Figure 4.7 The four regular arrangements of spheres in two dimensions.

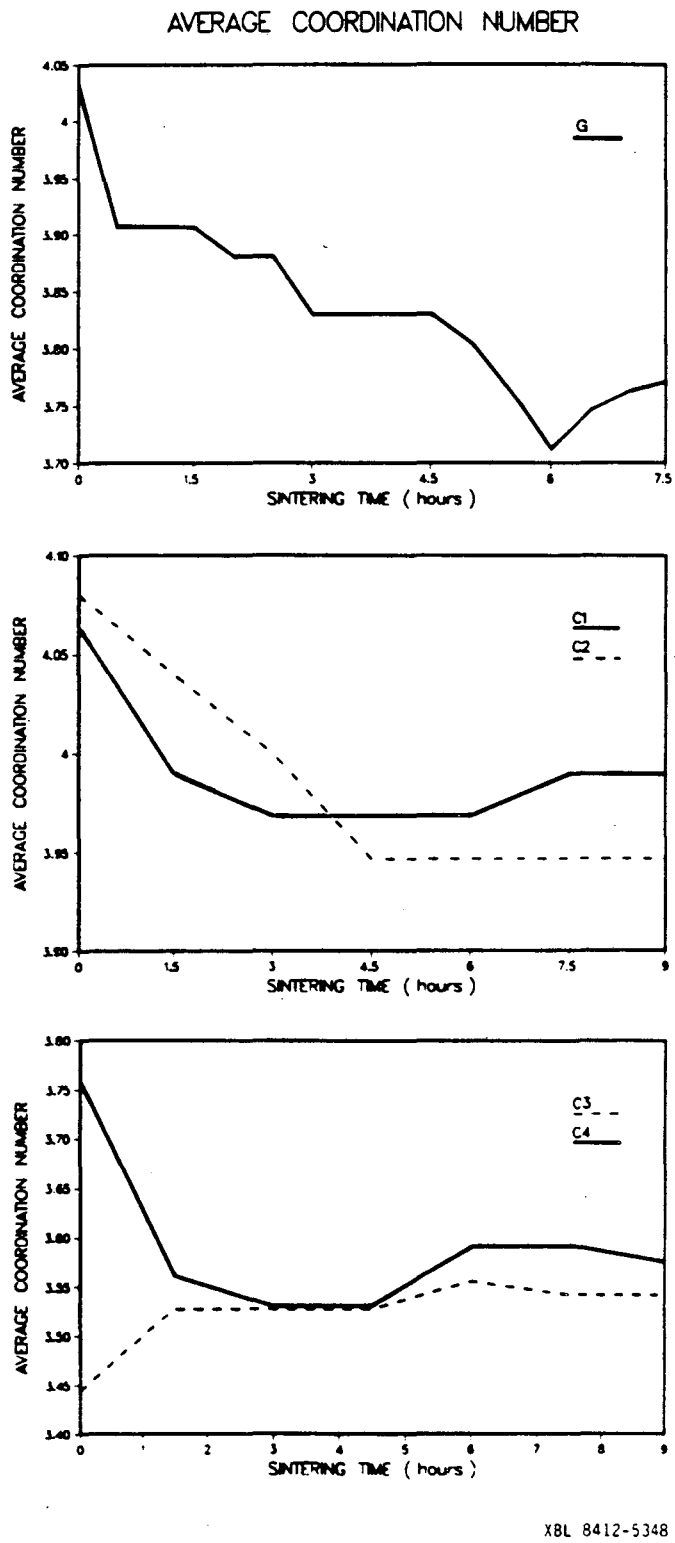

Figure 4.8 The average coordination number as a function of time for the five areas studied here. The top graph is for run G, the middle one for areas C1 and C2, and the lower one for areas C3 and C4.

for a long enough period of time to allow a neck to form between them and be seen on a micrograph. A contact may be broken when a large enough tensile stress is applied to the neck to make it creep and eventually rupture. The continuing contacts from the previous micrograph can exhibit either neck growth or neck shrinkage dependent upon both the operating material transport mechanisms and the stress condition of the neck. This relationship is plotted in normalized units for grain boundary diffusion for a variety of neck radii in figure 4.16. In this study the highly coordinated arrays showed more contact rupture than formation. This is due to the formation of very highly coordinated domains that can tear the more loosely packed areas between them apart. The arrays with low coordination exhibited the opposite trend and formed new contacts because the very highly coordinated domains necessary to break bonds did not form. These effects are felt to be direct a result of the relative inhomogeneity of the arrays studied here.

The distribution of the coordination numbers among the allowable values of zero to six is spread in a fairly predictable manner with the majority of the particles having three to five nearest neighbors. The distribution for run G is plotted in figure 4.9 and for run C in figure 4.10. There is a slight trend for the distribution to become peaked at four contacts per particle during the very early stages of sintering but this is highly dependent upon the details of the particle arrangement. During the later stages all of the distributions tend to broaden such that the number of particles with three or five contacts increases at the expense of those with four contacts per particle. This occurs because four fold coordination is a transition between loose and tight packings. In the later stages of this sintering experiment the more tightly packed domains are shrink-

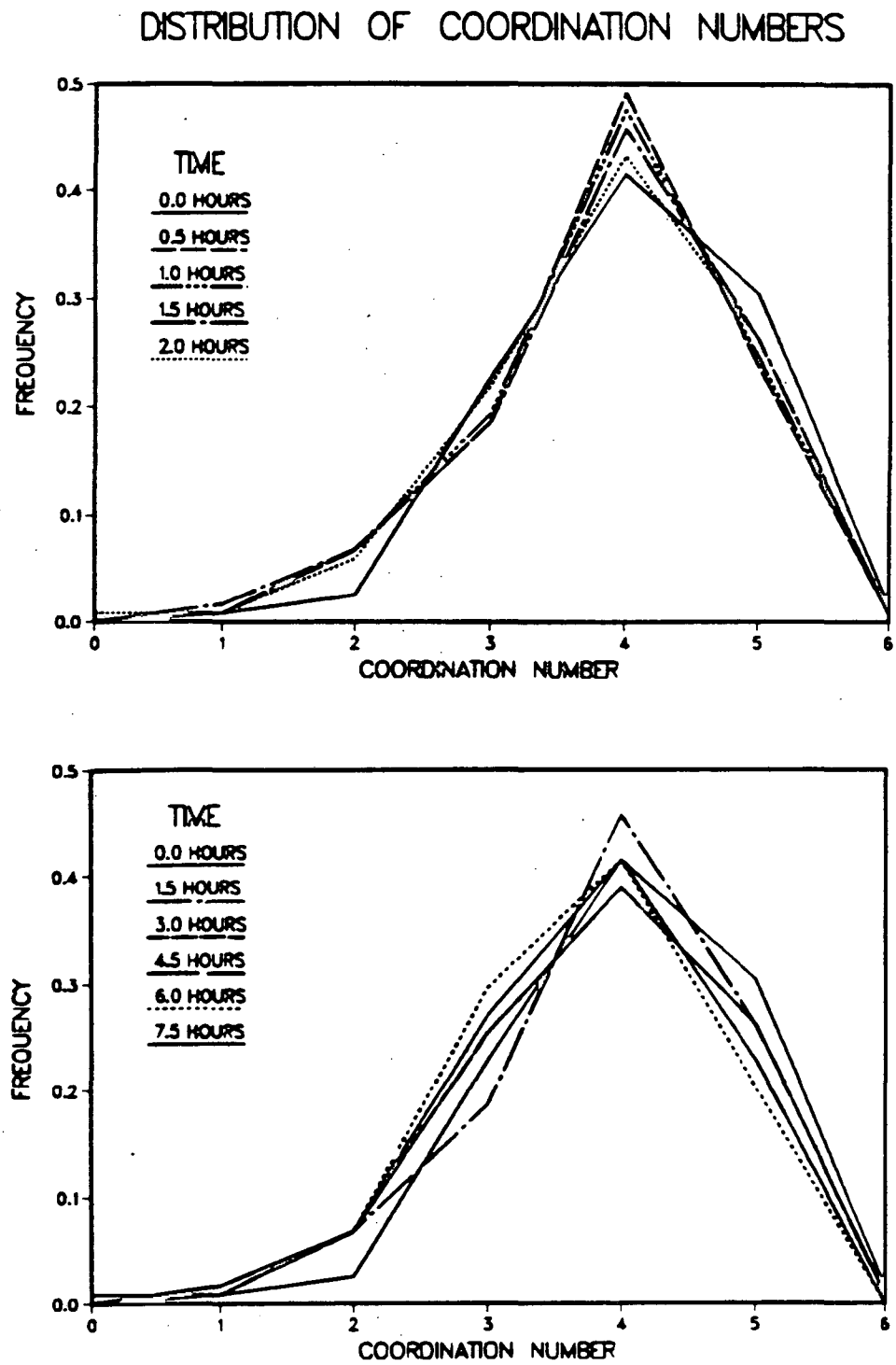

XBL 8412-5347

Figure 4.9 The distribution of the coordination numbers for run G. The upper graph shows the five earliest times and the lower graph shows every third time for the entire 7.5 hour experimental run.

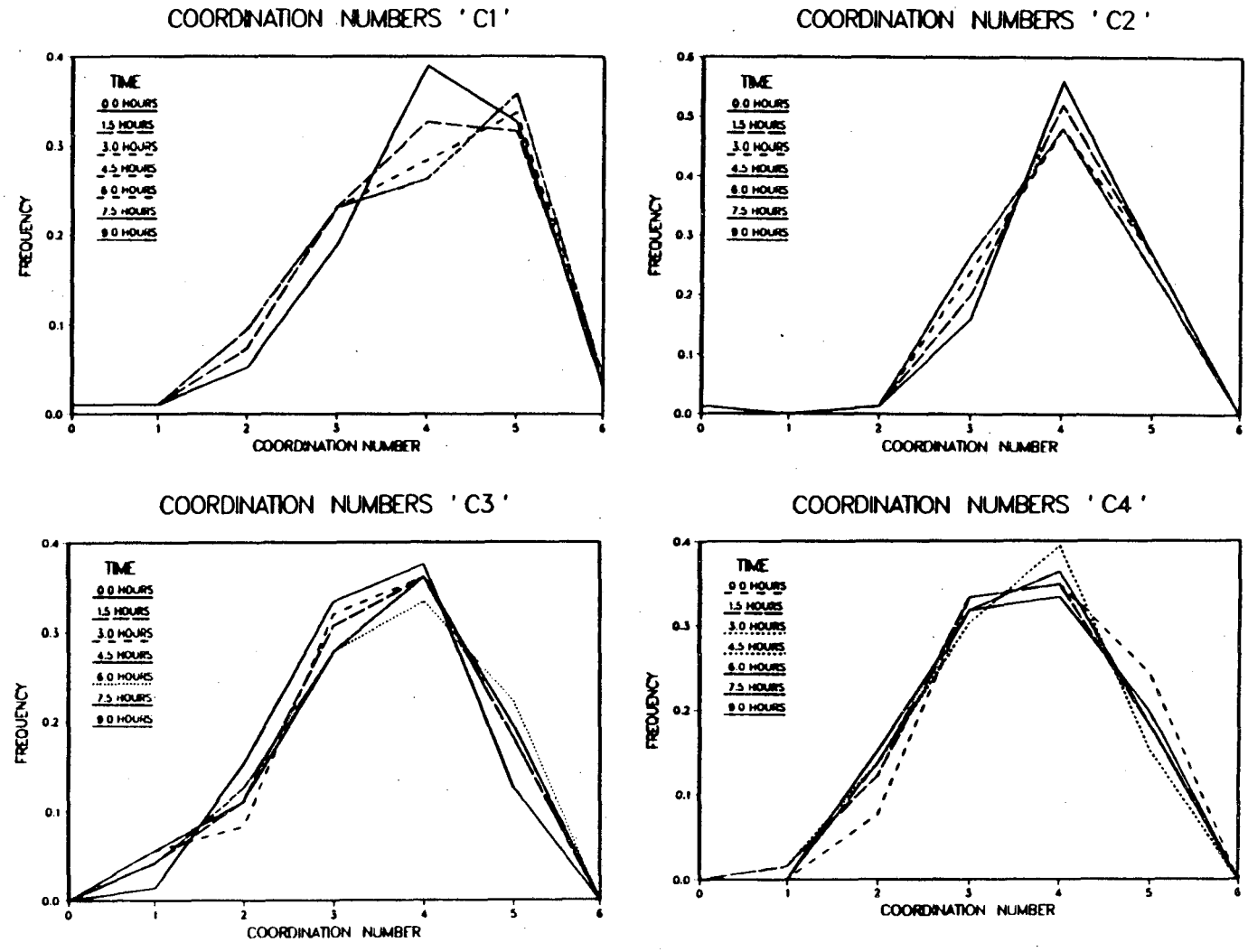

XBL 8412-5377

Figure 4.10 The distribution of the coordination numbers for run C.

ing homogeneously and a fifth contact can form. The loosely packed areas are often subjected to a tensile stress and a weak sintering neck can be torn apart.

The distribution of coordination numbers varies from the sharp peak in area C2 to the very broad distributions in C3 and C4. The width of the distribution is an measure of how uniformly packed the particles are in that array, since a sharp peak in the distribution is a result of a lack of both very densely and very loosely packed regions. The particles surrounding a large pore will have a lower coordination number because there are no particles to act as neighbors in the direction of the pore as shown schematically in figure 4.11. The sharp peak in C2 is a consequence of the very uniform packing of the particles in this array. The very broad distributions of C3 and C4 arise out of the great differences in packing density associated with the open network type of arrangement observed in these areas. Area C1 is still moderately spread but it is skewed heavily towards high coordination numbers, this results from the relatively dense packing in most of the array with the large riplike void along the top edge of the sample. The distribution for run G is somewhat peaked but not nearly as much as C2, this run was observed to have a fairly homogeneous packing with no large voids.

The average coordination number and the distribution of the coordination number can give some insight into the potential sintering behavior of particulate arrays. The average value is observed to approach a value somewhat less than four, the coordination of a regular square packing, regardless of its initial value. This results from the breaking of bridges between areas of high density in the highly coordinated arrays, and the formation of new contacts in rapidly densifying areas in arrays with a low initial coordination. The distribution of

Lower Coordination Around a Large Pore

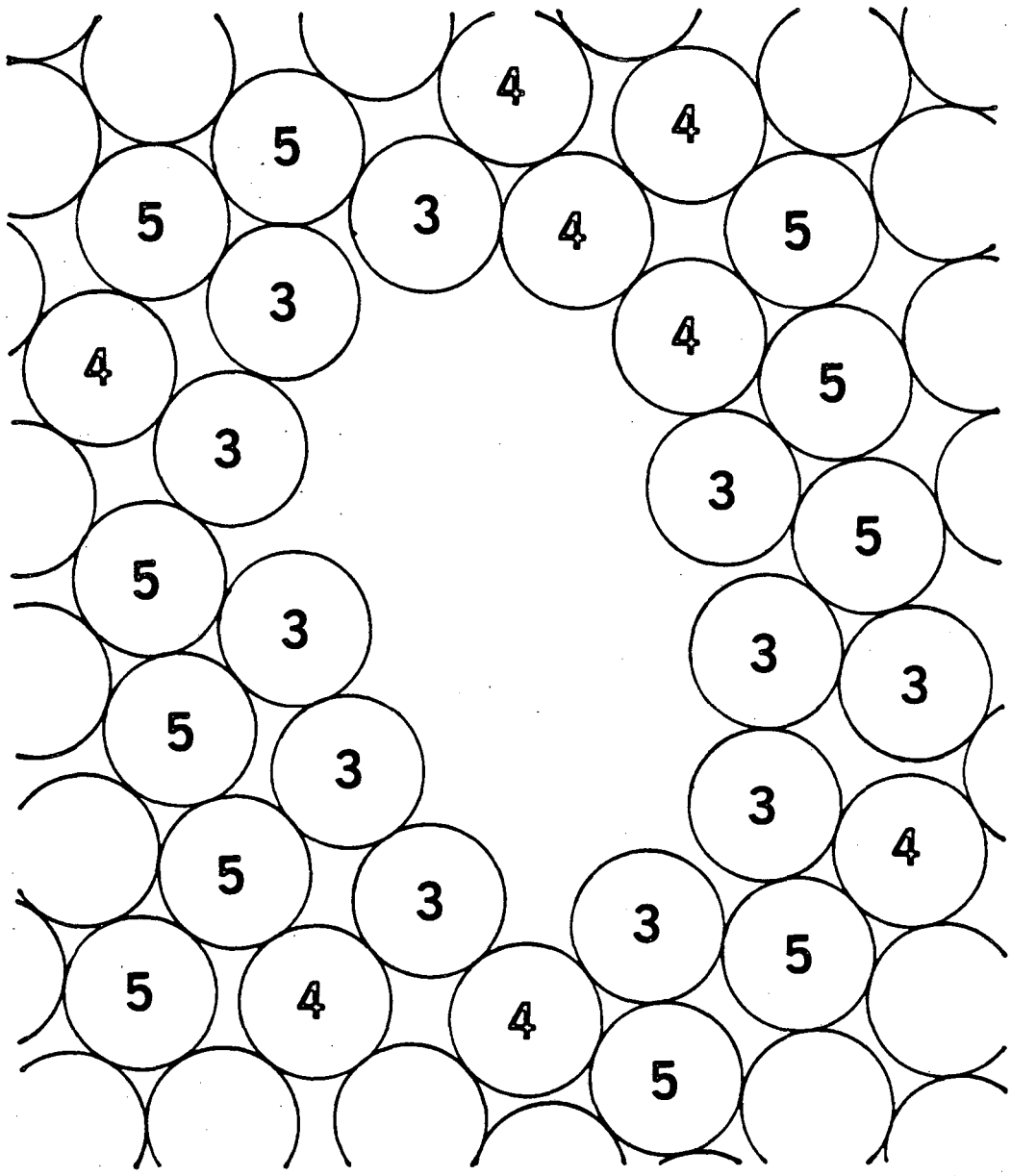

XBL 8412-5346

Figure 4.11 Schematic drawing showing the lower coordination around a large pore. The coordination number for each sphere is shown within the circle that is its projected image in two dimensions.

the coordination numbers is seen to broaden in various amounts as a function of the sintering time for all types of arrays. This is a consequence of the stretching, straightening, and sometimes breakage of the bridges connecting the high density areas. This results in a few strong bridges of very low coordination connecting high density, high coordination islands as the broken bridge ends are absorbed into these islands.

4.2 Local Density and Densification Rate

The local density used in this study was defined as the projected area of an average spherical particle divided by the area of the particle's Voronoi cell. This definition of the local density takes the sphere size, the local geometry, and the interparticle shrinkage into account. When the local density for a particle is plotted versus the sintering time the resulting curve is somewhat irregular due to the errors of up to 2 % in the measurement of the sphere location. This irregularity of the local density data was acceptable, but it caused the derivative with respect to time, the local densification rate, to be very erratic. To alleviate this problem the local density versus time was smoothed with a least squares algorithm that employed four adjustable parameters. The densification rate was then taken as the derivative of this function. The fitted curve varied less than 1.2 % from the actual data points in all cases. This smoothed local density and local densification data were used to produce the various plots this section and the maps in section 5.

Due to variations in the particle radius it is possible to have local densities that are greater than 1.0. A sphere in a hexagonal close packing with a radius smaller than 96 % of the average will have an initial local density greater than

1.0. The local density will then increase further with center to center approach. This type of variation in the particle size is not uncommon with particles of less than 50 micrometers diameter. The spheres used in this study had a mean diameter of 41 micrometers and over 95 percent of them were between 36 and 47 micrometers in diameter as shown in figure 3.1. This variation in the sphere size can make the interpretation of the results a little more difficult but it makes the behavior of the model experiment closer to that of a real particle compact.

In random arrays of the type studied here there are fluctuations in the packing density from point to point in the array. These fluctuations are seen in the width of the distribution of the local densities, this was measured as the standard deviation of the local densities. The variability of the local densities ranges from 5.7 to 11.5 percent of the average local density and increases with increasing sintering time as graphed in figure 4.12. Run G is initially more homogeneous than any of the areas in Run C as seen in by comparing the initial values of the standard deviation, 0.057 versus 0.074 to 0.084. This higher degree of homogeneity continues at all sintering times with a maximum variability of 0.097 for run G and a range of 0.099 to 0.115 for run C. The distributions of the local densities give good insight into how and why the variability of the local densities varies between areas and times, and how this will effect the final homogeneity of the array.

4.2.1 Local Densities

The initial distribution of the local densities for Run G is approximated by a slightly skewed normal distribution as plotted in figure 4.13. Both the spread

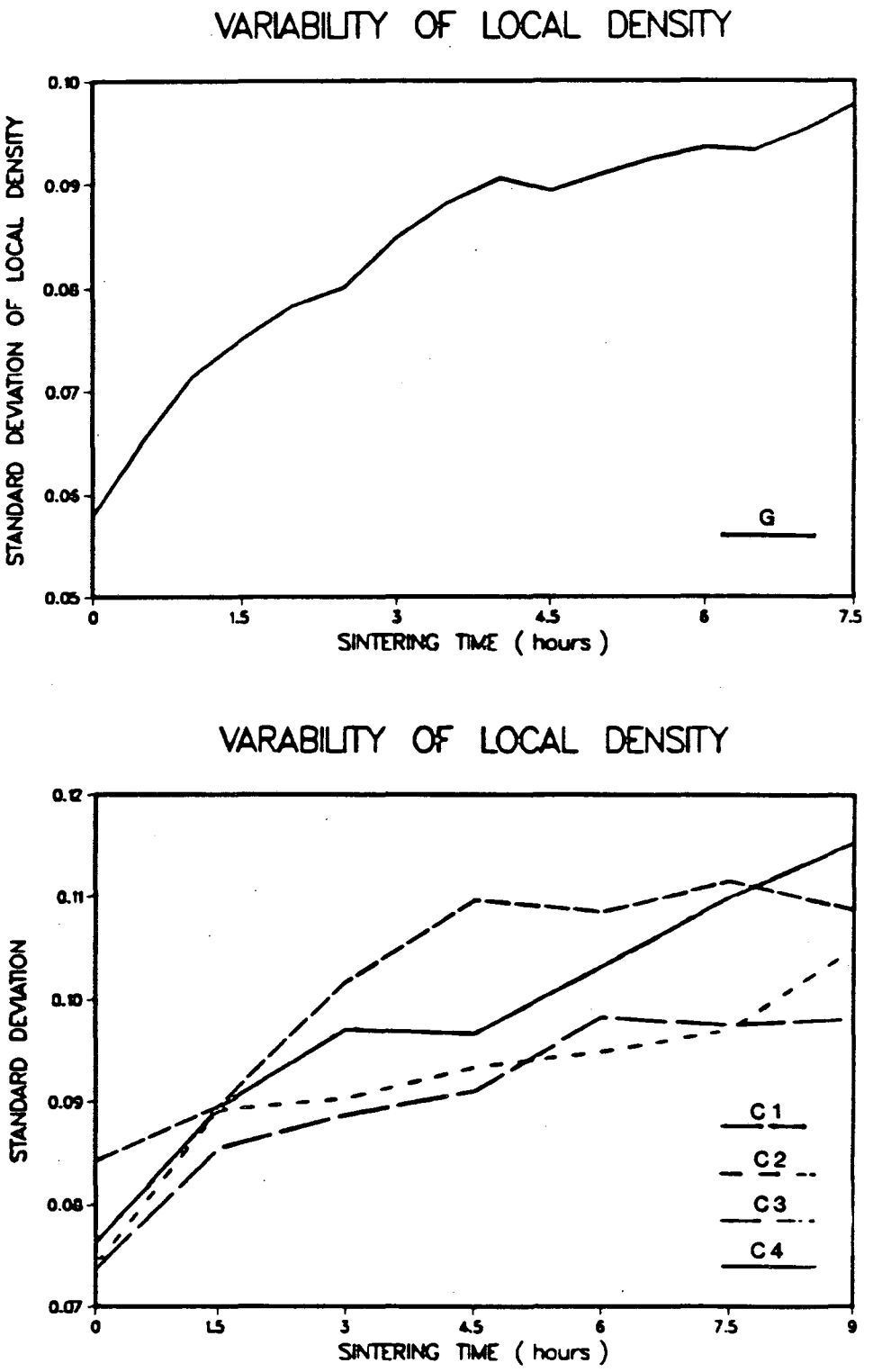

XBL 8412-5345

Figure 4.12 Variability of the local density as measured by the standard deviation.

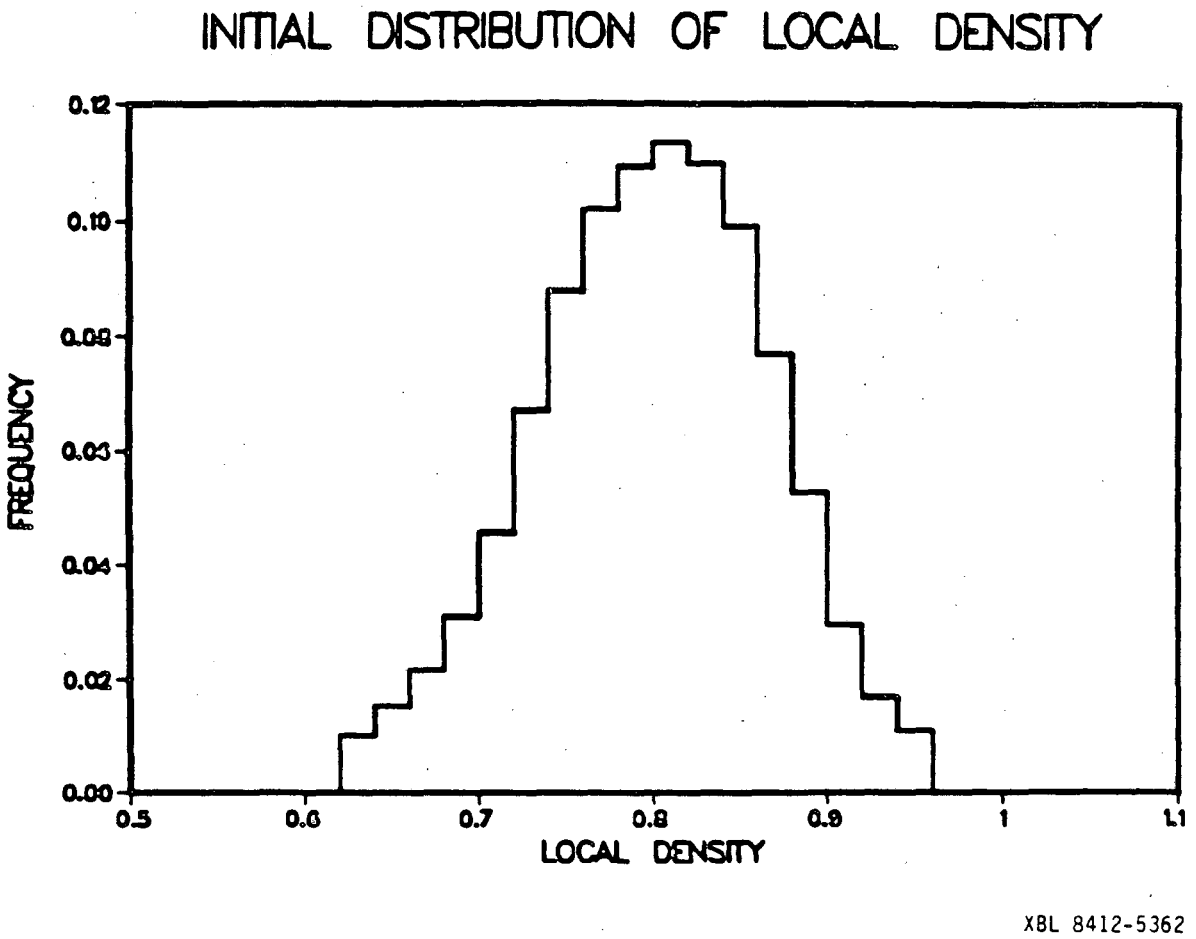

Figure 4.13 Initial distribution of the local density for run G.

and the skewness of the distribution increase with sintering time. This is illustrated well in figure 4.14 where the distribution of the local densities at times of 0, 1.5, and 7.5 hours are plotted. These times correspond to the initial, the end of the major fast rearrangement, and the final times used in this study. During the early stages of sintering the major change is the shift to higher densities with a the formation of a few low density cells. During the later stages of sintering the shift to higher densities is much slower but formation and expansion of large low density cells is accelerated.

This behavior is explained by the differences in the shrinkage behavior of areas of high and low density during the course of sintering. In the high density, high coordination areas the sintering necks are located a small distance apart compared to the low density, low coordination areas. As the sintering necks grow they can begin to impinge upon each other and decrease the radius of curvature of the neck as shown schematically in figure 4.15. The difference between the particle curvature and this curvature supplies the driving force for sintering. Any decreases in the neck curvature will dramatically slow the shrinkage rate as seen in the analysis of grain boundary diffusion for the two sphere model preformed earlier. A tensile force is generated in a sintering neck that is a function of the radius of curvature as seen from the calculation of the force required to halt center to center shrinkage graphed in figure 4.16. The result of this is that the shrinkage rate and tensile force generated in a sintering neck are lower than predicted by the neck diameter when neighboring necks impinge.

In high density regions the sintering necks impinge upon each other much sooner than in the low density areas. This causes the sintering rate to drop off in the high density area relative to the low density area. Such a low density

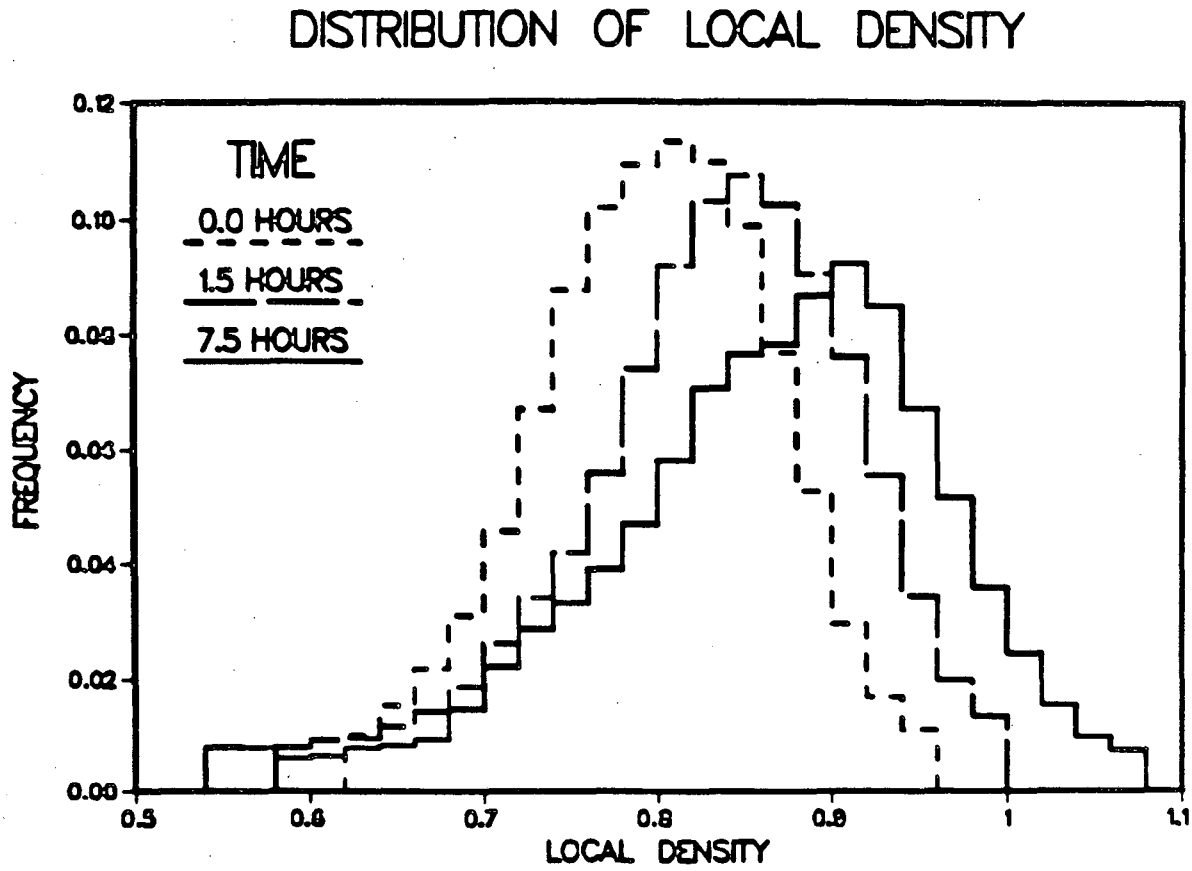

XBL 8412-5363

Figure 4.14 Distribution of the local density at 0, 1.5, and 7.5 hours showing how the distribution spreads and shifts to higher densities as sintering time increases.

Lower Curvature Due to Overlap of Sintering Necks

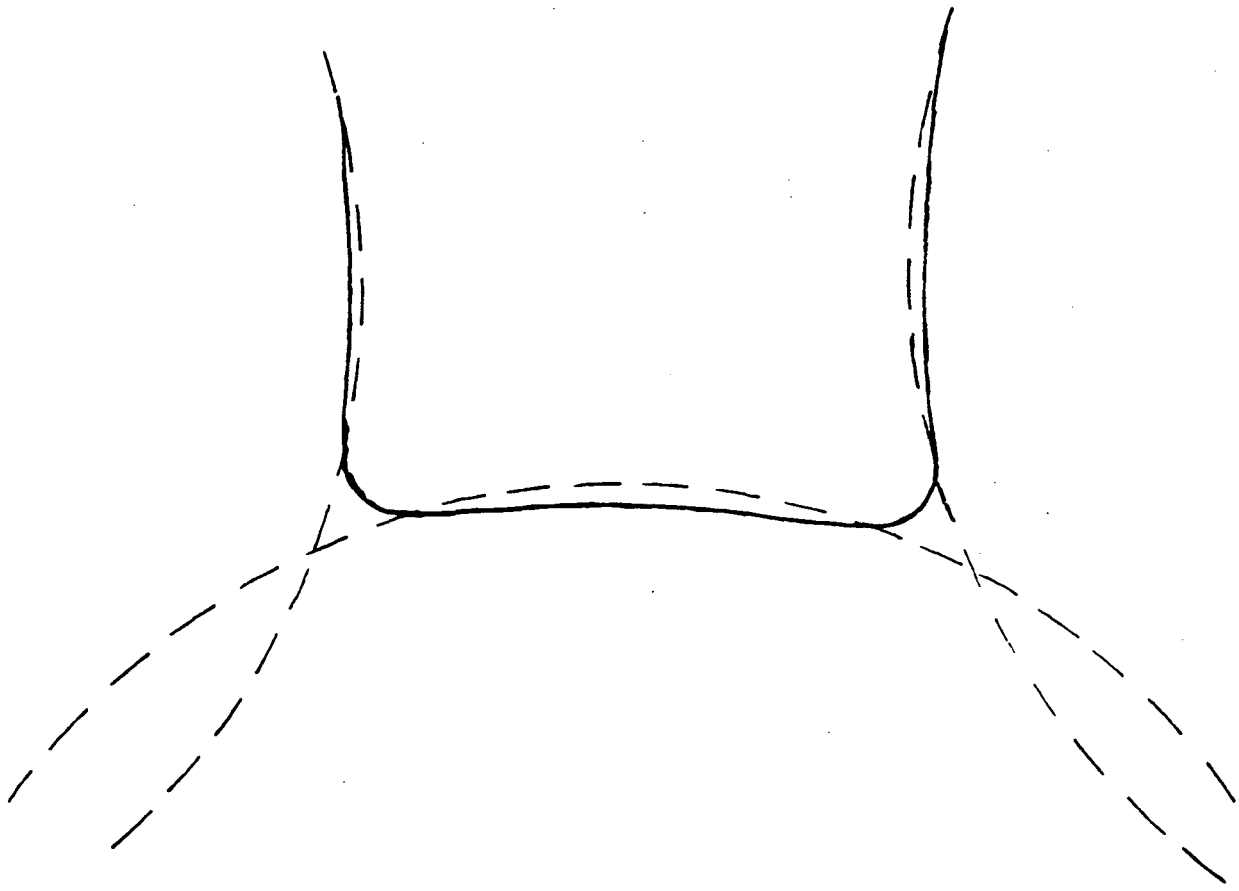

XBL 8410-4465

Figure 4.15 Schematic drawing of the lower curvature when necks impinge upon each other. The dashed line is the outline of the original spheres and the solid line is the geometry observed during sintering.

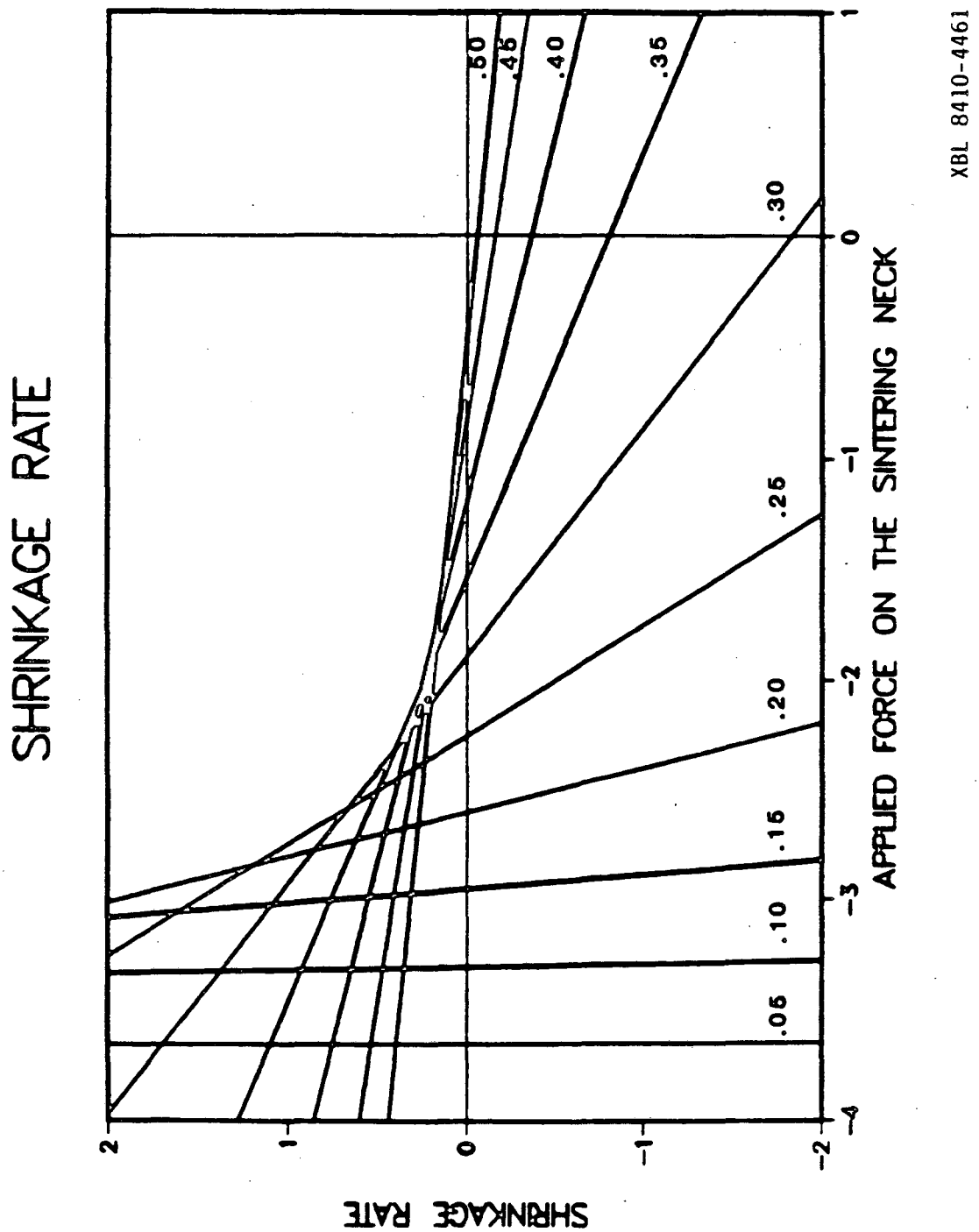

XBL 8410-4461

Figure 4.16 The shrinkage rate of the two sphere model as function of the applied force for various neck radii. Note that small radius necks require a much larger force to halt sintering than large radius necks.

area in high density matrix is shown schematically in figure 4.17. This results in a decrease in the shrinkage rate of the high density areas relative to that of the low density areas as plotted in figure 4.18. Because the sintering necks have not impinged upon each other in the low density areas the shrinkage rate continues at a faster rate than in the high density areas. However, when looking at the overall densification rate the effect of this faster shrinkage rate in the low density areas is more than offset by the slower rate in the high density areas. Due to the distribution of the stresses in a larger number of necks per particle in the high density areas it is not possible for the faster shrinkage of the low density areas to accelerate that of the high density areas.

A neck with a high energy grain boundary in it will sinter at a slower rate as shown by Hermann et al. [18] and thus develop a lower tensile force than its more favorably oriented neighbors. From discussion in the previous paragraph it is seen that the necks in the low density areas are being slowed from shrinking at their preferred rate and therefore a tensile force is developed in them. A neck with a high energy grain boundary located in a chain of necks in a low density area can then be the weak link in the chain. This stretching and subsequent breakage of a weak neck is illustrated in the micrograph of figure 4.19. It is felt that this neck stretching and subsequent breakage mechanism makes a major contribution to the rearrangement process. Such a process will have the greatest effect primarily during the intermediate stages of sintering when the necks have grown large enough for impingement in the high density areas but are still small enough so that substantial forces are generated in low density areas.

The four different areas of run C all exhibit variations of the possible types of behavior explained above. The initial distribution of the densities shown in

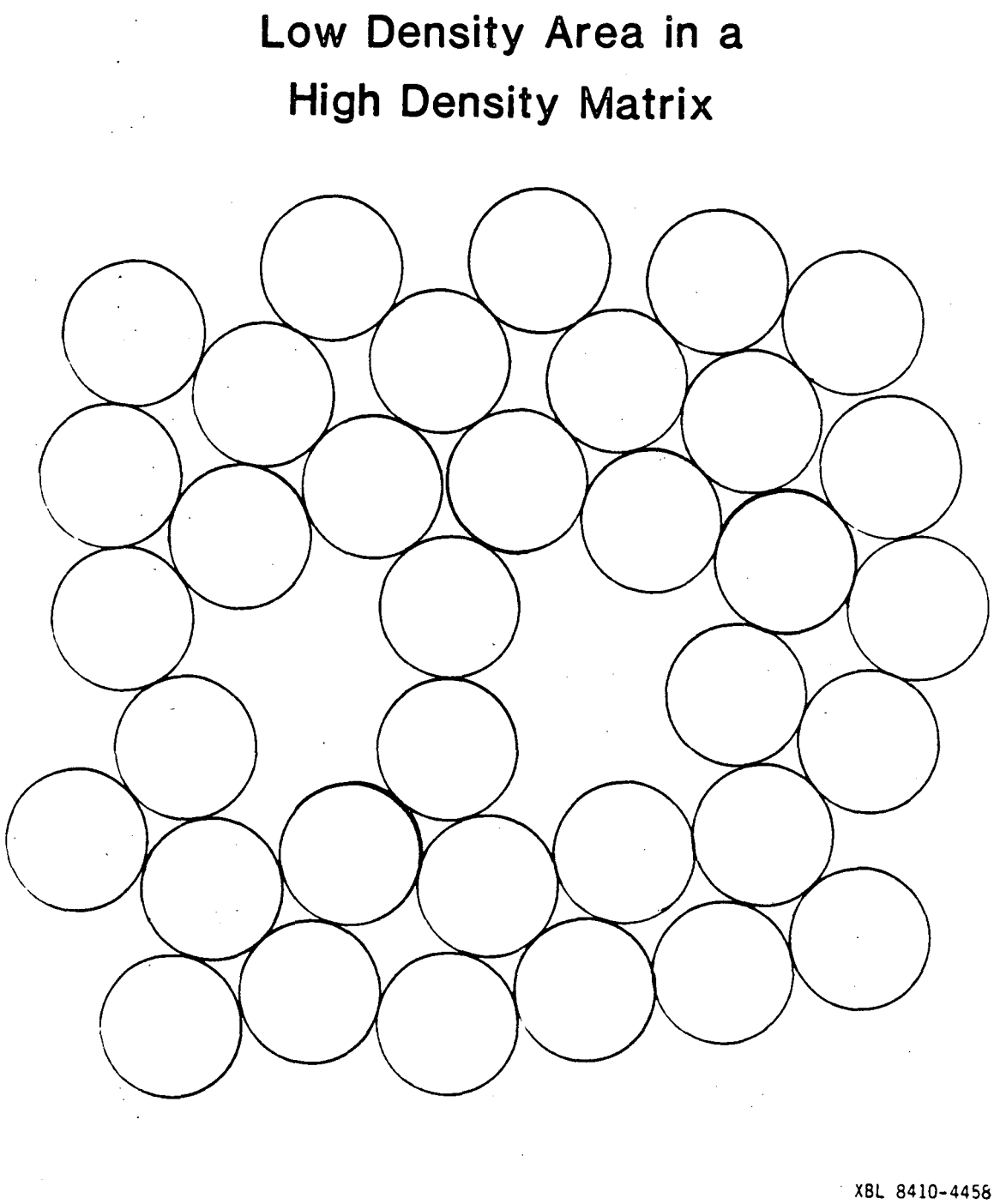

Figure 4.17 A low density area in a high density matrix. This results in the formation of a bridge between areas of high density.

Differential Shrinkage due to Different Surface Curvatures

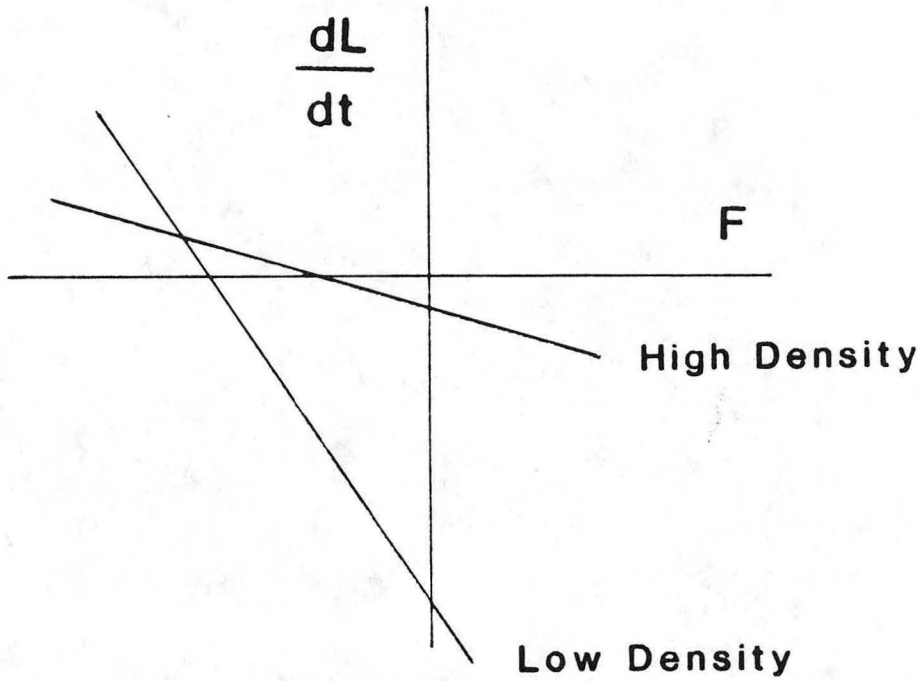

$$\frac{dL}{dt} = \frac{8D_b\delta_b\Omega}{kT}\left(\frac{K\gamma}{x^2} + \frac{2\gamma}{x^3} - \frac{F}{\pi x^4}\right)$$

XBL 8410-4462

Figure 4.18 The effect of different surface curvatures upon the shrinkage rate. The high density region has a lower curvature than the low density area due to the impingement of the sintering necks.

BRIDGES BETWEEN AREAS OF HIGH DENSITY

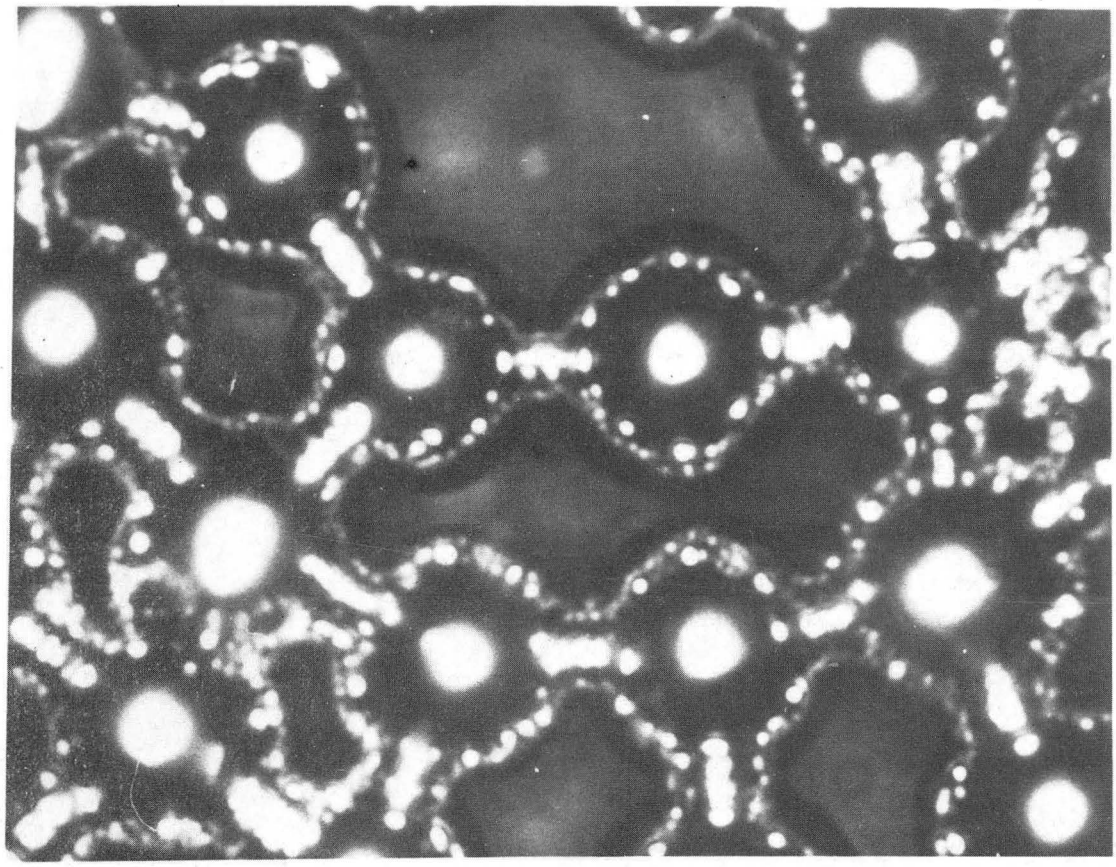

XBB 840-7819A

Figure 4.19 Micrograph of bridges between high density areas. Note that the sintering necks in the bridges are longer and thinner than those in the matrix indicating that they are being stretched.

figure 4.20 for array C1 shows a long low density tail indicating an area of low initial density which corresponds to the riplike void in the upper edge of this area as shown in figure 4.1. After sintering for nine hours the bulk of the cells have densified but a small fraction have remained stationary or de-densified. It appears that the cells with an initial density of less than 0.650 have expanded and caused the peak in the distribution at approximately 0.575. Area C2 was observed to be fairly uniformly dispersed from the micrograph in figure 4.2, this is confirmed by the initial distribution of the local densities shown in figure 4.21. In this case the distribution strongly shifts toward higher densities upon sintering with only a slight trend for the lower density cells to densify at a slower rate. The large amount of very uniform densification observed in this area is felt to be a result of the uniformly high initial particle distribution.

The distribution for area C3 is also initially very uniform as seen in figure 4.22, although at a lower density than C2. During the first half of the sintering the distribution shifts toward higher densities much as area C2 did. During the second half of the sintering the highest density cells, near a density of 1.000, no longer shrink. The cells in the density range 0.800 to 0.900, however do continue to shrink at the expense of the lower density cells. The low density cells then show some de-densification during the second half of the sintering. The late appearance of the de-densification in this area is a result of the proximity of the area to the edge of the sample and the uniform open network structure of this area as shown in figure 4.3. In areas that are relatively loose or located near the sample edge it takes longer for a strong enough network to be set up to break necks than in areas closer to the center of the sample. This results from the lack of constraint in the direction of the sample edge where no particles are found. In

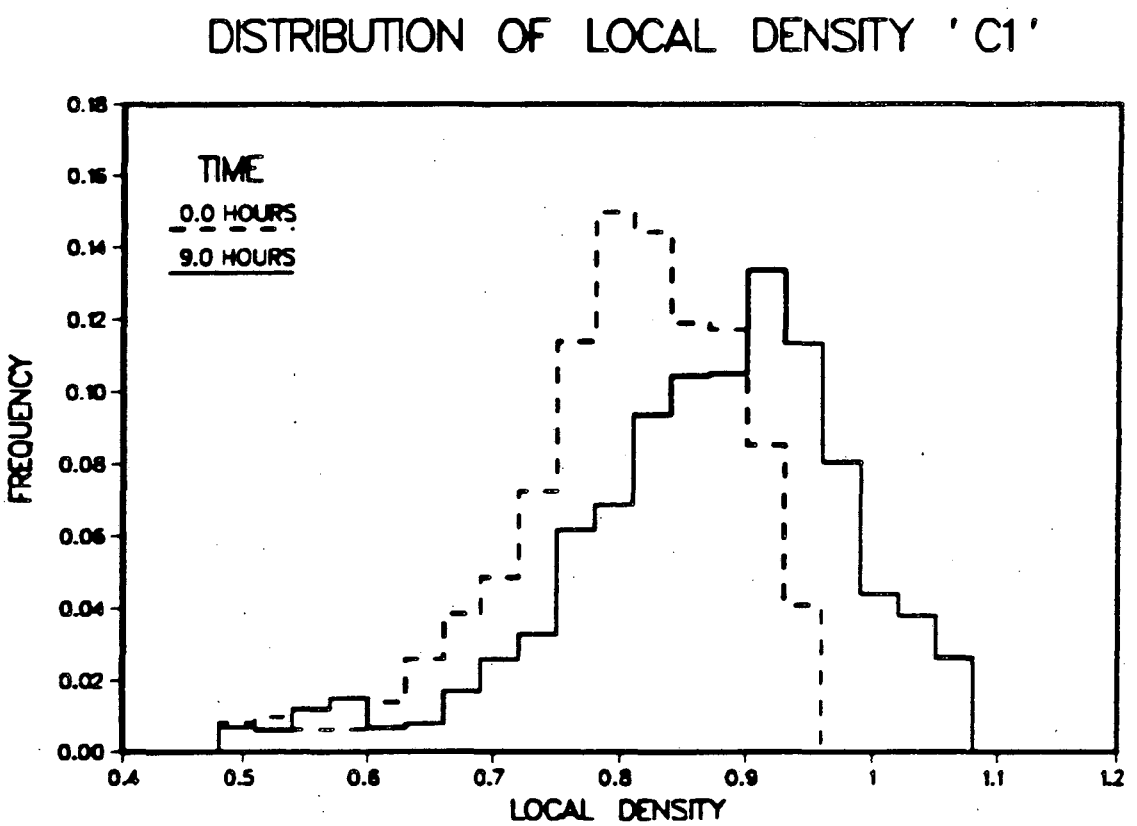

XBL 8412-5364

Figure 4.20 Distributions of the local densities for area C1.

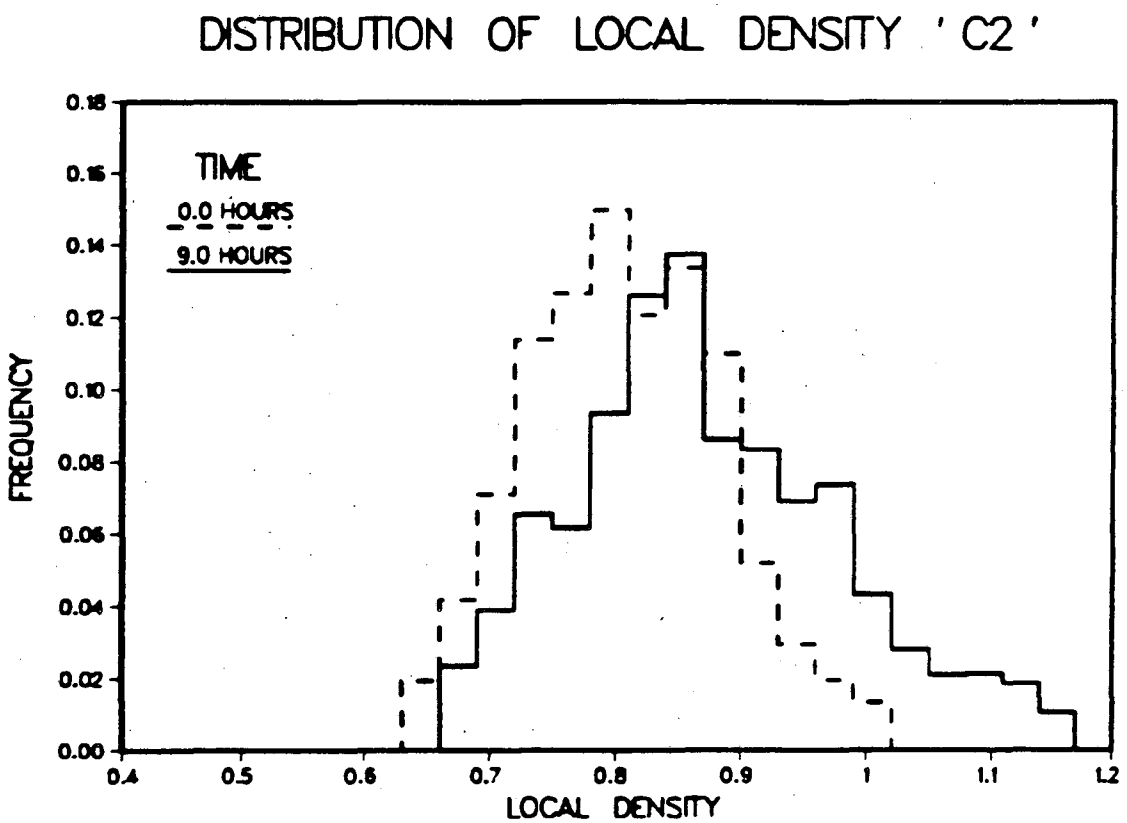

XBL 8412-5361

Figure 4.21 Distributions of the local densities for area C2.

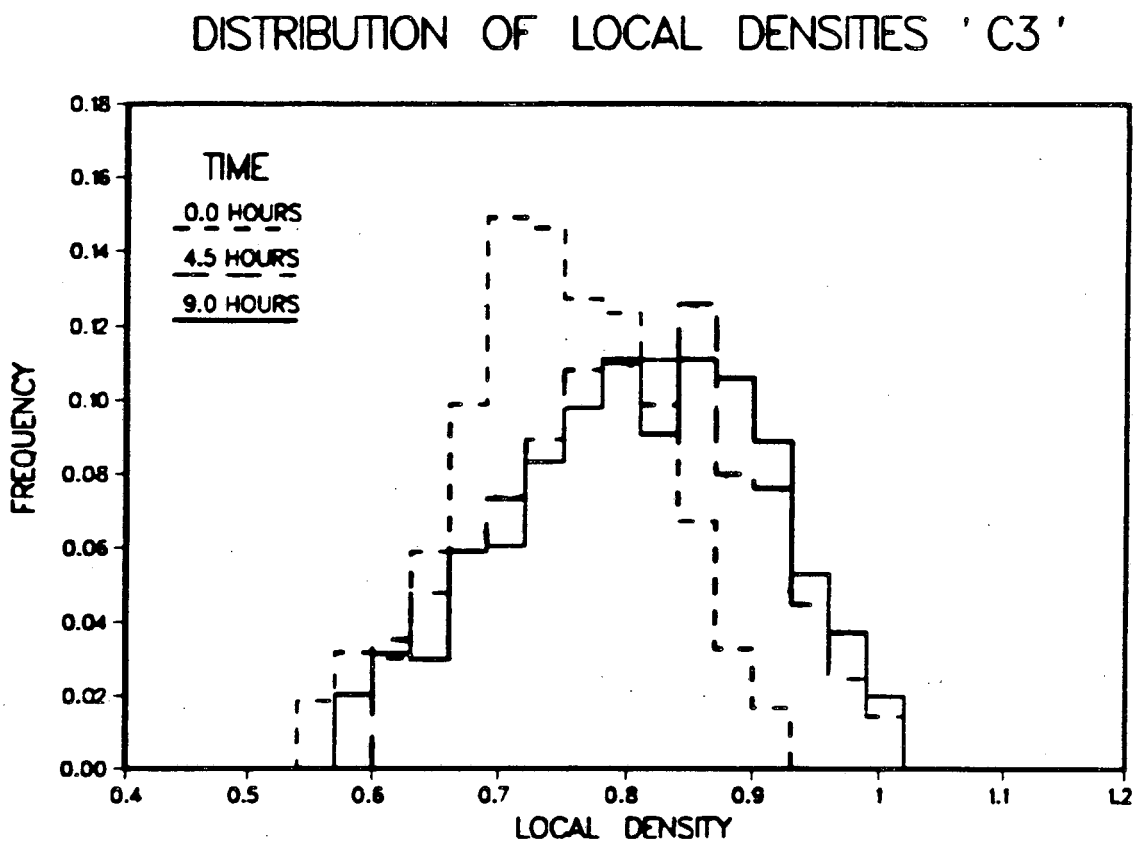

XBL 8412-5359

Figure 4.22 Distributions of the local densities for area C3.

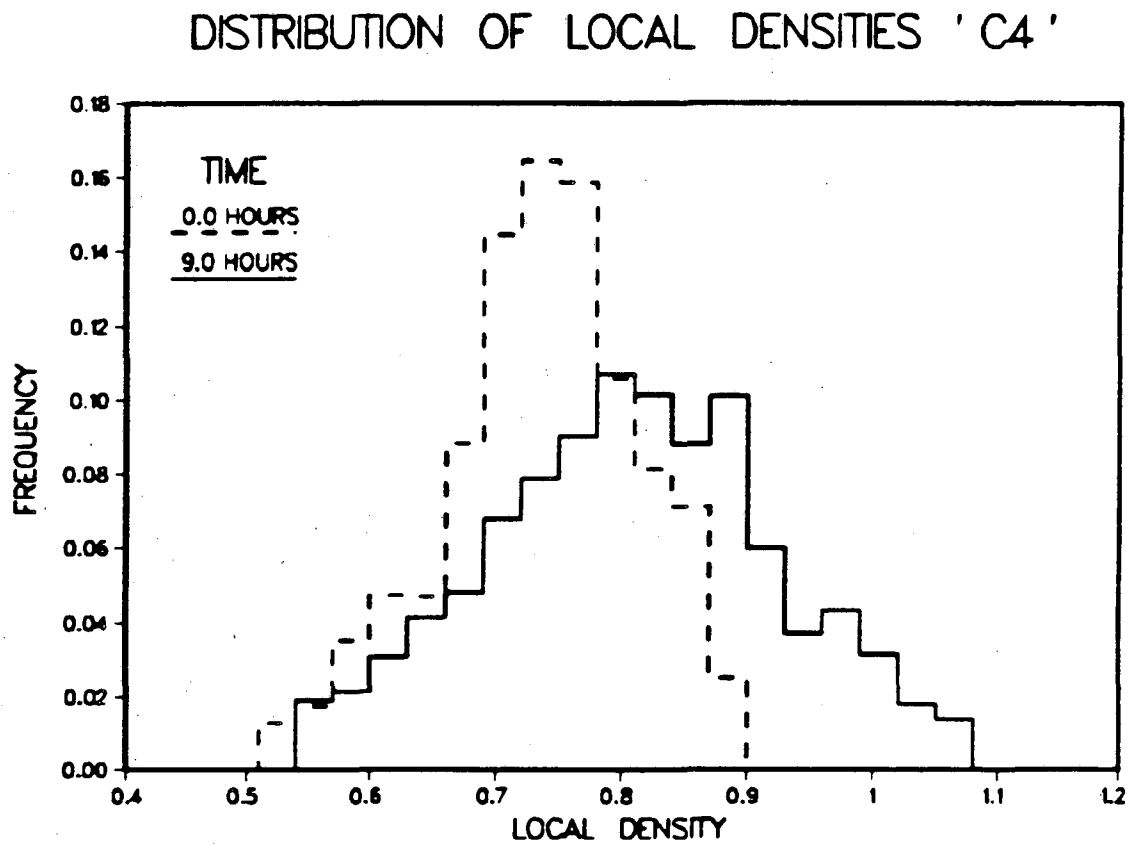

XBL 8412-5360

Figure 4.23 Distributions of the local densities for area C4.

area C4 the initial distribution is fairly uniform except for a pronounced low density tail as plotted in figure 4.23. Upon sintering the bulk of the cells shrink strongly but those in the low density tail show little or no densification.

From the two-dimensional arrays of spheres studied here it appears that a prediction of the local shrinkage behavior can be made based upon the local density of the particle. Particles that have a local density of less than approximately 0.650 seem to be unstable as far as whether they will densify or not. Particles with very low local densities, less than 0.550, de-densify in nearly all cases. Since the densification behavior of the Voronoi cell of a particle is a complex function of not just the local density this can not be taken as a quantitative law of densification. However, it is felt that this can give a better idea of the degree of initial homogeneity required to produce a homogeneous final sintered compact than using only parameters such as the particle coordination.

4.2.2 Local Densification Rate

The distributions of the densification rates behave in nearly the same manner for both runs and will be treated together. In the graphs presented here a negative rate means densification and a positive rate means de-densification or expansion of the Voronoi cell. The initial distribution shows most of the cells to be densifying with a small fraction of them de-densifying as shown in figures 4.24 and 4.25. For most of the areas the number of de-densifying cells drops off rapidly as the rate of de-densification increases. For run G some of the cells are seen to continue to de-densify rather strongly. This is a result of necks being stretched and broken in strings of initially slightly lower density cells located between high density areas.

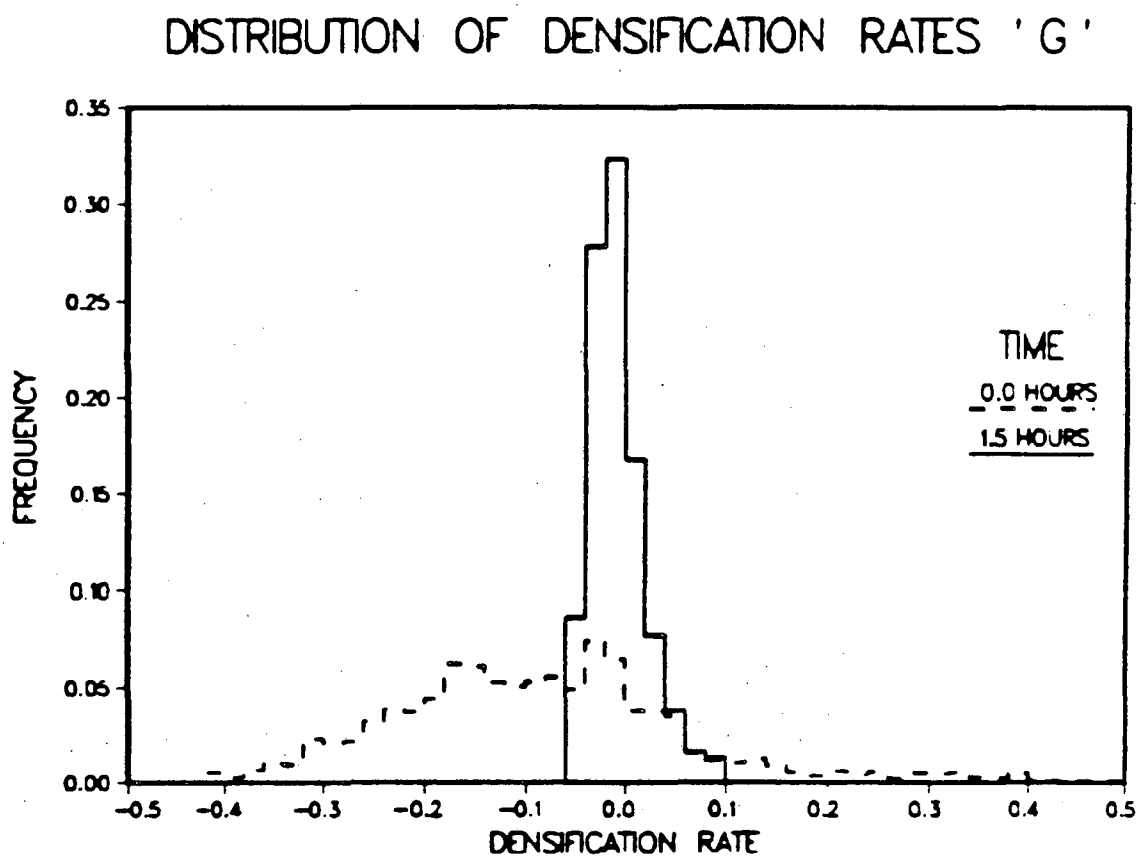

XBL 8410-4402

Figure 4.24 Distribution of the densification rates for run G. Note that the distribution is initially widely spread and narrows dramatically after only 1.5 hours.

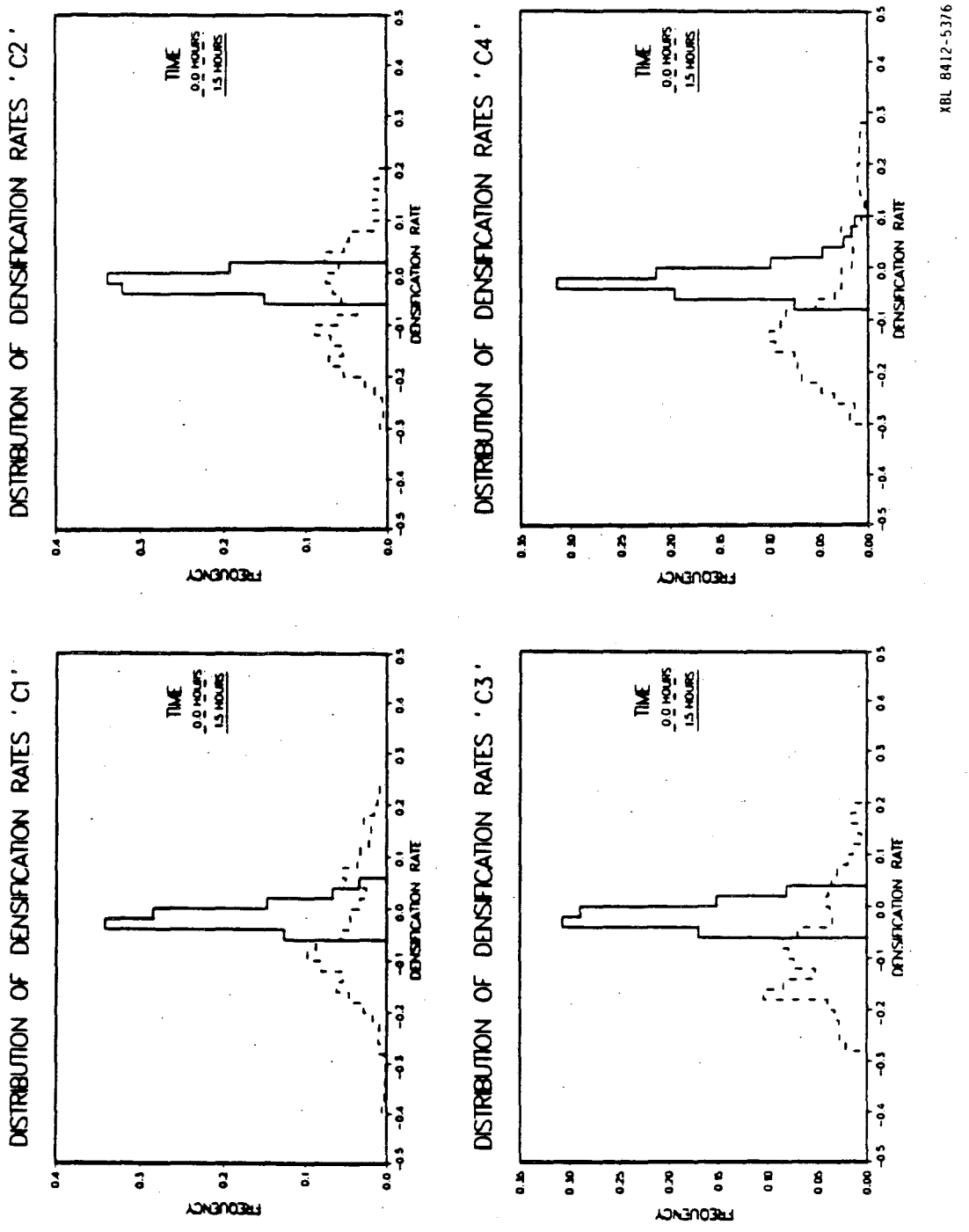

Figure 4.25 Distributions of the densification rates for all four areas of run C.

After sintering for just 1.5 hours the distributions of the densification rates have narrowed dramatically and the average rate has tended towards zero. As the sintering progresses the densification rate was observed to go from skewed in favor of densification to skewed slightly towards de-densification as shown in figure 4.26, however, the overall densification rate remained slightly negative meaning densification predominates. During the later stages of sintering a portion of the overall shrinkage is accommodated by the expansion of nearby cells. The result of this is that the dense areas continue to densify and that the lowest density areas are very slowly torn apart.

The general densification behavior of cells of different local density can be seen by plotting the average densification rate for a particular local density versus the local density. Figures 4.27 and 4.28 show that in general the dense cells tend to shrink or at least remain neutral at all times and that low density cells can exhibit both densifying and de-densifying behavior dependent upon the extent of sintering. Initially it can be seen that cells of all densities tend to densify with stronger densification occurring at lower densities. After the initial overall densification the low density cells tend to de-densify and the high density cells to densify. The formation of large sintering necks as the sintering progresses causes the average densification rate, whether positive or negative, to approach zero.

Both of these trends are illustrated particularly well in run G, figure 4.28, because of the larger number of time increments. For run G the crossover from densifying to non-densifying behavior occurs at a local density of approximately 0.700 in good agreement with the value of 0.650 found from the analysis of the distribution of the local densities. In some of the other areas this trend is not

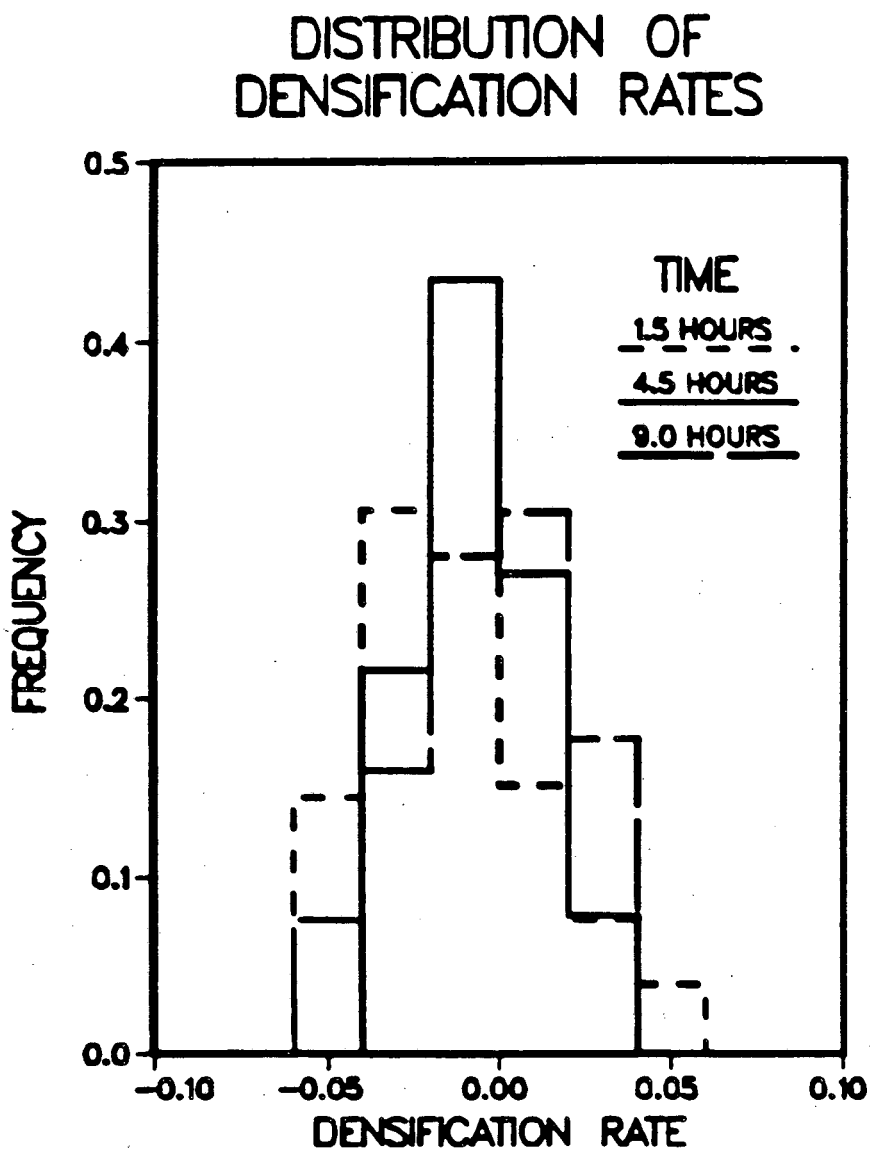

XBL 8412-5358

Figure 4.26 Distributions of the densification rates for 1.5, 4.5 and 9.0 hours for run G. This shows the shift from skewed towards densification to skewed towards de-densification.

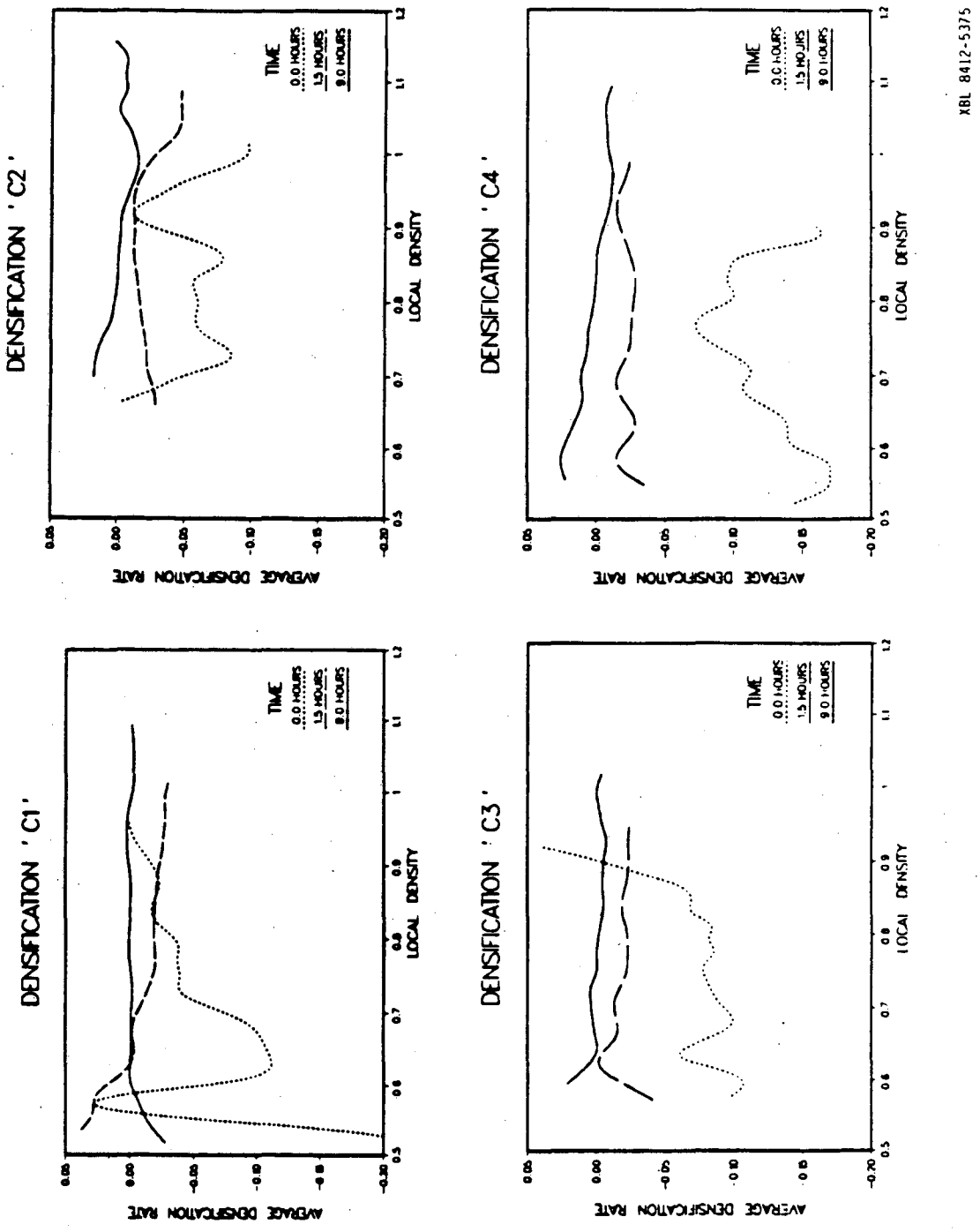

Figure 4.27 The densification rate versus the local density for all four areas of run C.

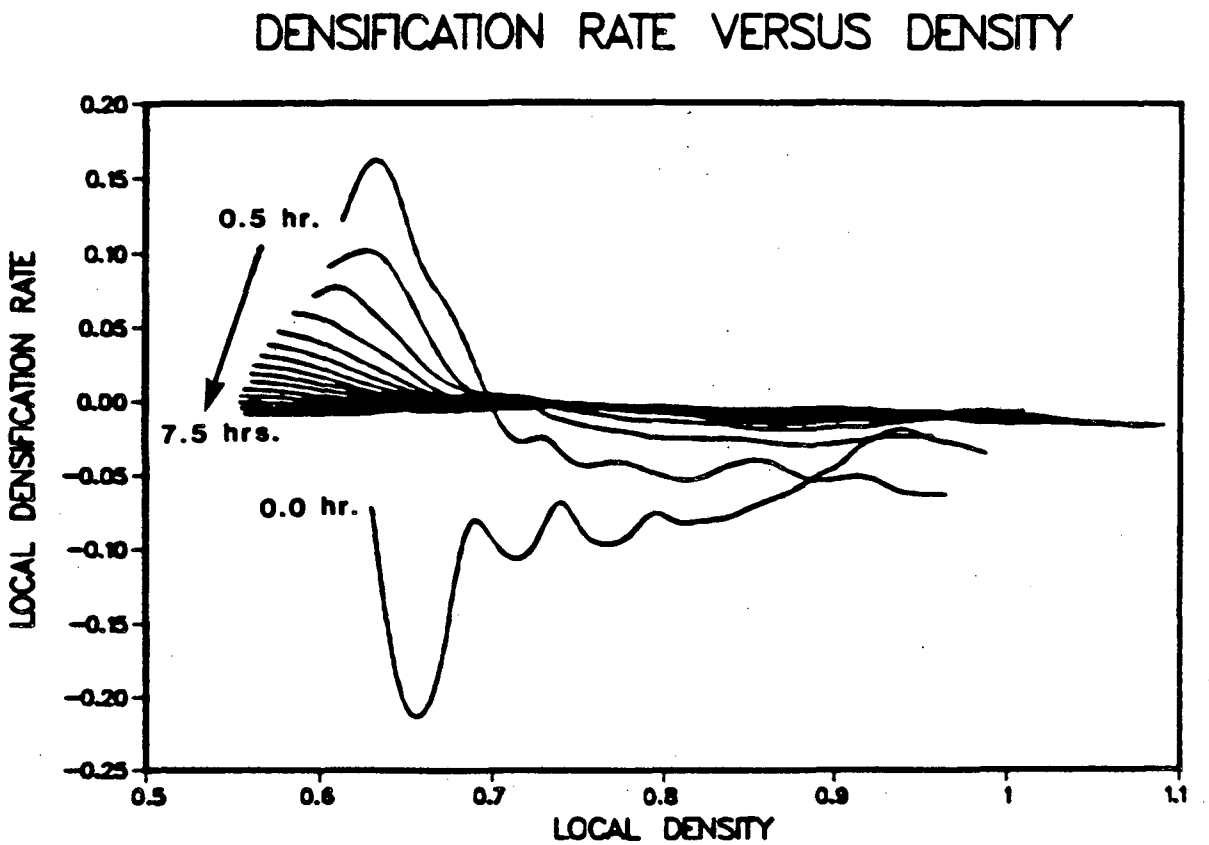

XBL 8412-5371

Figure 4.28 The local densification rate versus the local density for run G. This shows the rapid initial densification for all local densities and the cross over from de-densification to densification at a local density of about 0.7.

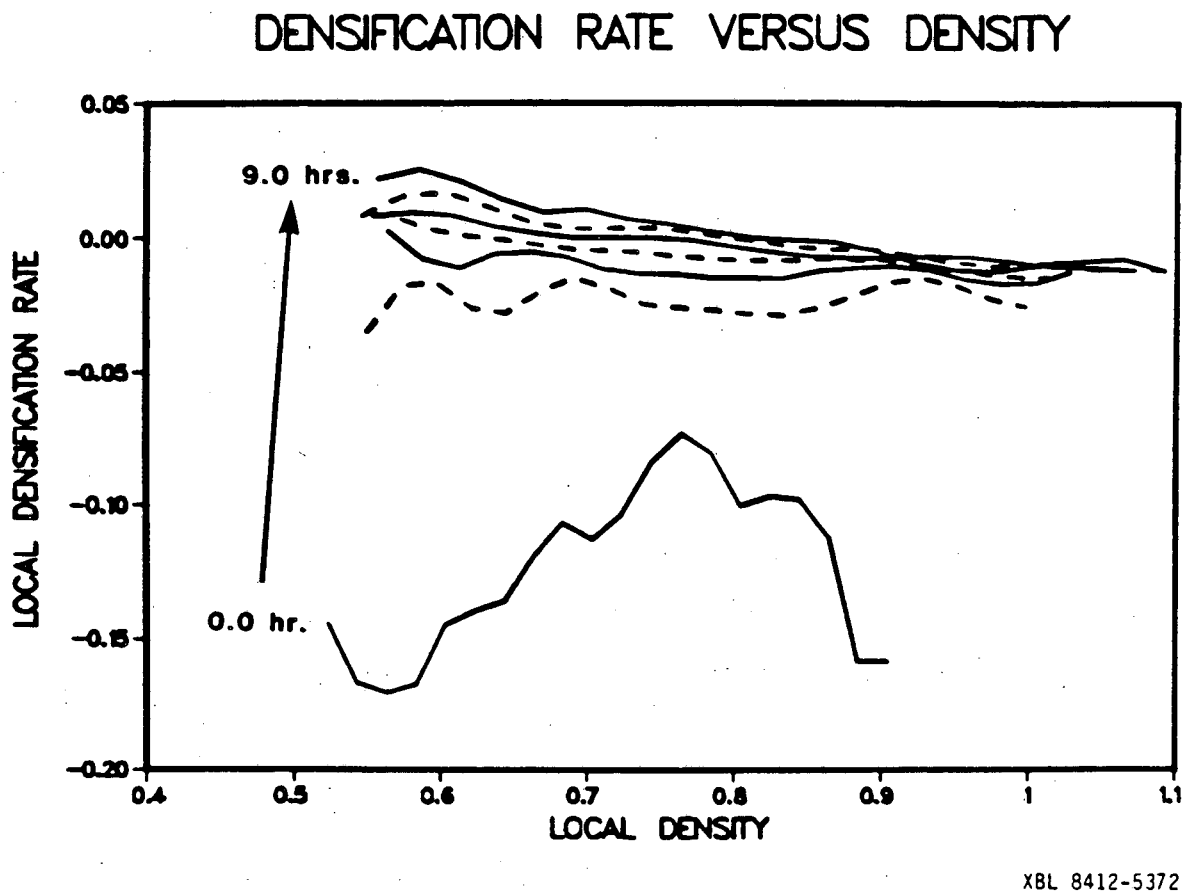

Figure 4.29 The local densification rate versus the local density in run C showing that higher density cells tend to densify faster than the lower density cells.

nearly as clear cut; however, the trend of high density cells densifying at a faster rate than the low density cells appears to hold in general as seen in figure 4.29.

As seen in the previous sections there is no absolutely clear cut method of predicting the densification behavior of a two dimensional array of spheres during the early stages of sintering based only upon the local density of the particle. There is a tendency for the low density cells to shrink at a slower rate or not at all when compared to the high density cells. The actual determination of which cells will shrink or expand is a complex function of both local and longer range parameters. The local parameters include the local density, the particle's coordination number, and the sizes and crystallographic orientation of each of the necks. The longer range parameters include the coordination and density of the surrounding area and the angular relation between particles. All of these parameters affect both the ability to form a network and the distribution of stresses in the network. These stresses can then stretch and break necks in areas of low local density. The determination of the densification behavior of individual configurations of particles is very difficult to predict based only upon statistical analysis. Prediction of the sintering behavior of particular configurations is probably best accomplished by an accurate computer simulation once we learn the details of particle interactions in random arrays.

4.3 Interparticle Distances

The interparticle distance used in this study is the distance between sphere centers of nearest neighbors. Nearest neighbors are spheres which are joined by a sintering neck. Initially this distance is just the sum of the two spheres radii

and will be evenly distributed about 2.0 as shown in figure 4.30 since the sphere radii have been normalized to 1.0. In order to more easily examine the shrinkage or elongation behavior of individual sintering necks the initial distance of each neck was normalized to a length of 1.0. This results in the initial distribution of the nearest neighbor distances being a delta function at 1.0, so the initial data are omitted from the graphs for clarity. Two examples of the distributions of distances are shown in figure 4.31.

For both experimental runs the very sharp peak in the distribution at 1.0 spreads and shifts to lower values as a function of the sintering time. Most of the necks are observed to shrink rapidly soon after sintering begins and to continue to shrink as the sintering progresses. A few of the necks are observed to lengthen soon after sintering commences, the number of these long necks then decreases gradually during sintering. This trend of most of the necks shrinking with a few elongating agrees well with a differential densification mechanism as proposed earlier.

As the sintering occurs, the nearest neighbor distance will either shrink for interpenetration of the spheres or lengthen if the sintering neck is being stretched. When the distance for a particular neck is plotted as a function of time two dramatically different types of behavior are observed. The majority of the necks tend to exhibit shrinkage at nearly all times, however, some of them elongate after various amounts of shrinkage. Because distribution of the stresses in the network varies as a function of time it is possible for individual necks to be stretched at nearly any point in the sintering process. Those necks that elongate during the early stages of sintering often exhibit a rapid shrinkage during the later stages of sintering as shown in figure 4.32. This rapid shrinkage

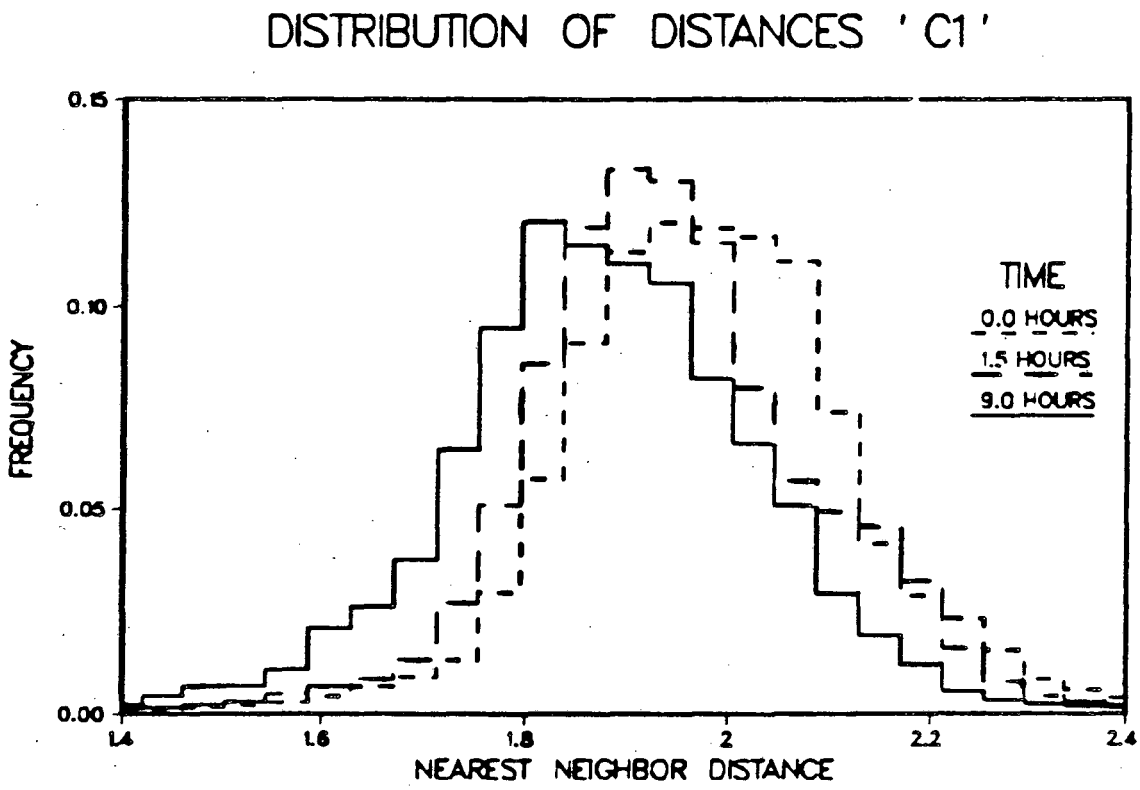

XBL 8412-5373

Figure 4.30 The distribution of the interparticle distances for area C1 showing the moderate spread in the values and the shift to shorter distances as sintering progresses.

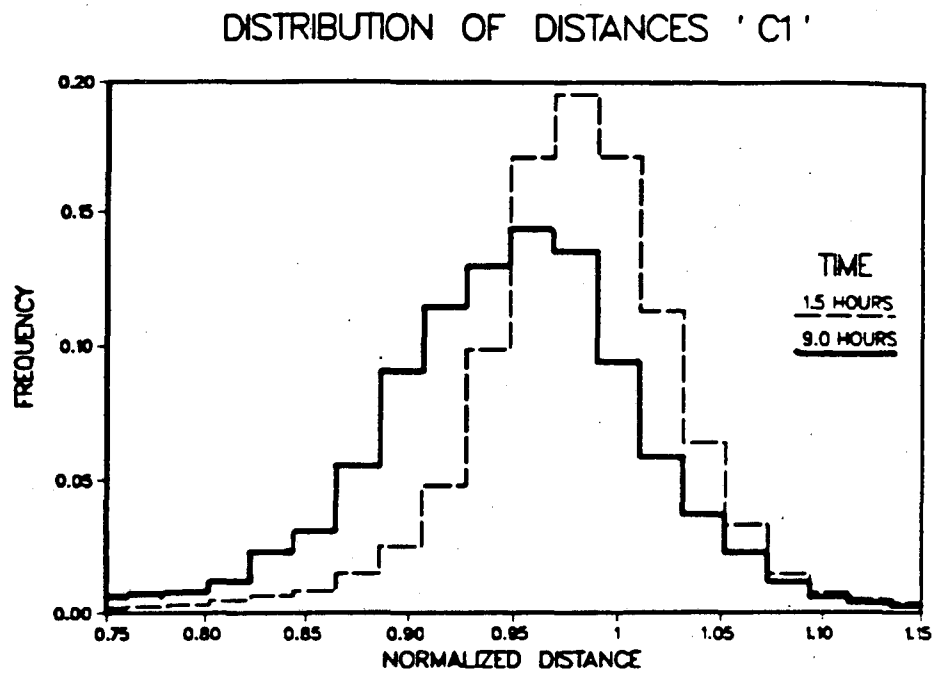

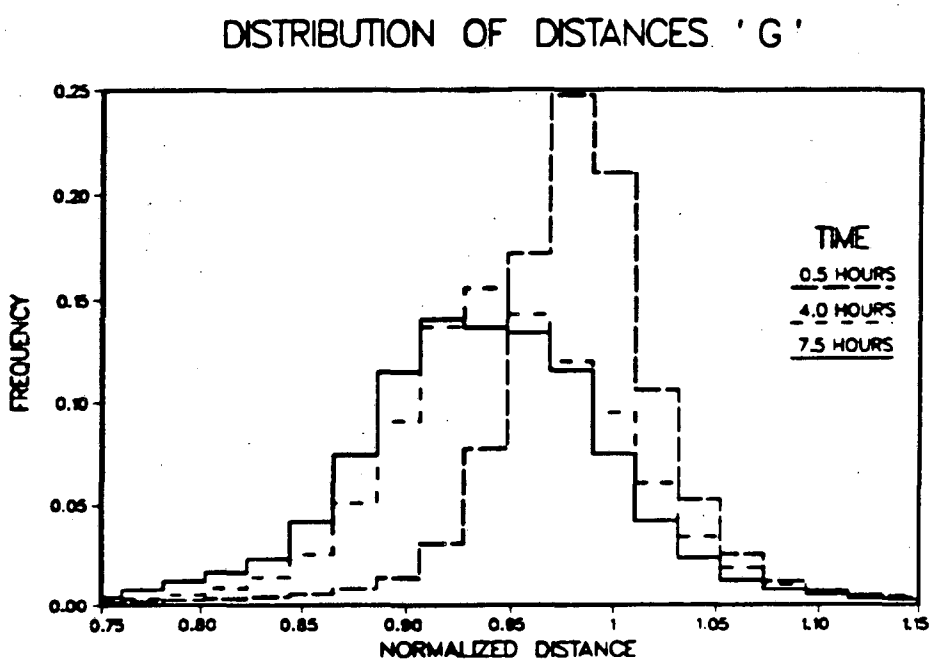

XBL 8412-5355

Figure 4.31 Distributions of the interparticle distances for area C1 and run G showing the rapid spread from the initial delta function and the shift to shorter distances. Run G has a steeper early peak because the first time shown is for a shorter period of sintering in run G than in area C1.

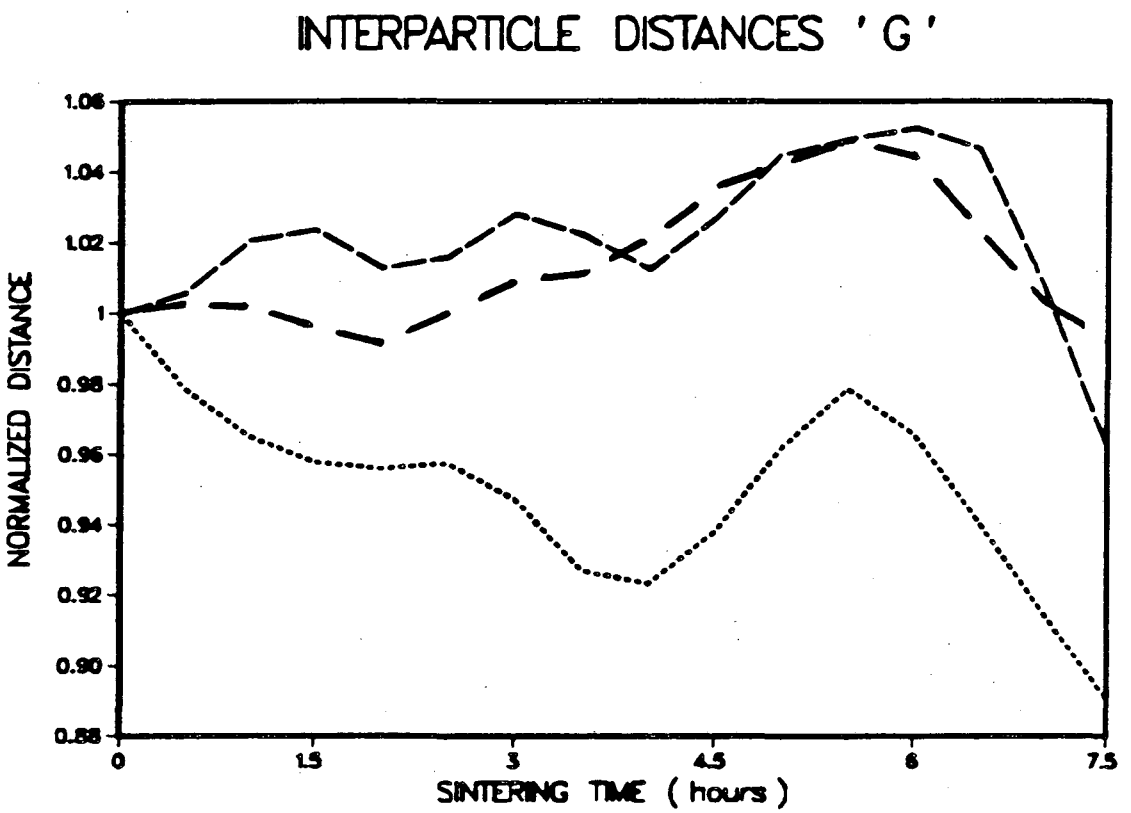

XBL 8412-5356

Figure 4.32 Selected interparticle distances as a function of the sintering time. This shows the great variablity in the interparticle distance as a function of time and the rapid shrinkage of some of the distances in the later portion of the sintering.

shrinkage can be explained by the breakage of a nearby neck in the chain releasing the tension that was stretching the chain. As a result the remaining necks can shrink in an unconstrained manner as shown schematically in figure 4.33.

The nearest neighbor distance is a measure of the linear shrinkage that occurs between individual particles in the array. The overall linear shrinkage of the array can be found either from the distance between spheres on opposite sides of the array or from the square root of the average Voronoi cell area. In order to compare these various measures of the shrinkage it is necessary to normalize the initial average value of all three parameters to 1.0. The square root of the Voronoi area must be used so that all three parameters are in units of normalized length.

When these average normalized values are plotted versus the sintering time in figure 4.34 all three parameters show an initial rapid shrinkage followed by a period of slower shrinkage. The average Voronoi area and average linear distance shrink at nearly the same rate which is much less than the average nearest neighbor distance. This is a result a of a portion of the interparticle shrinkage being accommodated by rearrangement and the opening of pores between clumps of particles. Initially the average linear shrinkage follows the nearest neighbor shrinkage because a strong enough network has not yet been formed to cause much rearrangement. After a network has formed the shrinkage rate is the same for both the Voronoi area and the average linear.

4.4 Interparticle Angles

The interparticle angle as used in this work is the angle formed by two

Breakage of Stretched Necks

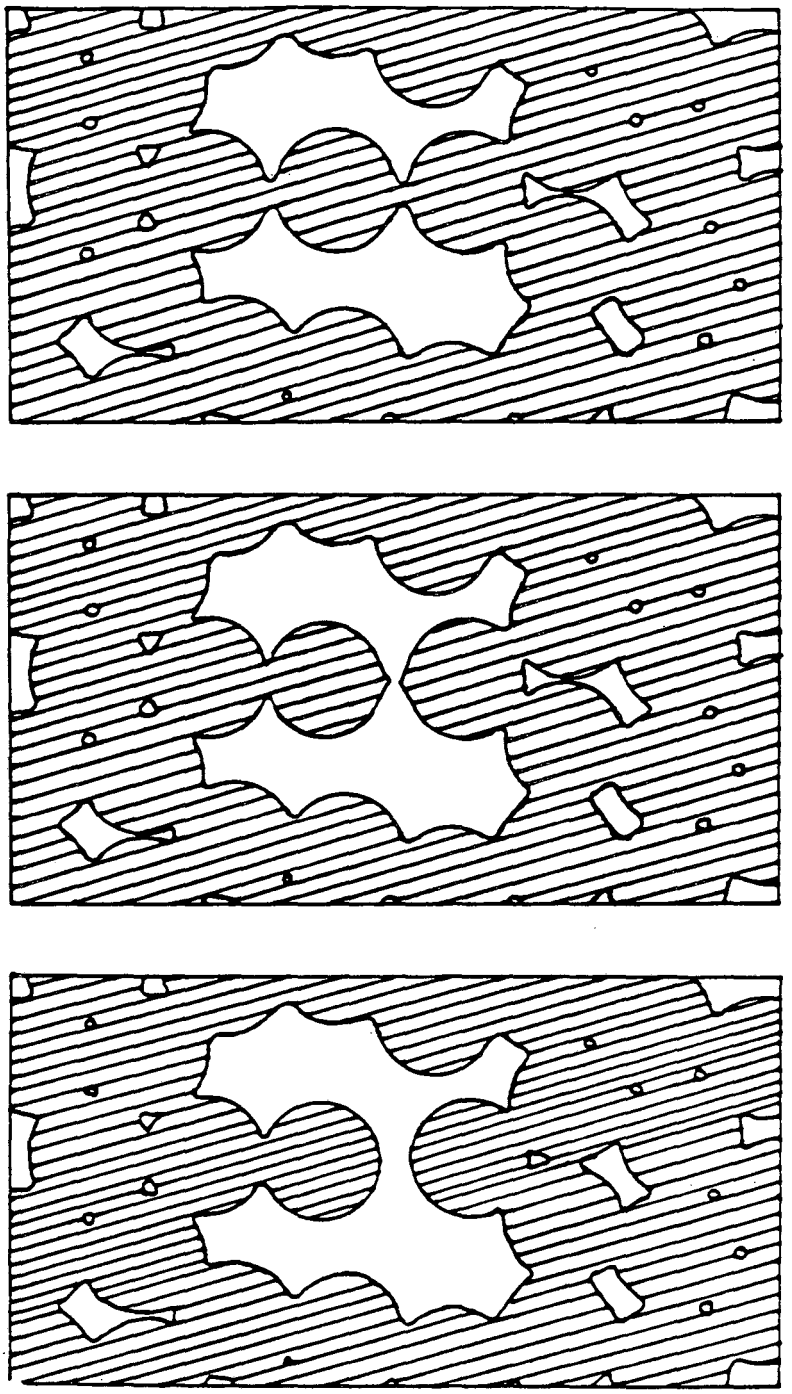

XBL 852-1176

Figure 4.33 Schematic drawing of the breakage of a stretched neck for three different times. Note that the broken ends are absorbed back into the matrix.

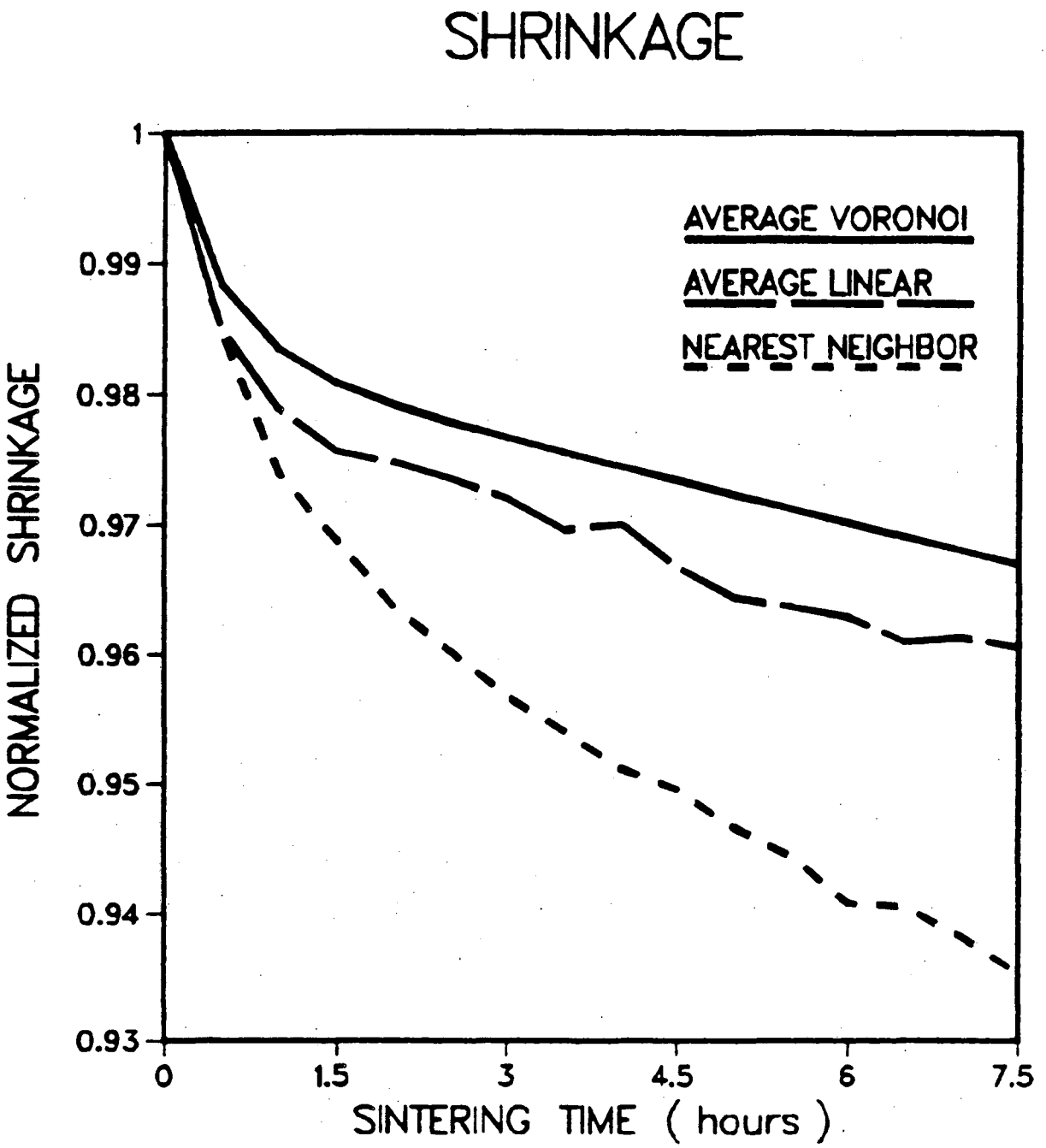

XBL 852-1174

Figure 4.34 Comparison of the shrinkage as measured by the average Voronoi area, the average linear distance across the array, and the nearest neighbor distance.

spheres making contact with a third central sphere. Since a single central sphere may have up to six neighbors only the angles formed by consecutive pairs of contacting spheres are used as illustrated in figure 3.5. This results in the total of all of the interparticle angles about a central sphere being 360 degrees. The average interparticle angle is then only 360 degrees divided by the average coordination number. In this study the average coordination number ranged from 3.6 to 4.1 so the average interparticle angle ranges from approximately 88 to 100 degrees with the most common average between 90 and 95 degrees. Because the average interparticle angle as defined here is inversely proportional to the coordination number it has no direct significance that has not been explained earlier. However, the average interparticle angle is useful in explaining the trends in the change in the angles so it is used later for that purpose.

The interparticle angles range from a low of approximately 45 degrees up to the maximum possible of 360 degrees. The low value of 45 degrees occurs when two small particles form a triangle with a larger particle and particle interpenetration has occurred. The 360 degree angle is a result of the sphere having only one sintering neck. This later case could also be defined as zero but the value of 360 is more easily worked with in creating the statistics.

4.4.1 Distribution of Interparticle Angles

There are very few large interparticle angles so the distributions of the interparticle angles are cut off at 200 degrees. At this point the frequency has dropped to less than 0.2 %. The total number of angles in the various areas ranges from 260 to 476. Therefore, these very low frequencies represent an occasional angle every 4 to 8 degrees. The distributions of the interparticle angles

for all five of the areas studied here were essentially the same so only the data for run G are presented. There were slight differences between the different areas due to the different average angle and number of angles; however, the overall shapes and trends of the curves were the same.

The distribution of the interparticle angles is highly skewed with the major peak located at approximately 60 degrees as shown in figure 4.35. Slightly more than 36 % of the angles lie between 50 and 70 degrees. If the angles were evenly distributed between 50 and 200 degrees only 13.3 % of the total would lie between 50 and 70 degrees. A simple minded analysis of this high frequency at 60 degrees would lead to the misleading conclusion that most of the particles had a coordination number of six since a regular hexagonal packing has interparticle angles of 60 degrees. Examination of the distribution of coordination numbers in figure 4.9 shows that six occurs rather infrequently and that four is actually the most common coordination number. This large frequency of 60 degree angles is explained by many of the spheres being tightly packed on one side with approximately 60 degrees angles and loosely packed on the other. This is shown schematically in figure 4.11 at the border of a high density area.

There is also a secondary peak in the distribution at approximately 105 degrees. Since the average angle is approximately 90 degrees the large number of 60 degree angles must be balanced either the by having some very large angles or a large number of angles just a bit bigger than the average. These angles around 105 degrees are a result of the opening of the 90 degree angle of four fold coordination on the low density side on the sphere by the closure towards 60 degrees on the higher density side. As the interparticle angle increases the frequency decreases with a very slight peak in the area of 180

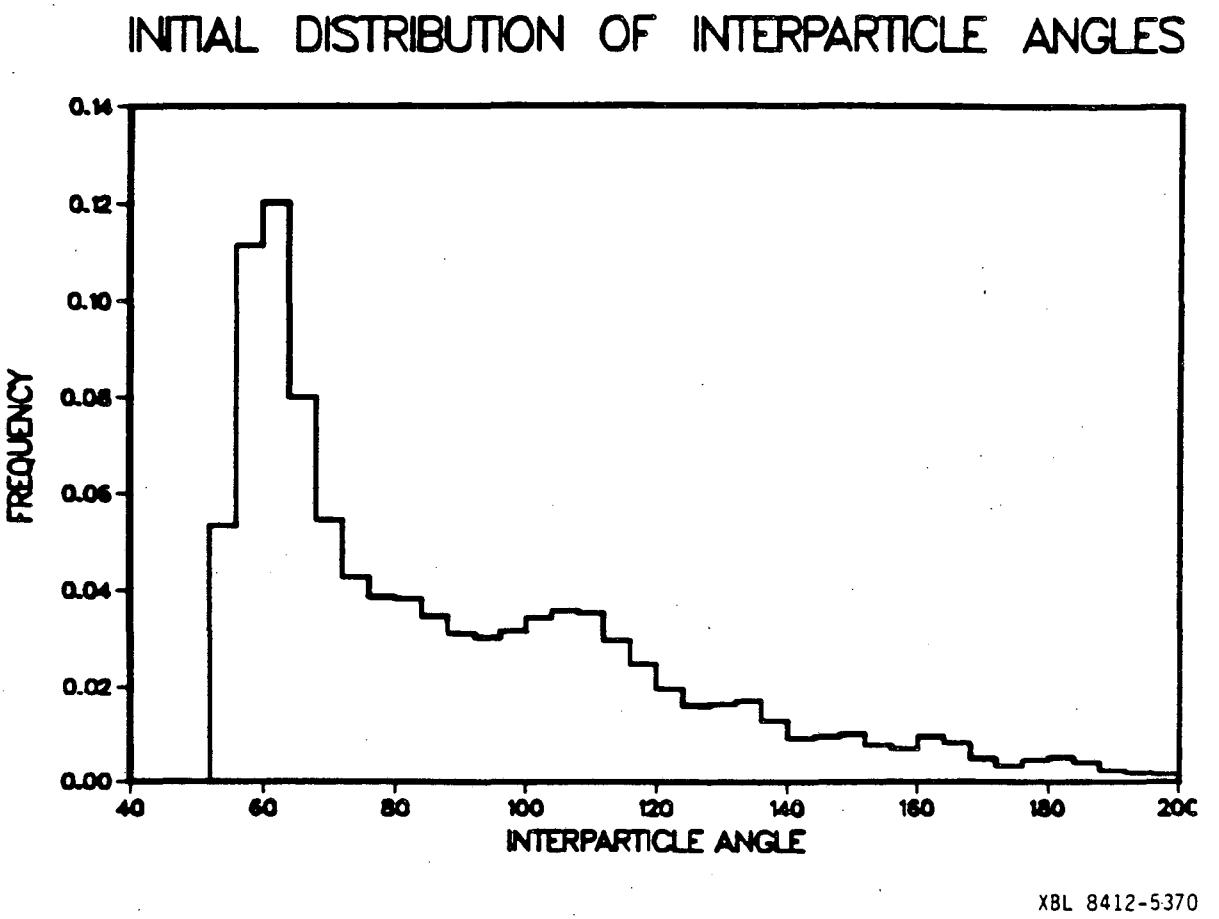

Figure 4.35 The initial distribution of the interparticle angles for run G showing the major peak at 60 degrees and minor peaks at 105 and 180 degrees.

degrees corresponding to two fold coordination and chains of particles between high density areas.

Initially the smallest interparticle angles found are all greater than 52 degrees, but as the sintering proceeds this minimum angle is decreased to 44 degrees after 7.5 hours as shown in figure 4.36. The height of the peak in the distribution at 60 degrees drops as function of the sintering time. This, combined with the appearance of the smaller angles leads to the conclusion that many of the angles initially near 60 degrees exhibit slight shrinkage during sintering. The only other noticeable trend in the angles is for the peak in the distribution between 100 and 120 degrees to be shifted towards lower values by about eight degrees. This shift corresponds to a shift towards the average value of the interparticle angle which lies in the range of 90 to 95 degrees.

4.4.2 Trends of Individual Angles

The changes in the individual interparticle angles in these random two-dimensional arrays vary greatly from angle to angle and can only be classified by general trends. The angles exhibited three general types of behavior, little or no change, positive change, and negative change from the initial angle. The rate of change of the angle was not at all constant and fluctuated greatly with time, selected examples of these different types of behavior are shown in figure 4.37. The changes in the interparticle angles are felt to arise from three sources; asymmetric necks, non-axial applied forces, and noise due to slight errors in the measurement of the particle location. The noise was suppressed by using a nearest neighbor smoothing. The remaining fluctuations in the rate of change of the angle did not exhibit consistent trends as would be expected from an asym-

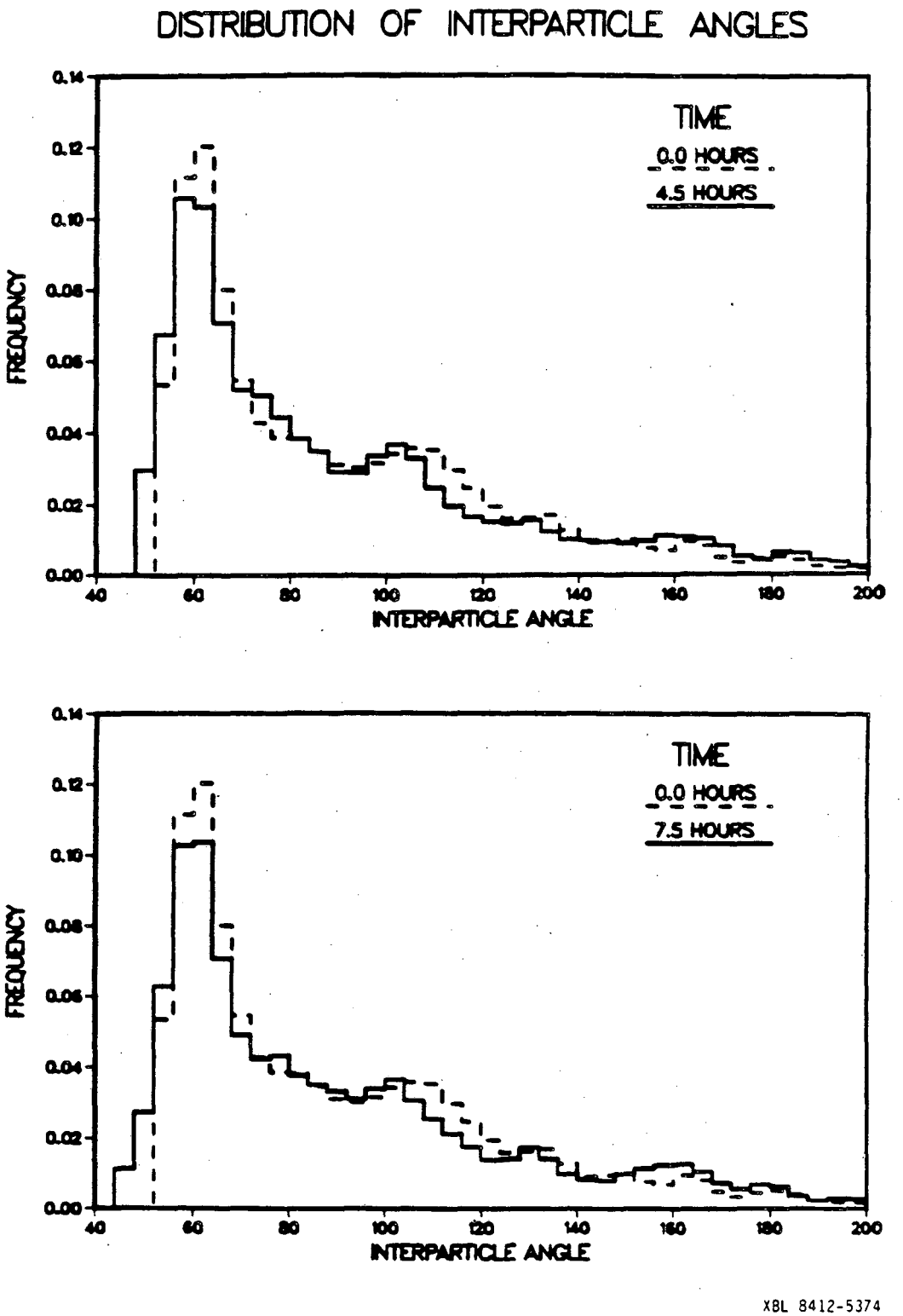

Figure 4.36 Distributions of the interparticle angle for run G comparing the initial distribution with the distributions at 4.5 and 7.5 hours of sintering.

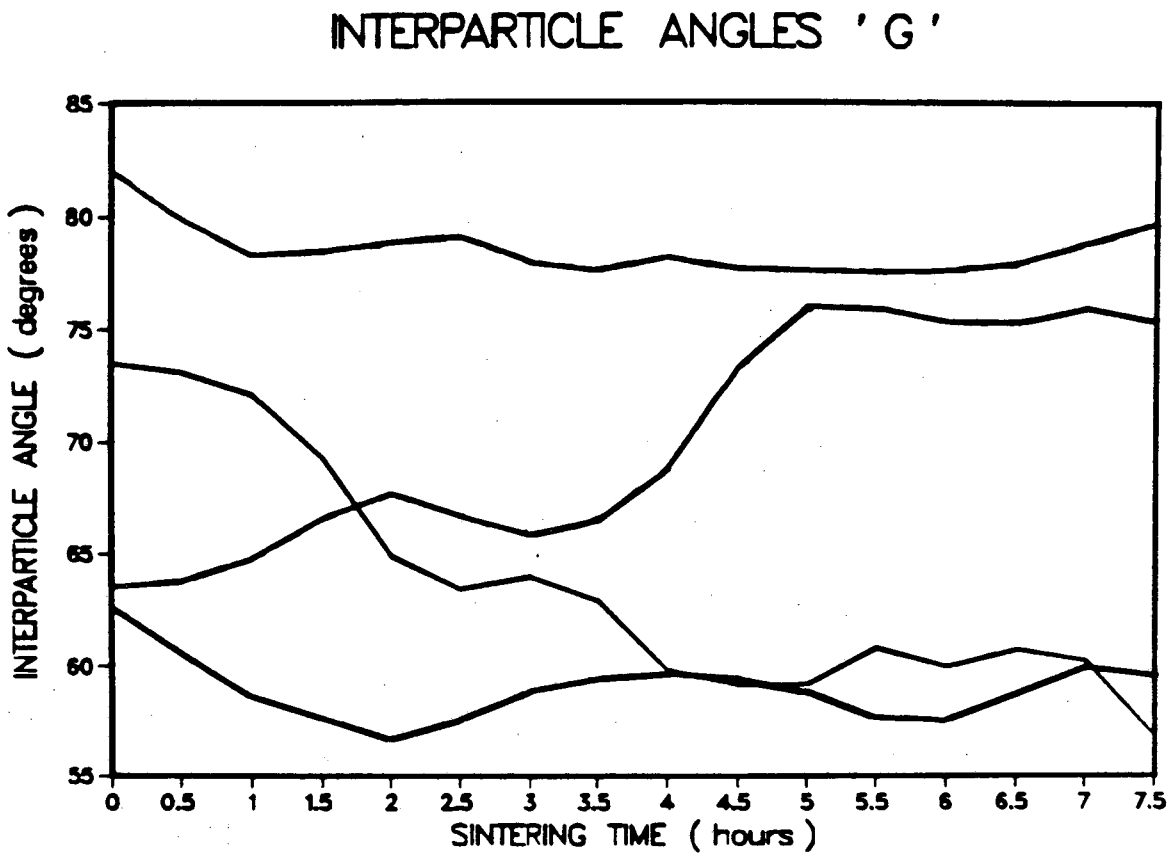

XBL 8412-5365

Figure 4.37 Selected individual interparticle angles as a function of time. Note that the angles fluctuate with time and that the angle can change greatly with time.

metric neck mechanism so it is concluded that the changes are primarily a result of the changes in the interparticle forces.

The maximum changes in each angle were calculated as a measure of the amount of rearrangement that occurred. Nearly all all of the angles were observed to have both positive and negative changes at some point during the sintering, therefore both the positive and negative maxima were calculated. During the sintering process interparticle angles can be both created and destroyed by the change in the number of particle contacts, therefore the initial angle is defined as the first appearance of the particular three particle angle. Since a given interparticle angle can exist at only one of the times studied, the zero change in the angle was ignored as it does not contribute any useful information. The absolute maximum change in the angle was found by using only the larger of either the positive or negative maxima for each initial angle.

The frequency distribution of the maximum change in the angle is roughly approximated by a narrow normal distribution with an average of nearly zero degrees shown in figure 4.38. In all five areas over 50 % of the maximum angular changes are between 1.5 and -1.5 degrees. The large number of values near zero is primarily a result of an angle having a small positive change and then going negative or vice versa; however, some of the angles exhibit only very small angular changes.

The distribution of the absolute maximum angular change is much more evenly spread than the distribution when both the positive and negative maxima are used. This result is plotted in figure 4.39. This is the expected result when the small changes in the opposite direction from the major change are eliminated. For the absolute maximum angular change only 15 to 25 % of the

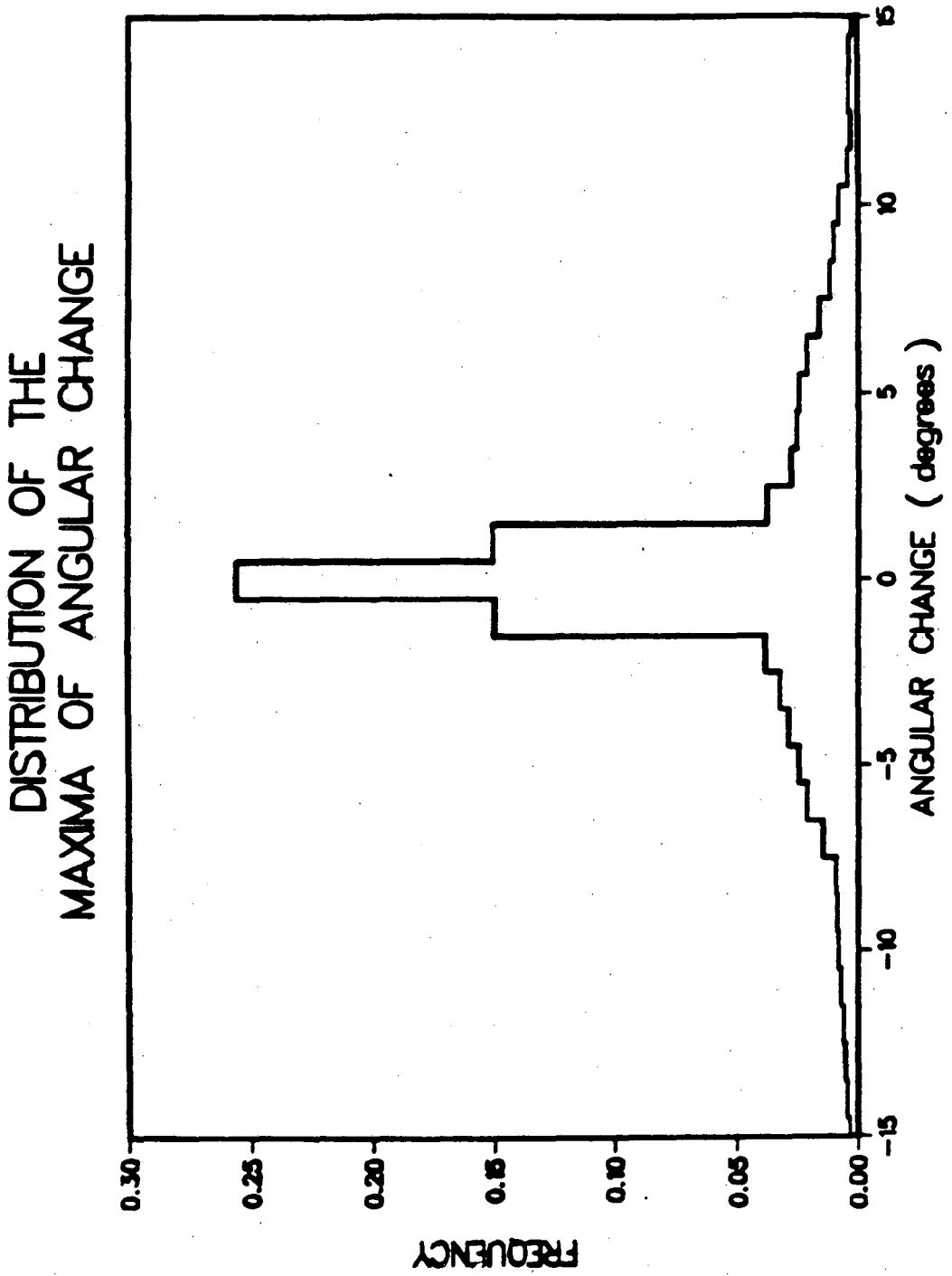

XBL 851-1048

Figure 4.38 The distribution of the maximum angular change showing the large concentration of changes near zero degrees.

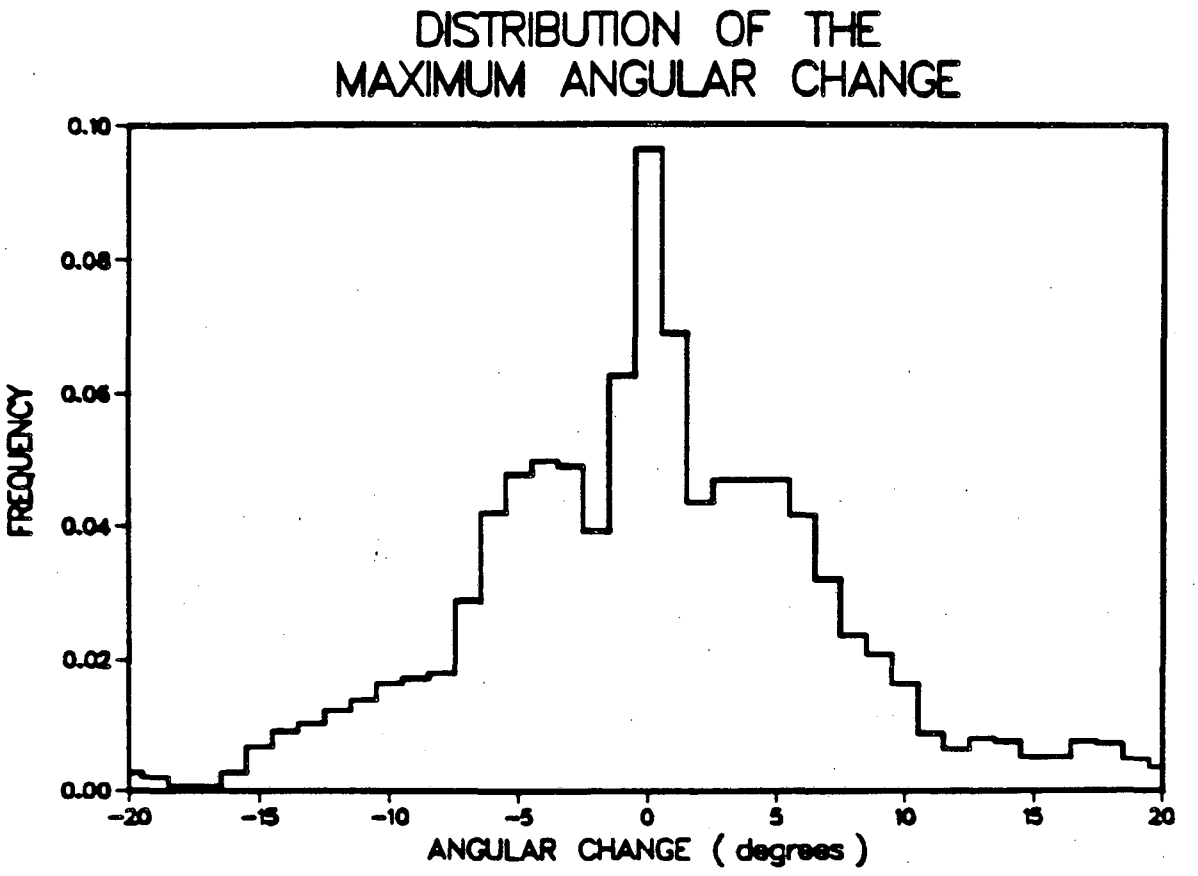

XBL 8412-5366

Figure 4.39 The distribution of the maximum angular change when small changes in the direction away from the larger change are removed. Note that the number of very small changes is much less than in the previous figure.

changes are between 1.5 and -1.5 degrees as opposed to the 50+ % for both maxima. The highest peak in this distribution is at zero degrees but there are also substantial peaks near both plus and minus five degrees. Angular changes of as great as plus and minus 20 degrees were observed. This large change in the angle is three times that observed in three particle models and as much as ten times that predicted from computer simulation of the neck asymmetry. It is therefore concluded that the major cause of rearrangement as measured by changes in the interparticle angle are due to non-axial forces exerted by the rest of the sintering necks in the array.

It is observed that the maximum change in the angle occurs at the later sintering times, although a few of the maxima occur early as shown in figure 4.40. The occurrence of most of the maxima towards the end of the sintering time studied here is expected since it takes time for a network to form which can give rise to bending moments in the necks. Most of the maxima at early times occur in high density, highly coordinated areas where isolated necks that can easily be bent are absent.

When the absolute maximum angular change is plotted versus the initial angle it is seen that there is a extremely large scatter in data as shown in figure 4.41. A very rough trend is observed for smaller angles to increase and larger ones to decrease as seen by the solid line indicating the average angular change versus the initial angle. This is not simply the trend in run G as seen when the average angular change is plotted versus the initial angle for all five areas in figure 4.42. This trend is felt to be the effect of asymmetric necks in rough agreement with the work of Exner [13] for three particle models. The large variation in both the magnitude and direction of angular change lead to the

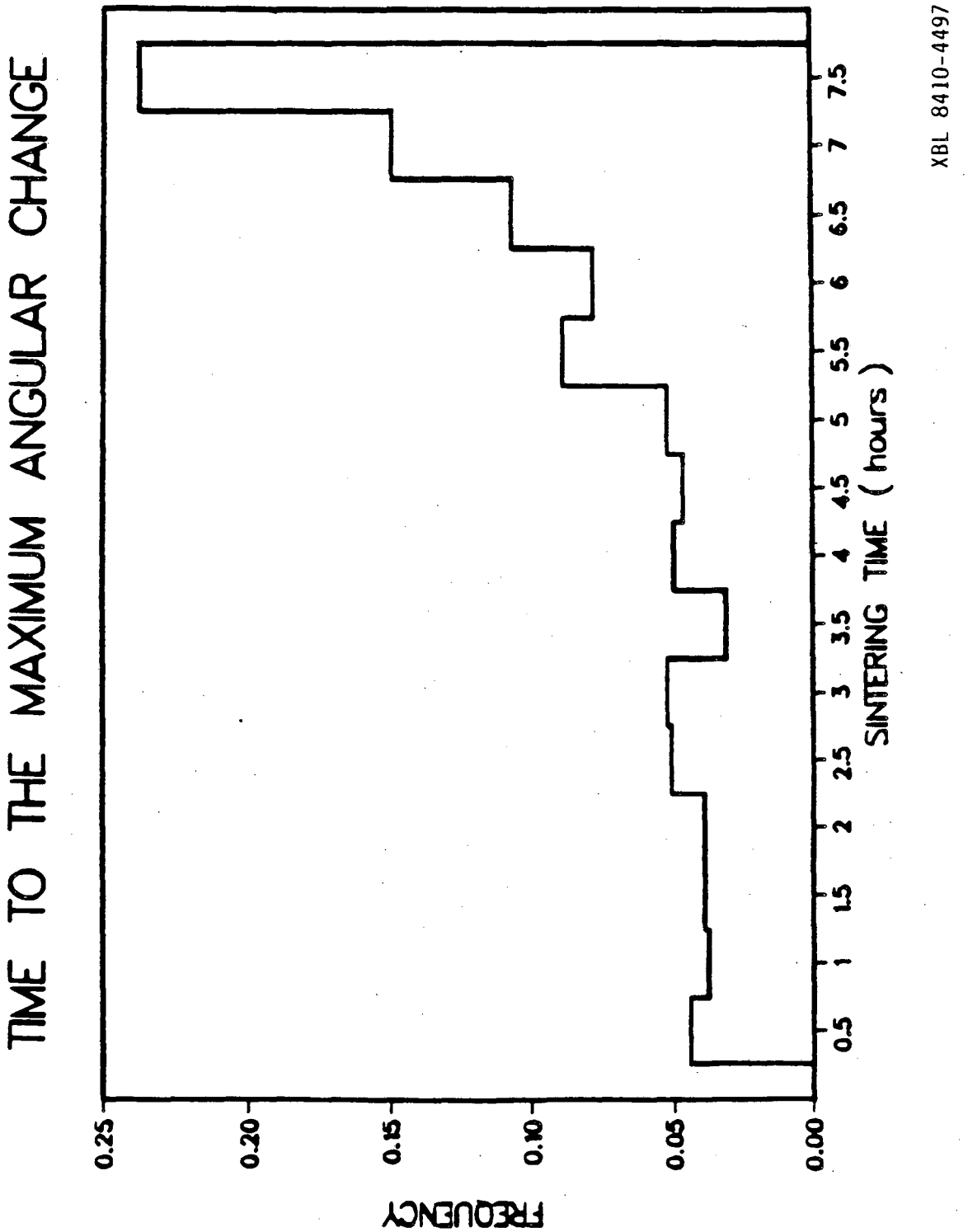

Figure 4.40 The time to the maximum angular change showing that most of the angles reach their maximum in the later stages of sintering.

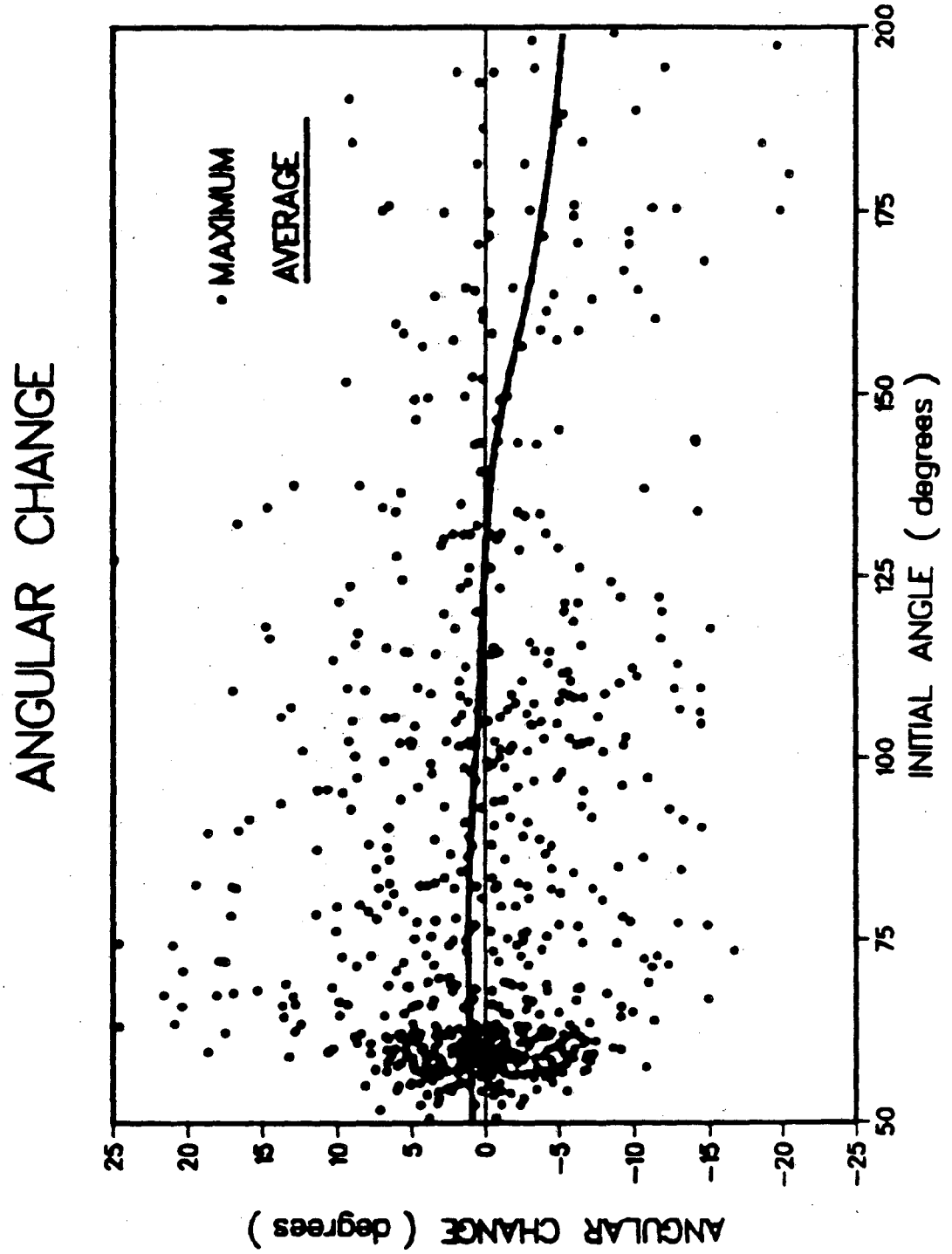

XBL 851-1047

Figure 4.41 The maximum angular change for each angle as a function of the initial angle showing the tremendous scatter in the data.

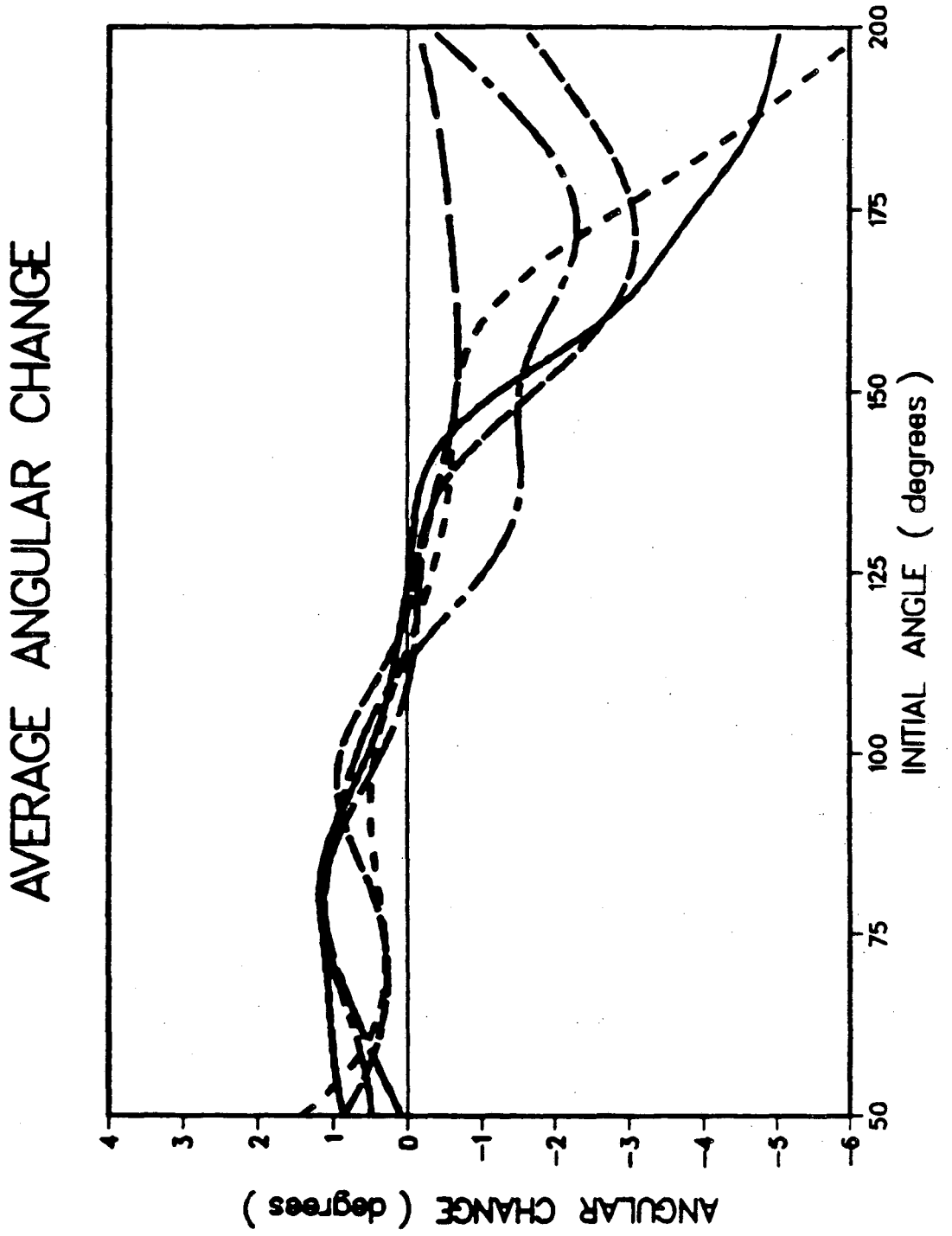

XBL 851-1046

Figure 4.42 The average of the maximum angular change as a function of the initial angle for all five areas studied. There is a slight trend for small angles to enlarge and large angles to contract on the average but this only a very rough trend.

conclusion that the major contribution to these changes is the stress induced in the necks by the formation of a network during sintering. The result of this is that rearrangement during sintering is a combination of both long range network processes and to a small extent, short range asymmetric necks with the dominant contribution being the long range one.

5 Color Mappings

The statistical results presented in the previous section give many indications as to how the spheres interact during sintering, but they fail to convey the exact nature of the interactions. For this reason we have developed the technique of mapping the data value for a particular sphere on to its location in the array. This is accomplished by having the computer draw the Voronoi cell for each of the spheres in the array and then filling the cell with a color corresponding to the appropriate data value. These color mappings graphically depict how the change of a quantity for one cell is influenced by and influences its neighbors. Only the mappings for the largest run, run G, are presented here due to the expense of creating the color hardcopies; however, all of the different areas gave similar results.

In mapping all of the different types of data the same color scheme is employed to make the interpretation of the different maps easier. The lowest data values are plotted in dark blue, as the data values increase the color progresses through lighter blues until green is reached at just under the middle value. Values just above the middle are plotted in yellow, as the data value increases further so does the red content of the color until a deep red is reached at the maximum data value.

5.1 Local Density

The minimum data value used in mapping the local density is 0.5 and the maximum is 1.0. Initially, nearly all of the cells have densities of approximately 0.75 with a scattered few either higher or lower as mapped in figure 5.1. The initial map can be described as areas of slightly higher density in a lower den-

sity matrix. As the array is sintered it is observed that the areas of high density increase in size at the expense of the low density matrix. It is also seen that the cells of highest density normally arise in the middle of a high density region.

A couple of persistent low density regions are observed to remain even at the longest sintering times. These low density regions are predominantly found as a line of cells between areas of higher density. The most notable of these lines is located just to the right of the center and runs vertically. It is only of moderately low density but it is clearly a dividing line between two areas of high density. It is felt that this type of persistent low density dividing line arises from the higher density, highly coordinated areas shrinking and thus preventing the lower density, low coordination areas from shrinking. Two regions of very low density are observed on the left side of the array. Both of these are the edges of pores where there are no spheres connected to them on the side away from the main body of the array.

5.2 Local Shrinkage Rates

The local shrinkage rates are mapped in figure 5.2 with the minimum data value being rapid shrinkage and the maximum data value being rapid expansion. To best understand the shrinkage behavior of the cells it is necessary to compare this figure with the local densities in the previous figure. Initially, over half of the cells are shrinking rapidly with a few areas of rapid expansion. After 7.5 hours nearly all of the cells are shrinking slowly with some mild fluctuations in the rates between cells. This rapid initial shrinkage when the sintering necks are small in diameter followed by slower shrinkage rate as the necks grow as is expected from theory. The increasing neck size and strength at later sintering

times are observed to help evenly distribute the sintering stresses throughout the array causing the sintering rates to become more uniform.

Comparison of the initial shrinkage rates and local densities shows that the expanding areas are located in regions of low density. This is particularly noticeable on the edges of the two pores where the cells are expanding very rapidly. The expansion of some of these cells can even be seen when comparing the size of the Voronoi cells in the first two maps. At 7.5 hours a couple of cells are observed to be shrinking faster than the rest of the cells. These rapidly shrinking cells are located either in or at the edges of areas of low density and shrink because of the relaxation of stress due to the breakage of a nearby sintering neck.

5.3 Maximum Angular Change

The maximum angular change is used here as a measure of the extent of rearrangement that occurs. To find the maximum angular change for a particular sphere it is first necessary to find the maximum change in each of the interparticle angles. The maximum used for this is the absolute maximum as defined in section 4.4. The maximum for a sphere is then the average of the individual maxima where the sphere is at the apex of the interparticle angle. The maximum angular changes were mapped in the same way as the local densities with very small changes in dark blue and large changes of 10 degrees or more in deep red as mapped in figure 5.3. In the same figure the mapping of the local density as in figure 5.1 is also shown to make the comparison between the two easier.

The amount of angular change varies greatly from point to point in the array. There is even one instance of the largest and smallest changes being

located next to each other in the left central region of the array. Most of the largest and smallest angular changes are observed to occur at the boundaries between high and low density, particularly those boundaries that remain during the later stages of sintering. A particularly good example of this relationship is found to correspond to the low density dividing line discussed earlier and located just to the right of the center of the array. It is felt that these low density dividing lines are the location of high stresses similar to the stress concentration at the edge of a slit or hole. The higher stresses in these areas result in large amounts of particle motion. If the spheres are already aligned with the stress the necks are stretched with little angular change. If the spheres are not aligned with the stress the spheres are sheared past each other to make the necks align with the stress, resulting in large angular changes.

The wide variation in the extent of angular change over very short distances is proof that asymmetric necks are not the major driving force for rearrangement. If asymmetric necks were responsible for rearrangement then the maximum angular changes should be much more evenly distributed and there should be little or no correspondence between very large and very small angular changes and the boundaries between high and low density. As was stated earlier, it is concluded that the major driving force for rearrangement is the redistribution of the tensile stress generated by the sintering necks in a random network.

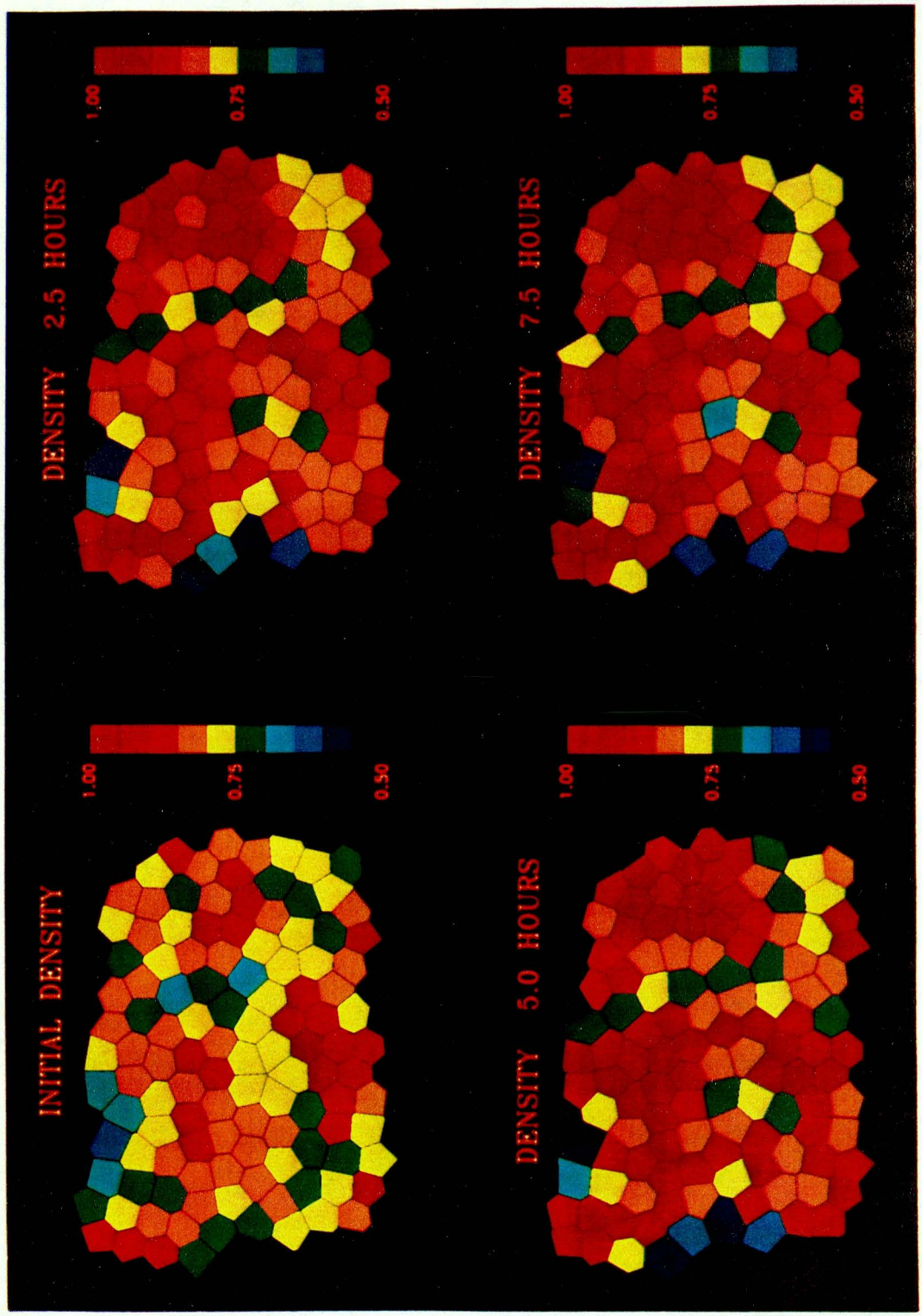

Figure 5.1 Color mapping of the local density at four different times. Note that most of the cells densify but that a few areas of low density cells persist into the later stages of sintering. Most of these low density areas are dividing lines between areas of high density.

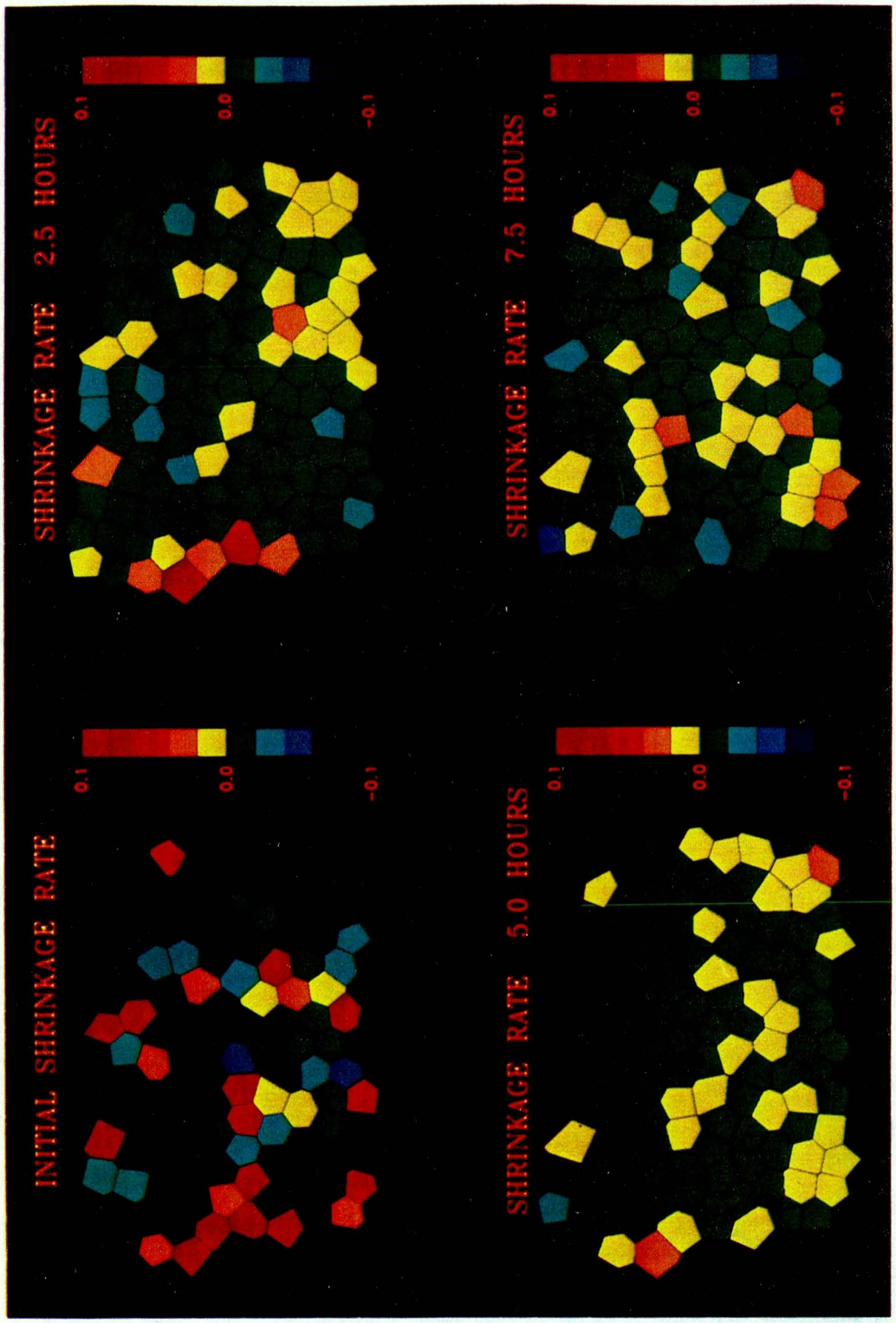

Figure 5.2 Color mapping of the local shrinkage rate at four different times. Upon comparison with the previous figure it is seen that most of the areas of expansion occur between high density areas.

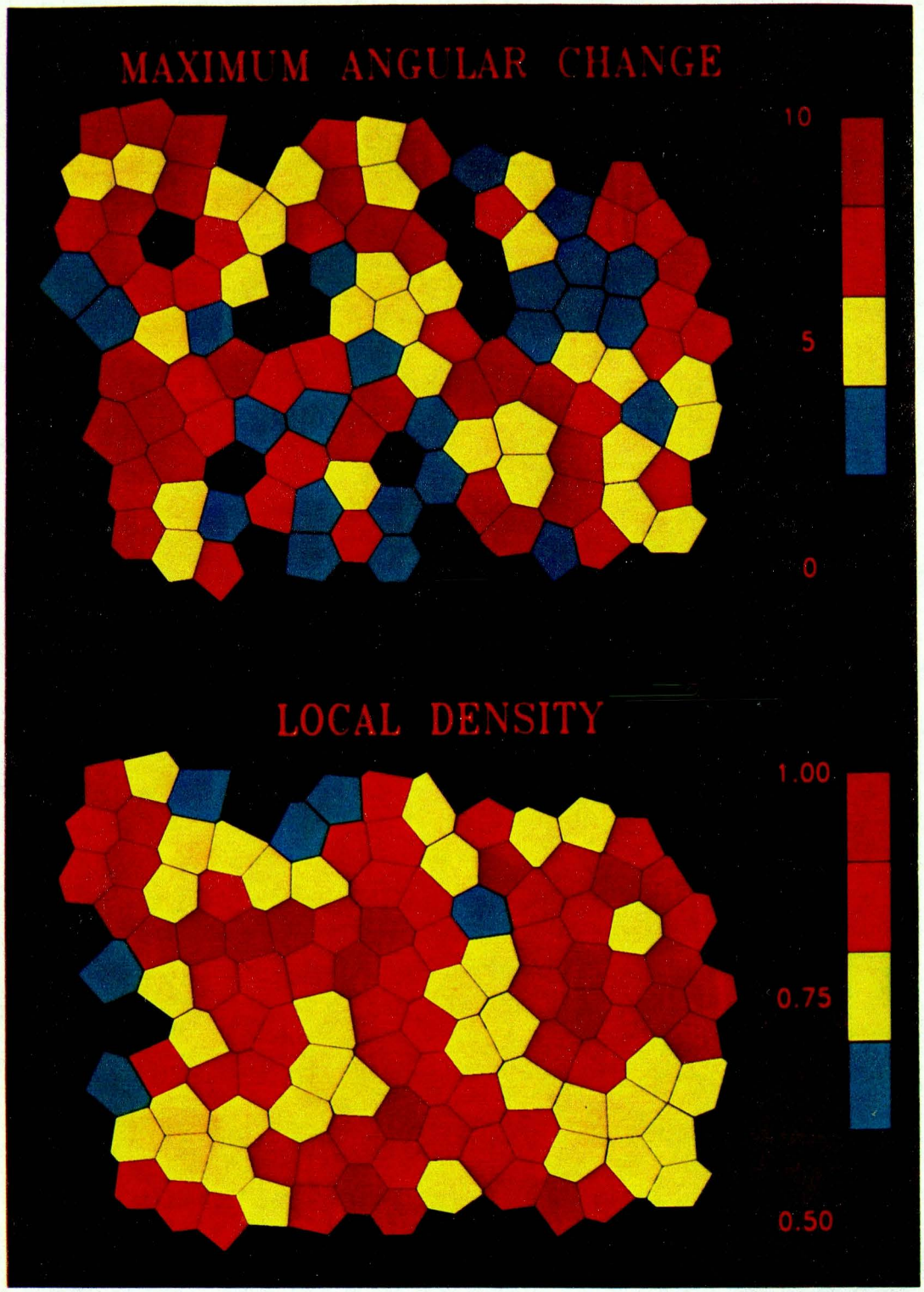

Figure 5.3 Color mapping of both the maximum angular change and the local density. Most of the very large and very small angular changes occur along the low density lines between areas of high density.

6 Conclusions

The results of this study give the most detailed view yet of sintering in two dimensions. This study is also the first to follow a large random array of spheres through the sintering process from the first moment of heat treatment. The most important conclusion is that rearrangement during sintering is a extremely complex process, and that it is futile to attempt to simply extrapolate the two-sphere or three-sphere model to two or three dimensions. This obvious conclusion is most easily seen in both the large magnitude and high degree of scatter in the change of the interparticle angular. During the course of this study a very large body of statistics was generated about sintering in two dimensions. Most of the conclusions were given as these statistics were presented but they will restated in order to clarify the above major point.

The average coordination number of all of the arrays studied here ranged from 3.5 to 4.1. The coordination number was distributed in a fairly predictable manner with a peak in the distribution at 4 nearest neighbors. The width of the distribution varied mildly from array to array with narrower distributions indicating more homogeneous packings. The distribution was observed to become more spread during sintering in all of the areas studied here. This is a result of the formation of new bonds in high density regions and the breakage of some of the bridges that connect them.

The local density was defined as the projected area of an average sphere divided by the Voronoi cell area. This local density is an excellent measure of the densification that an individual sphere has undergone. This is because it incorporates the entire local neighborhood of the sphere and not just those that are connected to it by a sintering neck. It was found that initially the local

density is approximately normally distributed, but after sintering for a period of time a tail is left at the low density end of the distribution. The cells in this tail do not actively expand to any great extent but they are left behind as the majority of the cells shrink. These persistent low density cells are found to have much lower coordination than the rest of the array. These low density cells are often grouped together between areas of higher density or located at the edges of voids. It is found that spheres with a local density greater than 0.650 will densify and those of lower local density are apt to de-densify.

The local densification rate was defined as the rate of change of the local density as a function of time. Initially nearly all of the cells shrink at widely distributed rates. As the sintering progresses the distribution narrows dramatically with slight overall shrinkage. At the end of the period studied here it was found that the distribution becomes skewed towards expansion; however, the larger number of slowly expanding cells are more than offset by faster shrinking cells so the array undergoes overall densification at all times. During the entire sintering time both the most rapidly shrinking and expanding cells are associated with areas of low density.

The nearest neighbor distance was defined as the distance between sphere centers that were connected by a sintering neck. In order to accommodate the variation in the sphere diameter this distance was normalized so that the initial appearance of a particular distance was set equal to 1.0. As the sintering progressed the distribution of the nearest neighbor distances was observed to become more spread. This spreading was accomplished by most of the distances shrinking in various amounts with a few of them elongating. These elongated necks are being stretched by the tensile forces generated in the network. Many

of these stretched necks exhibit a rapid shrinkage towards the end of the sintering time as a nearby neck breaks and relieves the tensile stress. The average nearest neighbor distance is used as a measure of the interparticle shrinkage in the array. After appropriate manipulations it is found that the area shrinkage and the average linear shrinkage across the array are less than the interparticle shrinkage would suggest, this is a result of a portion of the interparticle shrinkage being accomodated by rearrangement.

The interparticle angle was defined as the angle between two spheres making contact with a third sphere located at the apex of the angle. The distribution of the interparticle angles was observed to be strongly peaked at 60 degrees with a long tail extending to at least 200 degrees. The large number of 60 degree angles indicates that many of the spheres are tightly packed on one side with looser packing on the other since six fold coordination is found to be rather rare. The changes in the individual angles vary greatly both from sphere to sphere and as a function of time. Many of the angles exhibit maximum changes larger than 10 degrees with a few greater than 25 degrees. This finding is in direct contridiction with the changes of 1 to 6 degrees found for asymmetric necks. It is therefore concluded that the primary driving force for rearrangement in two-dimensional arrays of spheres is the formation of a network through which sintering stresses can act at longer range.

This study therefore proves that the sintering process is very complex and that the simple extrapolation of the two-sphere model is of little significant use. The measurement of the local density for a particle and its neighbors can be used to describe the expected shrinkage behavior of the particle, however, it is not possible at this time to write an explicit formula describing this behavior.

The complete description of rearrangement requires the analysis of the stress distribution in the random network of the sintering necks connecting the spheres where the stresses themselves are generated in the necks. The process of rearrangement during sintering can not be attributed to asymmetric necks or other very local phenomena. In conclusion it is found that rearrangement during sintering is a long range, multiparticle process that arises mainly out of the local density fluctuations that are found in inhomogeously packed arrays.

REFERENCES

1 E. Arzt, "The Influence of an Increasing Particle Coordination on Densification of Spherical Particles", Acta. Met. 30, 1883-90 (1982)

2 M. F. Ashby, "A First Report on Sintering Diagrams", Acta. Met. 22, 274-89 (1974)

3 L. K. Barret, C. S. Yust, "Progressive Changes in the Void During Sintering", Met. Trans. 239, 1172-80 (1967)

4 J. D. Bernal, "Geometry of The Structure of Monotomic Liquids", Nature 185, 68-70 (1960)

5 P. Bross, H. E. Exner, "Computer Simulation of Sintering Processes", Acta. Met. 27, 1013-20 (1979)

6 R. L. Coble, "Initial Sintering of Alumina and Hematite", J. Am. Ceram. Soc. 41, 55-60 (1958)

7 R. L. Eadie, D. S. Wilkinson, G. C. Weatherly, "The Rate of Shrinkage During the Initial Stage of Sintering", Acta. Met. 22 [10], 1185-95 (1974)

8 R. L. Eadie, W. A. Miller, G. C. Weatherly, "Random Close Packing and Sintering: Some Implications for Initial - Stage Shrinkage", Scripta Met. 8, 755-62 (1974)

9 R. L. Eadie, G. C. Weatherly, "Contributions of Grain Boundary and Volume Diffusion to Shrinkage Rates During Sintering", in "Catalysis and Sintering", ed. G. C. Kuczynski, 239-48, Plenum Press (1975)

10 P. C. Eloff, F. V. Lenel, "The Effects of Mechanical Constraints Upon the Early Stages of Sintering", in "Modern Developements in Powder Metallurgy v. 4", ed. H. H. Hausner, 291-302, Plenum Press (1974)

11 H. E. Exner, G. Petzow, P. Wellner, "Problems in the Extension of Sintering Theories to Real Systems", in "Sintering and Related Phenomena", ed. G. C. Kuczynski, 351-62, Plenum Press (1973)

12 H. E. Exner, G. Petzow, "Shrinkage and Rearrangement During Sintering of Glass Spheres", in "Sintering and Catalysis", ed. G. C. Kuczynski, 279-93, Plenum Press (1976)

13 H. E. Exner, "Reviews on Powder Metallurgy and Physical Ceramics", Freund Publishing House (1979)

14 H. E. Exner, P. Bross, "Material Transport Rate and Stress Distribution During Grain Boundry Diffusion Driven by Surface Tension", Acta. Met. 27, 1007-12 (1979)

15 H. J. Frost, "Cavities in Dense Random Packings", Acta. Met. 30, 889-904 (1982)

16 R. A. Gregg, F. N. Rhines, "Surface Tension and the Sintering Force in Copper", Met. Trans. 4, 1365-74, (1973)

17 T. M. Hare, "Statistics of Early Sintering and Rearrangement by Computer Simulation", in "Sintering Processes", ed. G. C. Kuczynski, 77-93, Plenum Press (1980)

18 G. Hermann, H. Gleiter, G. Baro, "Investigation of Low Energy Grain Boundaries in Metals by a Sintering Technique", Acta. Met. 24, 353-59 (1976)

19 C. Hsueh, L. C. De Jonghe, "Particle Rotation in Early Sintering", J. Am. Ceram. Soc. 67 [10] C215 (1984)

20 W. S. Jodrey, E. M. Tory, "Computer Simulation of Isotropic, Homogeneous, Dense Random Packing of Equal Spheres", Powder Technology 30, 111-18 (1981)

21 D. L. Johnson, "New Method of Obtaining Volume, Grain Boundary, and Surface Diffusion Coefficients From Sintering Data", J. App. Phys. 40 [1], 192-200 (1969)

22 B. Kellet, F. F. Lange, "Stresses Induced by Differential Sintering in Powder Compacts", J. Am. Ceram. Soc. 67, 369-71, (1984)

23 W. D. Kingery, M. Berg, "Study of the Initial Stages of Sintering Solids by Viscous Flow, Evaporation - Condensation, and Self - Diffusion", J. App. Phys. 26 [10], 1205-12 (1955)

24 G. C. Kuczynski, "Self Diffusion in Sintering of Metallic Particles", Met. Trans. 185, 169-78 (1949)

25 A. Mohan, N. C. Soni, V. K. Moorthy, "Review of Earlier Work on Mechanisms With Sintering Diagrams", Science of Sintering 12 [3], 163-70, (1980)

26 F. A. Nichols, "Coalescence of Two Spheres by Surface Diffusion", J. App. Phys. 42 [7], 2805-08 (1966)

27 J. A. Pask, C. E. Hoge, "Thermodynamic Aspects of Solid State Sintering", in "Sintering and Catalysis", ed. G. C. Kuczynski, 229-38, Plenum Press (1975)

28 R. L. Porter, "The Effect of Surface Topography During the Initial Stage of Sintering", in "Sintering Processes", ed. G. C. Kuczynski, 129-34, Plenum Press (1980)

29 J. W. Ross, W. A. Miller, G. C. Weatherly, "Computer Simulation of Sintering in Powder Compacts", Acta. Met. 30, 203-12 (1982)

30 G. D. Scott, "Radial DIstribution of the Random Close Packing of Equal Spheres", Nature 194, 956-57 (1962)

31 F. B. Swinkles, M. F. Ashby, "A Second Report on Sintering Diagrams", Cambridge University (1980)

32 T. L. Wilson, P. G. Shewmon, "The Role Of Interfacial Diffusion in the Sintering of Copper", Met. Trans. 236, 48-58 (1966)

33 O. J. Wittemore, J. A. Varela, "Pore Distributions and Pore Growth During The Initial Stages of Sintering", in "Sintering Processes", ed. G. C. Kuczynski, 51-60, Plenum Press (1980)

34 B. Wong, J. A. Pask, "Models for Kinetics of Solid State Sintering", Lawrence Berkeley Laboratory preprint LBL-6293 (1977)

This report was done with support from the Department of Energy. Any conclusions or opinions expressed in this report represent solely those of the author(s) and not necessarily those of The Regents of the University of California, the Lawrence Berkeley Laboratory or the Department of Energy.

Reference to a company or product name does not imply approval or recommendation of the product by the University of California or the U.S. Department of Energy to the exclusion of others that may be suitable.

TECHNICAL INFORMATION DEPARTMENT
LAWRENCE BERKELEY LABORATORY
UNIVERSITY OF CALIFORNIA
BERKELEY, CALIFORNIA 94720